Biophysical Impacts of Mixed Chain Phospholipids on Membrane Structure and Phase Behavior: Insights from Molecular Dynamics and Experimental Approaches

‘

A Dissertation Presented for the

Doctor of Philosophy

Degree

The University of Tennessee, Knoxville

Emily H. Chaisson

August 2025

Copyright © 2025 by Emily H. Chaisson
All rights reserved.

To my sister: Since Mom always makes sure everything is equal, it's only fair that half of this is yours, too.

ACKNOWLEDGMENTS

So many people have shaped and supported me along the way - but some have truly stood out in ways I'll never forget.

Dr. Fred Heberle, thank you for sharing in my excitement for science and for being a steady, supportive presence throughout my Ph.D. You've played a crucial role in my development as a scientist, and I cannot imagine navigating grad school without a PI like you. You're an amazing scientist and even better person.

Dr. Milka Doktorova, your mentorship has meant more to me than I can express. You've been a steady source of encouragement and have always known what to say when I need it most. Even when you didn't have to be, you were there with your time, wisdom, and kindness. Your belief in me has left a lasting mark on both my work and me, and I'll always be grateful for it.

To my committee members: Dr. Tessa Calhoun, thank you for being a voice of reason, for believing in me when I didn't, and for always being up for eating a chocolate cupcake (or three) - even when my confidence waivered your support never did. Dr. Sharani Roy, you were the first to truly challenge me in grad school, and I'm better for it. Thank you for pushing me in ways I didn't know I needed. Dr. Steve Abel, thank you for your kindness, for generously sharing both your students and your wisdom, and for always being a kind face in a crowd.

To my lab mates - past and present - Dr. Kristen, Dr. Karan, Elizabeth, Deeksha, Loretta, Jimmie, and Anupam: You all made hard days bearable and good days feel like an R^2 of 1 on a phosphate assay. I'm forever grateful for our shared ideas, snacks, trips, and giggles. Thank you all for sharing not only your ideas with me but also your lives.

To my best friend Ashley, and undergraduate adviser Dr. Jason Pajski : you both are a big reason I started this journey and an even bigger reason I finished.

To my beautiful big sister Jess: you've been one of my biggest sources of strength, comfort and laughter. You are my hero, and being your little sister is still way cooler than having a Ph.D. I love you.

To the rats: watching you grow reminded me to keep growing too. Lily, thank you for always pulling me back into the joy of middle school drama and keeping me hip.

Charlie, thank you for reminding me I am cool when Lily tells me I am not. I am so lucky to be your aunt.

To Coleman: Thank you for always making me feel like your home is mine too and for letting me unofficially sub in when I needed a fun trip with the kids.

And finally, to my parents. There aren't enough words or pages to fully express my gratitude. My success is a reflection of both of you. Thank you not only for being my support system, but also for giving me the best one. Our family kinda rocks.

Mom - I'm finally done! Thank you for your unconditional support, for listening to every complaint, for giving advice when I needed it (and sometimes when I didn't want it), and for always reminding me that my worth isn't tied to school. You are someone I'm incredibly proud of, and you've helped me become someone I'm incredibly proud to be.

Dad - we're tied at three now. Thank you for your endless encouragement, for being my coach in life, and for always showing up. You have always known I could do it, and you're right once again. Here's hoping the next chapter goes as smoothly as my change-up.

ABSTRACT

Lipid bilayers are essential for all forms of life and are comprised of hundreds of structurally distinct lipids. One of the most important lipid bilayers in nature is the plasma membrane (PM) that forms the external barrier of all living cells. Given the vast diversity of lipid types and structures, a major challenge in membrane biophysics is determining how specific lipid classes contribute to physical properties of the PM. One understudied class of phospholipids consists of lipids where both chains are saturated but differ in the number of carbons. These mixed chain lipids are thought to alter midplane interactions as compared to their symmetric counterparts. Here, we developed novel methodologies to investigate the fundamental biophysical properties of mixed chain lipids both *in vitro* and *in silico*. All-atom molecular dynamics simulations were used to explore the effect of acyl chain mismatch on bilayer properties at an atomic scale. Complementary experimental techniques including FRET, confocal fluorescence microscopy, and cryogenic electron microscopy were used to examine model membrane systems exhibiting phase separation. Simulations reveal that chain mismatch and glycerol backbone positioning significantly influence bilayer properties such as bending modulus, interdigitation, and acyl chain backbending. The application of a phenomenological model for FRET data enabled precise determination of the miscibility transition temperature and phase behavior of mixed chain lipid systems composed of a high-melting lipid, low melting lipid and cholesterol. Complementary experimental findings further demonstrated that the positional transposition of acyl chains on the glycerol backbone significantly impacts lateral lipid organization in the membrane and other bilayer properties. These findings and methods enhanced our understanding of membrane biophysics, establishing a strong foundation for future studies on the structure, dynamics, and function of complex biomembranes.

TABLE OF CONTENTS

Chapter One Background and Introduction 1

1.1 Motivation 3

1.2 Structural Basis of Membrane Heterogeneity 4

1.2.1 Lipid and Membrane Structure 4

1.2.2 Lateral Lipid Heterogeneity and the Lipid Raft Hypothesis 6

1.3 The PM Is Asymmetric 8

1.3.1 The PM Has Lateral Heterogeneity 8

1.3.2 The PM Leaflets Differ in Composition 10

1.3.3The PM Has Lipid Number Asymmetry 12

1.3 Molecular Dynamics (MD) Simulations to Study Model Membranes 12

1.4.1 MD Simulations Are Advantageous in Membrane Studies 12

1.4.2 Building Bilayers and Modifying Lipid Structures from CHARMM-GUI 16

1.4.3 Calculating the Lateral Pressure Profile for Lipid Bilayers 18

1.4.4 Leaflet Asymmetry Can Drive Differential Stress 19

1.4.5 Ways to Build Compositionally Asymmetric Bilayers, and How to Choose One 20

1.4.5 Simulated Lipid Bilayers with Leaflet Lipid Imbalance 22

1.4.6 Calculating the Bending Moduli from MD Simulations 23

1.4.6.1 Real Space Fluctuation (RSF) Method for Determining Bending Rigidity 23

1.4.6.2 Transverse Curvature Bias (TCB) Method 24

1.5 Model Membranes for Studying Phase Separation in the PM 24

1.5.1 Simplified Models of the PM 24

1.5.2 Types of Model Membranes 25

1.5.3 Domain Structure and Formation in Model Membranes 26

1.6 Techniques for Examining Phase Behavior in Model Membranes 27

1.6.1 Confocal Fluorescence Microscopy (CFM) 27

1.6.2 FRET 28

31.6.3 Cryo-EM 29

Chapter 2 Quantifying Acyl Chain Interdigitation in Simulated Bilayers Via Direct Transbilayer Interactions 31

2.1 Abstract 33
2.2 Introduction 33
2.3 Methods 35
2.3.1 Simulation details 35
2.3.2 3D Voronoi tessellation 36
2.3.3 Normalized Interfacial Surface Area (nISA) 37
2.3.4 Carbon Contact Matrix (ccMat). 37
2.3.5 Density Overlap Matrix (doMat) 40
2.4 Results and Discussion 40
2.5 Conclusion 45
Chapter Three Structural Consequences of Chain-Length Mismatch in Simulated PC Lipid Bilayers 47
3.1 Abstract 49
3.2 Introduction 49
3.3 Methods 51
3.3.1 Simulation Protocol 51
3.3.2 Analysis Methods 52
3.3.2.1 Area per lipid, bilayer thickness, and chain order parameters. 53
.3.2.2 Bending rigidity and area compressibility 54
3.3.2.3 The polymer brush model 54
3.3.2.4 Interdigitation 55
3.3.2.5 Acyl chain backbending 56
3.4 Results and Discussion 57
3.3.4 Chain Length Mismatch Drives Changes in Bilayer Structure 57
3.4.2 Chain Mismatch Drives Changes in Mechanical Properties. 60
3.4.4 Chain asymmetric lipids have a higher propensity to interdigitate and backbend. 63
3.5 Summary and Conclusions 67
Chapter Four 69
Phenomenological models for determining phase behavior of liposomes from SP-FRET 69
4.1 Abstract 71

4.2 Significance 71
4.2 Introduction 72
4.4 Materials and Methods 74
4.4.1 Chemicals 74
4.4.2 Sample preparation 75
4.4.4 FRET measurements 75
4.3.3 FRET fitting with 3-,4- and 5-parameter models 76
4.5 Results and Discussion 78
4.5.1 Determining the best model in sample replicates 79
4.5.2 Determining phase behavior with different cholesterol concentrations 79
4.5.3 Determining the $Tmisc$ using a single probe pair 82
4.6 Conclusion 82
Chapter Five The Influence of Mixed Chain Lipids on Membrane Phase Behavior and Nanodomain Formation 84
5.1 Abstract 86
5.2 Introduction 87
5.2 Materials and Methods 89
5.2.1 Materials 89
5.2.2 Confocal Fluorescence Microscopy 90
5.2.3 Fluorescence Spectroscopy 91
5.2.4 Cryo-EM Imaging 92
5.3 Results and Discussion 94
5.3.1 Macroscopic phase behavior from fluorescence imaging 96
5.3.2 Miscibility transition temperature from fluorescence imaging 99
5.3.3 Nanoscopic phase behavior from cryo-EM imaging 99
5.3.4. Miscibility transition temperature from FRET spectroscopy 102
5.3.4. Nanoscopic $Tmisc$ is higher than macroscopic $Tmisc$ 104
5.4. Summary and Conclusion 106
Conclusions and Future Directions 108
6.1 Conclusions 109

List of References 112
Appendices 140
Vita 169

LIST OF TABLES

Table 1.1) Summary of the advantages, disadvantages, and suitable applications of the different methods discussed in [91]. This table is reproduced from [91] under the form of CC-BY-4.0. 20

Table 1.2) Model membrane sizes with applications and methods from literature. 26

Table 2.1) Interdigitation Quantified by Various Methods reused from[4] by the terms of CC-BY-4.0. 42

Table 5.1) Analysis of cryo-EM images of LUVs. 102

Table A2.1) Interdigitation and structural parameters of simulated bilayers. Listed are the results from memIT, nISA, ccMat and doMat (both the total matrix sums and individual quadrant sums), the average area per lipid and average phosphate-to-phosphate distance (PP-dist). Errors are calculated from block averaging as described in Appendix 2.4. 142

Table A2.2) Correlation times of interdigitation dynamics. Fluctuations in nISA and ccMat were fit with a double exponential decay (Figure A2.3). Shown are the respective correlation times and errors calculated from the fits (using Mathematica's NonlinearLeastSquares[257] function)..... 143

Table A3.3) Interdigitation values for mixed-chain lipids..... 153

Table A3.4) R^2 of second degree polynomial fits for interdigitation values· 155

Table A3.5) R^2 values for normalized backbending versus normalized interdigitation. 156

Table A3.6) R^2 of second degree polynomial fits for backbending counts. 156

Table A4.7) $\boldsymbol{Tmisc}$ determined by FRET Curves 162

LIST OF FIGURES

Figure 1.1) Phospholipid structure and molecular shape. (a) Chemical structure of a representative phospholipid containing one saturated and one unsaturated acyl tail. The organic substituent group (X) attached to the phosphate determines the headgroup identity. (b) Based on the size and shape of the headgroup and tails, phospholipids adopt one of three general molecular shapes: cylindrical (top), conical (middle), or inverted conical (bottom). 5

Figure 1.2) Lipid membrane phases. The Ld phase (left) forms when lipids are above their melting temperature. Sterols increase acyl chain order, leading to the Lo phase. Below the melting temperature, lipids form the Lβ phase, which becomes more fluid with the addition of sterol by disrupting chain. This figure is adapted from [38] with the terms of a CC-BY-4.0 license. 7

Figure 1.3) Schematic of lipid raft structure. Lipid rafts are rigid domains and enriched in saturated lipids, sphingomyelin and cholesterol. These regions are more ordered and rigid compared to the surrounding non-raft (liquid-disordered) regions, which are enriched in unsaturated phospholipids, contain lower levels of cholesterol, and are typically thinner than the raft domains. This figure has been adapted from [46] under the terms of the Creative Commons Attribution (CC BY 4.0) license 9

Figure 1.4) The leaflets of the PM have a lipid imbalance. (a) Lipidomic analysis shows that the outer leaflet is enriched in PC and SM, but overall contains significantly fewer lipids compared to the inner leaflet. (b) Quantitatively, the outer leaflet has nearly half the total phospholipid content of the inner leaflet. This figure is reused from [60] with permission from Springer. 13

Figure 1.5) Structures of a DPPC molecule in the Cooke model, Martini CG model, and AA representation. (Left) In the Cooke model, a lipid is represented by three beads: one headgroup bead (green) and two tail beads (pink). (Middle) In the Martini CG model, multiple atoms are mapped to a single bead. For DPPC, a 4:1 mapping scheme results in 12 beads. (Right) In the AA model, each atom in the DPPC molecule is explicitly represented, totaling 130 atoms. 14

Figure 1.6) Different periodic boundary conditions (PBCs) used in bilayer simulations. (a) Standard P1 PBCs commonly used in MD simulations of lipid bilayers. When a lipid exits the unit box from one side it reappears on the opposite side in the same leaflet, prohibiting free exchange of lipids between leaflets. (b) Modified $P2_1$ PBCs where the primary simulation cell is rotated and translated to allow free passage of lipids between leaflets. When a lipid exits the unit box from one side it reappears in the opposite leaflet via an orthogonal face allowing sampling of both leaflet environments. Schematics on the left in (A,B) were adapted with permission from [] and illustrate the lipid headgroups on the two leaflets. This figure is used from [91] under the terms of the Creative Commons Attribution 4.0 license..... 17
Figure 1.7) Dual probe method for SP-FRET in lipid membranes. Starting with a uniformly mixed (b), if the two probes prefer different phases they separate and FRET signal intensity decreases (a). If the two probes prefer the same phase, decreasing the temperature increases FRET signal intensity. This figure is from [140] and reused with permission from the American Physical Society 30
Figure 2.1) Figure 1. Schematic illustration of interdigitation quantified by the normalized interfacial surface area (nISA) and the Interdigitation tool in MEMBPLUGIN (memIT, see Appendix A2.1). (a) nISA is calculated as the midplane surface area (in red) divided by the lateral bilayer area. In the absence of interdigitation, the interfacial surface area per lipid is equal to the average area per lipid and nISA = 1. memIT, quantified by the overlap of the total mass density profiles of the top (orange) and bottom (blue) leaflets, is also shown as a gray shaded area. (b) Increased interdigitation in a mixed-chain bilayer results in a greater mass density overlap and a more dimpled midplane surface, leading to an increase in both memIT (larger mass density overlap) and nISA (larger interfacial surface). ... 38
Figure 2.2) Interdigitation quantified with nISA. (a) 3D visualization of the interleaflet contact surface of DPPC from a representative trajectory frame. The surface is defined as the set of Voronoi cell faces shared by neighboring interleaflet atom pairs as described in Methods. (b) Contact surfaces shown as 2D intensity maps of $|z|$ where darker shades correspond to greater interdigitation of acyl chains for DPPC

and MSPC. (c) Interfacial surface area per lipid is correlated with the average area per lipid across all bilayers (correlation of 0.75). (d) Time autocorrelation function of nISA calculated for MSPC (solid line) and its best fit to a double exponential function (dashed line). Inset shows the raw data as a function of time. (e) Slow correlation times for nISA and ccMat for the three bilayers. Data and fits are shown in Appendix 2.1 and Appendix 2.3 39

Figure 2.3) Matrix-form quantification of lipid interdigitation in DPPC (left) and MSPC (right) bilayers. Quadrants correspond to interactions between carbon atoms in the *sn*-1 and *sn*-2 chains of opposing leaflets as indicated in the cartoons on the left. (a) Carbon contact matrices (ccMat) where each matrix element represents the time-averaged number of close contacts for the specific interleaflet carbon pair. (b) Atomic density overlap matrices (doMat) where each matrix element represents the overlap of time-averaged atomic number density profiles for the interleaflet carbon pair calculated from Eq 2.2. The mean quadrant sums are indicated in the corresponding four corners of each matrix and their errors are listed in Appendix 2.1..... 44

Figure 3.1) Lipids in this study. From left to right, the sn-1 chain increases in carbon number while the sn-2 chain decreases to maintain a total of 32 acyl chain carbons. 58

Figure 3.2) APL and Bilayer Thickness of Mixed Chain Lipid Bilayers. (a) APL for lipid bilayers with increasing chain mismatch. The lipid with the highest chain length difference has the highest APL. Knowing that the higher APLs form thinner bilayers, the trend agrees in (b) where the APL and bilayer thickness are inversely proportional. 59

Figure 3.3) Mechanical properties of mixed chain lipid bilayers. (a) is the bilayer $\boldsymbol{KA}$ for each of the mixed chain bilayers. (b) is $\boldsymbol{\kappa}$ for each of the mixed chain bilayers. $\boldsymbol{KA}$ and $\boldsymbol{\kappa}$ are positively correlated. Mixed-chain lipid bilayers maintain this trend (c). 61

Figure 3.4) Average order parameters for *sn*-1 and *sn*-2 chains. The values represent the mean order parameters across the entire acyl chains, plotted as a function of acyl

chain length and backbone position. Increasing chain length reveals differences in backbone positioning associated with disorder..... 62
Figure 3.5) PBM values for mixed-chain bilayers. Increasing chain-length mismatch does not significantly alter the mechanical coupling constant, despite observable differences in other mechanical properties 64
Figure 3.6) Quantification of interdigitation using four methods: ccMat, doMat, memIT, and nISA. All methods consistently show that increasing ΔCL results in greater interdigitation. Panels show (a) ccMat sums, (b) doMat sums, (c) memIT values, and (d) nISA values. While the absolute values differ across methods, normalization reveals highly similar trends (Appendix 3.5)..... 65
Figure 3.7) Average number of backbending acyl chains as a function of increasing fractional chain length threshold. Reducing the threshold from 70% to 60% of the maximum chain length (panel a) results in over a 50% decrease in the number of identified backbending chains. Despite changes in threshold criteria (down to 50% and 40%), SMPC consistently exhibits the highest number of upward-snorkeling chains. Fitting the data with a second-order polynomial reveals a strong correlation between backbending and carbon chain-length difference..... 67
Figure 4.1) Dual probe partitioning in SP-FRET. (a) For two probes that prefer the same phase, at lower temperature regimes, the FRET intensity is going to be higher. Conversely, if two probes prefer different phases, in lower temperature regimes, then FRET intensity will be lower. (b) In temperatures above the miscibility temperature, then the sample and probes are uniformly mixed. (c) This figure is an adaptation from [140] with permission from American Physical Society..... 73
Figure 4.2) Model Fits for a uniform, nanoscopic, and macroscopically phase-separated system. (a) 100% DOPC fit with all three models. Interpreting differences between the 4- and 5-parameter model fits is not phenomenologically justified in this case, as the system is compositionally uniform and lacks detectable phase heterogeneity. However, in both (b) DPPC/POPC/Chol and (c) DPPC/DOPC/Chol the $\boldsymbol{Tmisc}$ determined by the 4-parameter model is shown with an orange vertical line and the $\boldsymbol{Tmisc}$ determined by the 5-parameter model is shown with a green vertical line.

Each sample had 10 replicates, and the error bars are standard error of the mean. The error is determined from the error of the parameter in a weighted fit model. 80
Figure 4.3) Model Fits for ternary DOPC/DPPC/Cholesterol system at a fixed 1:1 DPPC:DOPC ratio and varying cholesterol concentration. Each $\boldsymbol{FRatioT}$ curve was fit with all three models and the best fit model was determined by $\boldsymbol{\chi red2}$ratio. The black vertical lines are the determined $\boldsymbol{Tmisc}$ values..... 81
Figure 4.4) Weighted curves for 100% DOPC, DPPC/POPC/Chol (40/40/20mol%) and DPPC/DOPC/Chol (40/40/20mol%). Column (A) is 100% DOPC weighted curve for FRET 1 (row 1), FRET 2 (row 2) and FRET Ratio (row 3). Each curve is fit with the 3 (blue dash), 4 (orange dash), and 5 parameter (green solid) model. Column (B) is DPPC/POPC/Chol (40/40/20mol%) and column (C) is DPPC/DOPC/Chol (40/40/20mol%). The error bars are standard error of the mean. Each composition had 10 sample replicates. 83
Figure 5.1) High-T_M lipids in this study. From left to right: DMPC (14:0-14:0 PC); 15:0-PC (15:0-15:0PC); DPPC (16:0-16:0PC); DSPC (18:0-18:0PC); SMPC (18:0-14:0PC); and MSPC (14:0-18:0 PC). 95
Figure 5.2) Confocal fluorescence images of GUVs at 22°C. Shown are slices near the GUV cap for three-component mixtures containing 1:1 high-T_M/DOPC with increasing Chol mol% and different high-T_M lipid as indicated: MSPC (top row); 15:0-PC (middle row); and SMPC (bottom row). GUVs were labeled with fluorescent dyes LRPE (red) and NBD (green). Each image shows the composite of the red and green channels. Scale bar is 5 µm. 97
Figure 5.3) Phase behavior of GUVs at 22°C. Shown are ternary plots of GUV phase behavior for: MSPC/DOPC/Chol (a); 15:0-PC/DOPC/Chol (b); and SMPC/DOPC/Chol (c). Each point in the diagram shows the predominant phase behavior at a specific composition: blue triangles indicate Ld+Lß phase coexistence, green circles indicate Ld+Lo phase coexistence, red circles indicate uniform mixing, and black asterisks indicate compositions that showed approximately equal populations of phase-separated and uniformly mixed vesicles..... 98

Figure 5.4) Representative sigmoidal fits for ternary mixtures used to determine $\boldsymbol{Tmisc}$ from CFM data. Each plot displays the fraction of phase-separated vesicles as a function of temperature, fitted with a sigmoidal curve to extract $\boldsymbol{Tmisc}$. Shown are data from one of the three experimental replicates 100

Figure 5.5) Cryo-EM images of ternary LUVs. All compositions are 40/40/20 mol%: DPPC/DOPC/Chol (a); MSPC/DOPC/Chol (b); 15:0-PC/DOPC/Chol (c); and SMPC/DOPC/Chol (d). Shown is a representative vesicle for each composition without (top row) and with (middle row) an overlay of the local bilayer thickness, D_{TT}, as indicated by the color scale bar. Black image scale bars are 50 nm. Plotted in the bottom row are histograms of local bilayer thickness calculated as described in Methods, with the total number of vesicles contributing to each histogram denoted by *n*..... 101

Figure 5.6) Average FRET ratio data for DOPC and ternary mixtures with model fits. (a) FRET ratio vs temperatures for DOPC (black circles) and high-T_M/DOPC/Chol 40/40/20 mol% for the high- T_M lipids: DMPC (blue diamonds), SMPC (orange triangles), 15:0-PC (green upside-down triangles), MSPC (red squares), DPPC (purple stars) and DSPC (brown right-pointing triangles). The solid lines represent the best fit to the uniform model for DOPC and the phase-separated model for ternary mixtures as described in Methods. Vertical lines indicate the best-fit value of $\boldsymbol{Tmisc}$ determined from the model fits. Error bars are standard deviations determined from 10 sample replicates for DOPC, SMPC/DOPC/Chol, and DPPC/DOPC/Chol and 3 sample replicates for all other compositions 105

Figure 5.7) Comparing miscibility transition temperatures determined fluorescence microscopy and spectroscopy. Panel a shows $\boldsymbol{Tmisc}$ values determined from FRET (vertical axis) and CFM (horizontal axis) for each mixture. The dashed line shows a linear fit ($R^2 = 0.96$) to the data points for mixtures with symmetric-chain high-T_M lipids (i.e., DMPC, 15:0-PC, DPPC, and DSPC). Panel b plots $\boldsymbol{Tmisc}$ determined from FRET (filled symbols) and CFM (open symbols) for the ternary mixtures vs. the main chain transition temperature, T_M, of the high-T_M lipid. 107

Figure A2.1) Autocorrelation functions of nISA (top) and ccMat (bottom) for each simulated bilayer (gray). Shown on each plot are the corresponding best fits with a single exponential (dashed color line) vs double exponential (solid color line) decay. The resulting correlation times from the double exponential fits are listed in Appendix 2.2. 144
Figure A2.2) Interdigitation in simulated bilayers quantified with different methods. Shown for each method are: the spread in the values from individual frames (for memIT, nISA and ccMat) or consecutive blocks of ~1000 frames (for doMat); their mean and effective standard error of the mean calculated from block averaging as detailed in Supplemental Methods; and the *p*-values for comparisons of the results for $DPPC_T$ and MSPC against those for the DPPC bilayer. 146
Figure A2.3) Maps of shared Voronoi faces between atoms in opposing leaflets in DPPC (a) and MSPC (b) from the same trajectory frames as in Figure 2.2. Different maps correspond to (from top to bottom): all atom pairs, *sn*-1/*sn*-1 pairs, *sn*-2/*sn*-2 pairs, and *sn*-1/*sn*-2 pairs. Each map is 80 × 80 Å. 147
Figure A2.4) Correlation between bilayer thickness (phosphate-to-phosphate distance, PP-dist) and area per lipid (APL) in the three simulated bilayers. Each data point represents a single frame from the corresponding trajectory 148
Figure A2.5) Interdigitation in the $DPPC_T$ bilayer quantified with ccMat (A) and doMat (B). Shown are the average results from each method as matrices following the format of Figure 2.3 in the main text. Errors for the quadrant sums are listed in Appendix 2.1. 149
Figure A3.6) Backbending cutoff distances for chain length distances. (a) DPPC is shown with the maximum chain length highlighted in black. The thresholds in this study are defined by a percentage of this maximum distance from the carbonyl carbon and the center of mass of the terminal methyl group. (b) Histogram of *sn*-1 and *sn*-2 chain length distances. The superimposed vertical lines represent the respective thresholds of the study 150
Figure A3.7) Acyl chain order parameters for mixed chain lipids. The deuterium order parameters were calculated for each lipid. The average order parameter for each

carbon is shown with the *sn*-1 and *sn*-2 plotted separately. The legend applies for both panels. Overall, the *sn*-2 chains are more disordered. 151
Figure A3.8) Bending rigidity and APC from this study and Doktorova et al..[107] The relationship of APC and $\boldsymbol{\kappa}$ is well known. These mixed chain lipids follow the trend. Shown in gray are lipids from a previous method application in ref[107] both saturated and unsaturated systems. SMPC behaves similarly to some unsaturated species, while the rest of the mixed chain lipids behavior mimics other saturated lipid systems. 152
Figure A3.9) Second-order polynomial fits for interdigitation and backbending as a function of acyl chain length mismatch. (Left): Interdigitation shows a quadratic correlation with the difference in carbon numbers between the two acyl tails in mixed-chain lipids. Each interdigitation method was fit with a second-order polynomial; corresponding R^2 values are provided in Appendix Figure 3.5. (Right): Counts per frame of backbending acyl chains also exhibit a second-degree polynomial relationship with the difference in carbon number between the *sn*-1 and *sn*-2 chains. Each maximum chain length threshold was independently fit, with R^2 values reported in Appendix 3.6 154
Figure A4.1) Probe excitation and emission spectra and collection channels. Spectra of Naph and DiD probes. Dashed vertical lines indicate the emission wavelength collection channels for Naph (545 nm) and DiD (664 nm), while solid vertical lines mark the excitation wavelengths (Naph: 427 nm; DiD: 646 nm). (bottom) Spectra of TFPC and DiD probes. Dashed vertical lines represent the emission collection channels for TFPC (551 nm) and DiD (664 nm), and solid vertical lines indicate the excitation wavelengths (TFPC: 499 nm; DiD: 646 nm). In both panels, the red shaded regions highlight the spectral overlap between the donor emission and acceptor excitation—an essential condition for FRET. However, excessive overlap can lead to spectral cross-talk. The collection channels for FRET excitation and emission are shown with solid black lines. 157
Figure A4.2) FRET1 and FRET2 data for single-component DOPC. The plot shows weighted FRET intensity values for 10 sample replicates for 100% DOPC system.

The error bars on the plots are found by the standard error of the mean. The gradual increase in intensity is because of quantum yield and not the phase behavior. 158
Figure A4.3) $\boldsymbol{\chi red2}$ for all sample replicates for 100% DOPC, DPPC/POPC/Chol (40/40/20mol%), and DPPC/DOPC/Chol (40/40/20mol%). (a) shows that for uniform samples show no significant different in the between models. In the phase-separated systems, (b) (DPPC/POPC/Chol) and (c) (DPPC/DOPC/Chol) there is a distinct difference in the $\boldsymbol{\chi red2}$. The differences in (b) are smaller than in (c) suggesting the nanoscopic mixture has increase fitting noise compared to macroscopic heterogeneity..... 159
Figure A4.4) Ratios of $\boldsymbol{\chi red2}$ for all sample replicates for 100% DOPC, DPPC/POPC/Chol (40/40/20mol%), and DPPC/DOPC/Chol (40/40/20mol%). Both ratios show that for uniform samples the ratio of is ~1. In the phase-separated systems, (DPPC/POPC/Chol) and (DPPC/DOPC/Chol) there is a distinct increase in the ratios when compared to uniform DOPC. In the phase-separated systems (DPPC/POPC/Chol) and (DPPC/DOPC/Chol), there is a distinct increase in the χ^2 ratios compared to the DOPC control. The p-values and $\boldsymbol{\chi red2}$ ratios indicate that both ternary mixtures exhibit phase separation. Furthermore, the 5-parameter model (A) provides a statistically improved fit over the 4-parameter model (B), supporting its utility in capturing nanoscopic heterogeneity. 160
Figure A4.5) $\boldsymbol{FRatio}(\boldsymbol{T})$ for the 1:1 line of DPPC/DOPC/Chol with increasing cholesterol concentration. Each line is an independent FRET experiment with a distinct amount of cholesterol. All experiments were fit with the 3(dark gray dashed),4 (black dashed), and 5 (light gray solid) parameter models. 161
Figure A5.1) GUV $\boldsymbol{Tmisc}$ experiment for SMPC/DOPC/Chol. Images of GUVs for a three-component system SMPC/DOPC/Chol (40/40/20mol%) starting from 17°C to 23°C. GUVs were labelled with fluorescent dyes LRPE (red) and 18:0 NBD (green). GUVs were prepared by electro-formation method and imaged on VA Heat substrate. Arrows indicate a representative vesicle, with dashed arrows marking its phase-separated state and a solid arrow indicating the transition to a uniform state. Each image presented is the fluorescence collected from both green and red channel

using Image J. The data is then fitted in a sigmoidal fit shown in [Eq 1] to precisely calculate $\boldsymbol{Tmisc}$. Scale bars are 10μm 163
FigureA5.2) Full field-of-view cryo-EM images of ternary liposomes. The first row is an overlay with thicknesses determined from the I(w) profiles. The bottom row is the full field of view with no overlay. Column (A) is DPPC/DOPC/Chol (40/40/20), (B) MSPC/DOPC/Chol (40/40/20), (C) is 15:0-PC/DOPC/Chol (40/40/20), (D) is SMPC/DOPC/Chol. 164
Figure A5.3) Representative FRET data for 40/40/20 mol% DOPC/DPPC/Cholesterol. The top panel shows FRET intensity for Pair 1 (Nap to DiD), which decreases with decreasing temperature due to the probes preferring different phases. The middle panel displays FRET intensity for Pair 2 (TF-PC to DiD), which increases with decreasing temperature as both probes partition into the same phase. The bottom panel presents the FRET ratio (Pair 1/Pair 2), which enables accurate determination of $\boldsymbol{Tmisc}$ 165
Figure A5.3) Model fits and $\chi\boldsymbol{red2}$ ratios for FRET samples. Panel a shows FRET ratio data for DOPC and ternary mixtures with uniform and phase-separated model fits. Average FRET ratio for DOPC, and 40/40/20 mol% ternary mixtures fit with uniform model fits (dashed lines) and phase-separated model fits (solid lines). Each plot is a minimum of 3 replicates. In each of the ternary mixtures, the best fits came from the phase-separated models. The best fitting models are shown in (a). (b) and (c) shows the reduced chi-squared ($\chi\boldsymbol{red2}$) for 10 sample replicates of uniform (DOPC) and phase-separated (40/40/20 mol % DPPC/DOPC/Chol) model fits respectively. The DOPC replicates have no significant difference in the value between the phase-separated and uniform model. However, in (c) the phase-separated model fits significantly better than the uniform model for all 10 replicates. 166

LIST OF ABBREVIATIONS

ABBREVIATIONS	DEFINITION
PM	Plasma Membrane
MCL	Mixed Chain Lipids
SM	Sphingomyelin
PA	Phosphatidic Acid
PE	Phosphatidylethanolamine
PI	Phosphoinositide
PC	Phosphatidylcholine
FMM	Fluid Mosaic Model
Ld	Liquid-Disordered
Lβ	Solid Ordered (Gel) Phase
GPMV	Giant Plasma Membrane Vesicle
RBC	Red Blood Cell
MD	Molecular Dynamics
AA-MD	All-Atom Molecular Dynamics
CG	Coarse-Grained
PBC	Periodic Boundary Conditions
SMPC/18:0-14:0 PC	1-stearoyl-2-myristoyl-sn-glycero-3-phosphocholine
DSPC/18:0-18:0 PC	1,2-distearoyl-sn-glycero-3-phosphocholine
RSF	Real Space Fluctuation
PMF	Potential of Mean Force
High-T_M	High-melting
Low-T_M	Low-melting
Chol	Cholesterol
SLB	Supported Lipid Bilayer
GUV	Giant Unilamellar Vesicle
MLV	Multilamellar Vesicle
LLV	Low Lamellarity Vesicle
SUVs	Small Unilamellar Vesicles
T_m	Main Chain Transition Temperature
FRET	Förster Resonance Energy Transfer
SANS	Small Angle Neutron Scattering
Cryo-EM	Cryogenic Electron Microscopy
CFM	Confocal Fluorescence Microscopy
nISA	Normalized Interfacial Surface Area
ccMat	Carbon Contact Matrix
doMat	Density Overlap Matrix
memIT	MEMPLUGIN Interdigitation Tool
MSPC/14:0-18:0 PC	1-myristoyl-2-stearoyl-sn-glycero-3-phosphocholine

15:0-17:0 PC	1-pentadecanoyl-2-heptadecanoyl-sn-glycero-3-phosphocholine
17:0 -15:0 PC	1-heptadecanoyl-2-pentadecanoyl-sn-glycero-3-phosphocholine
DPPC/16:0-16:0 PC	1,2-dipalmitoyl-sn-glycero-3-phosphocholine
VMD	Visual Molecular Dynamics
VT	Voronoi Tessellation
NDP	Number Density Profile
APC	Area per Chain
S_{CD}	Order Parameter
K_A	Area Compressibility Modulus
PBM	Polymer Brush Model
β	Mechanical Coupling Constant
κ	Bending Modulus
DOPC	1,2-dioleoyl-sn-glycero-3-phosphocholine
POPC	1-palmitoyl-2-oleoyl-sn-glycero-3-phosphocholine
SP-FRET	Steady-State Probe Partitioning FRET
D	Donor
A	Acceptor
T_{misc}	Miscibilty Temperature
χ^2_{red}	Reduced Chi-Squared
TFPC	1-palmitoyl-2-(dipyrromethene boron difluoride)undecanoyl-*sn*-glycero-3-phosphocholine
DiD	1,1′-dioctadecyl-3,3,3′,3′-tetramethylindodicarbocyanine, 4-chlorobenzene sulfonate salt
Naphthopyrene/Naph	naphtho[2,3-*a*]pyrene
RSE	Rapid Solvent Exchange
FRET1	Naph-DiD FRET
FRET2	TFPC-DiD FRET
F_{Ratio}	FRET2/FRET1
DMPC	1,2-dimyristoyl-sn-glycero-3-phosphocholine

LRPE	1,2-dioleoyl-sn-glycero-3-phosphoethanolamine-N-(lissamine rhodamine B sulfonyl) (ammonium salt)
NBD-DSPE/NBD	1,2-distearoyl-sn-glycero-3-phosphoethanolamine-N-(7-nitro-2-1,3-benzoxadiazol-4-yl) (ammonium salt)
D_{TT}	Trough to Trough Distance from Cryo-EM
gA	Gramicidin A

CHAPTER ONE
BACKGROUND AND INTRODUCTION

A portion of Section 1.4.4 and a version of Section 1.4.4 and 1.4.5 were originally published as written below and is reused under the Creative Commons Attribution 4.0 license.

Emily H. Chaisson, Frederick A. Heberle, Milka Doktorova "Building asymmetric lipid bilayers for molecular dynamics simulations: What methods exist and how to choose one?" Membranes 2023, 13(7), 629

This section is from a review of “How to build compositionally asymmetric bilayers for molecular dynamic simulations and how to choose the proper method”. The preparation of the review was completed by Frederick A. Heberle, Milka Doktorova, and **Emily H. Chaisson**.

1.1 Motivation

Lipid bilayers are crucial semi-permeable membranes found in numerous biological contexts. These membranes are essential for the viability of both eukaryotes and prokaryotes. Arguably, the most vital membrane for both domains is the plasma membrane (PM). The PM is the specific membrane that encapsulates the cytoplasm. In eukaryotes, the PM serves as a cell's first line of defense against the external environment and plays a vital role in many biological processes.[1] One reason for the PM's high functionality is its complexity. The PM is comprised of hundreds of structurally distinct lipids and thousands of different proteins.[2] As the PM is primarily composed of phospholipids[3], understanding lipid-lipid interactions is crucial for deciphering its complexity.

To begin, comprehending the fundamental biophysical properties of specific lipid subclasses provides a foundation for more complex studies, such as membrane asymmetry, protein function, and even drug delivery. One subclass of lipids hypothesized to affect bilayer properties consists of lipids in which the number of carbons in one acyl chain differs from that in the other, or mixed-chain lipids (MCL).[4-6] In some cases, this difference can be substantial, as seen in particular In some cases, this difference can be substantial, as seen in particular sphingomyelins (SMs), where the sphingosine backbone typically contains 18 carbon atoms, and the N-acyl chain can vary from as short as 14 to as long as 40 carbons — leading to a carbon number difference of up to 26 between different SM species.[7] Conversely, in other cases, the difference can be as minimal as one carbon. Even when the number of carbons in both chains is the same, the lipid's backbone tilt can result in a chain length mismatch. This mismatch is thought to impact bilayer properties by altering the midplane interactions between the bilayer's two leaflets.[4, 5] Since most biologically occurring lipids demonstrate a chain mismatch, elucidating the dynamics of a simplified model focused solely on acyl chain interactions will enhance our understanding of the highly complex PM.

1.2 Structural Basis of Membrane Heterogeneity

1.2.1 Lipid and Membrane Structure

Eukaryotic and prokaryotic cells both have a rich diversity of lipids, among which phospholipids are the most abundant.[3] Phospholipids consist of a polar headgroup (which includes a phosphate and a variable functional group that may carry a positive, negative, or neutral charge), a glycerol backbone, and hydrophobic acyl chains. The different headgroups vary in size, contributing to the distinct preferred molecular shapes seen in **Figure 1.1**. For example, smaller headgroups (i.e., phosphatidic acid, PA, phosphatidylserine, PS, and phosphatidylethanolamine, PE) prefer conical shapes, while larger headgroups (i.e., phosphoinositide, PI) prefer an inverted conical shape. Some lipids prefer cylindrical shapes (i.e., phosphatidylcholine, PC). Phospholipids are amphipathic molecules that usually contain a polar headgroup and two fatty acid tails, although some variants, such as lysophospholipids and cardiolipin, differ in tail number and structure. These tails can either be saturated (no double bonds) or unsaturated (at least one, typically cis, double bond). Because of their amphipathicity, most membrane phospholipids spontaneously form bilayers in aqueous environments, with their hydrophobic tails sandwiched between the hydrophilic headgroups. The specific molecular shape of each lipid, dictated by the relative size of its headgroup and tails, influences how these molecules pack together within membranes, ultimately determining bilayer structure.

Sterol lipids like cholesterol interact with phospholipid membranes to influence molecular packing and membrane remodeling.[8-11] Cholesterol is insoluble in water and readily incorporates itself into a lipid bilayer. Adding cholesterol to a membrane affects its packing density, alters fluidity, and decreases the area per lipid (APL) through the umbrella effect.[12-14] In this scenario, the bilayer must maintain a loose enough structure to allow cholesterol to enter while being held together by electrostatic interactions. These dynamic properties enable the membrane to function as a two-dimensional fluid, facilitating molecular diffusion both through and within the membrane.[3] As a lipid

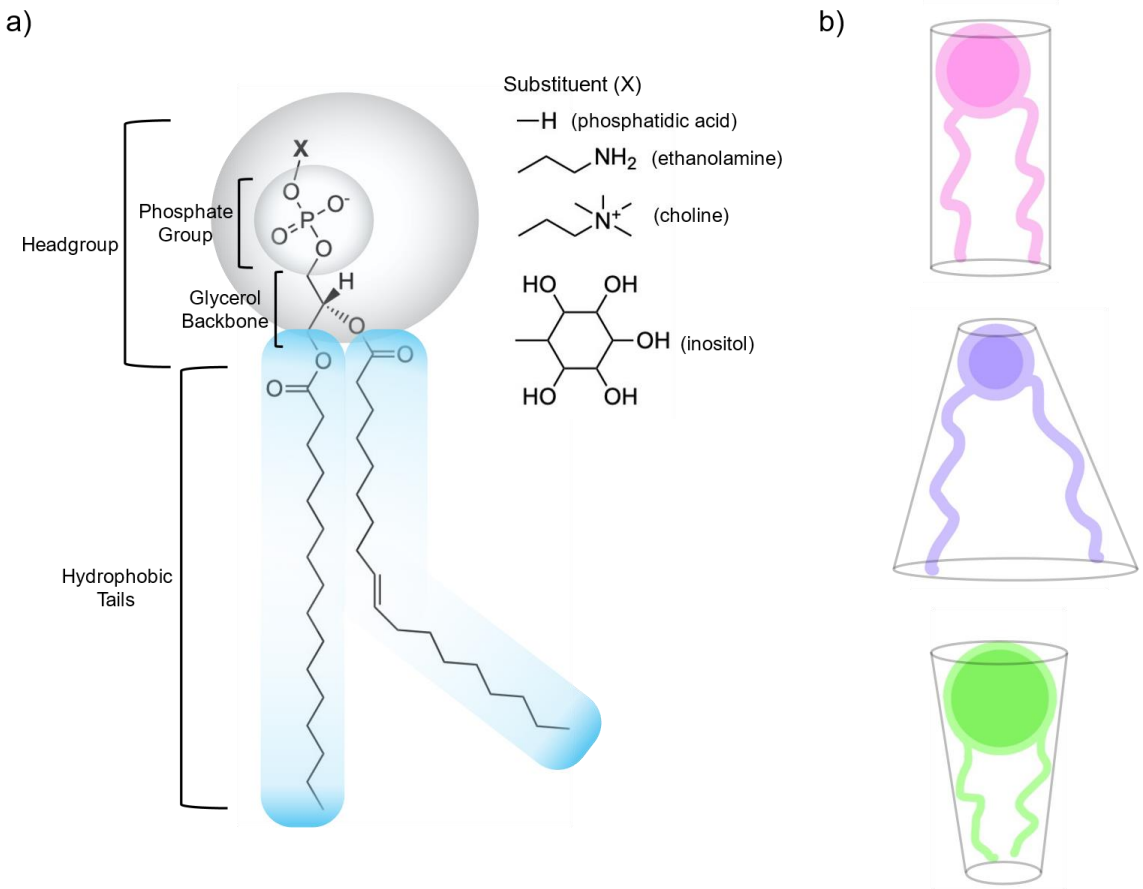


Figure 1.1) Phospholipid structure and molecular shape. (a) Chemical structure of a representative phospholipid containing one saturated and one unsaturated acyl tail. The organic substituent group (X) attached to the phosphate determines the headgroup identity. (b) Based on the size and shape of the headgroup and tails, phospholipids adopt one of three general molecular shapes: cylindrical (top), conical (middle), or inverted conical (bottom).

bilayer, the PM is highly advantageous due to its semi-permeable nature, which aids in molecular diffusion.

1.2.2 Lateral Lipid Heterogeneity and the Lipid Raft Hypothesis

Cell membranes have been hypothesized to be composed of lipids since the late 1800s, first proposed by Ernest Overton.[15] Since then, there has been a steady development of theories and experiments revealing how the PM can serve as such a vital barrier. In the early 1900s, several research groups demonstrated that the PM was not composed of only one specific lipid, but rather a variety of lipids—including PE, PI, and sphingolipids, along with some critical physical properties, such as deformability.[16-18] The growing recognition of lipid diversity and membrane adaptability encouraged the development of models that integrate both compositional complexity and dynamics, as shown experimentally. In 1972, Singer and Nicolson proposed the fluid mosaic model (FMM) to describe the overall organization of proteins and lipid types in biological membranes.[19] The FMM hypothesized that the PM is a complex and fluid lipid bilayer with proteins embedded throughout.[19]

Because the PM can be conceptualized as a two-dimensional fluid, regular solution theory can be applied.[20] Hildebrand's principle states that in a mixture of two distinct species, A and B, the interactions between A and B (i.e., A-B) are generally less favorable than self-interactions (i.e., A-A and B-B).[21, 22] These unfavorable interactions can lead to non-ideal mixing of A and B. In the context of lipid bilayers, this non-ideal mixing was termed raft formation, which led to the Lipid Raft Hypothesis by Simons and Ikonen in 1997.[23] When considering Hildebrand's principle, it becomes clear that in a mixture of hundreds of chemically distinct molecules, it is almost certain that similar species will co-localize. In lipids, this can lead to first-order phase separation that results in the segregation of lipids with highly unfavorable pairwise interactions (for example saturated, ordered lipids from unsaturated, disordered lipids). (**Figure 1.2**)

The "lipid rafts" Simons initially described were the ordered regions of the membrane enriched in SM and cholesterol. These areas suggest that rigid, ordered areas of the membrane, primarily composed of cholesterol and SM, are "floating in a sea" of

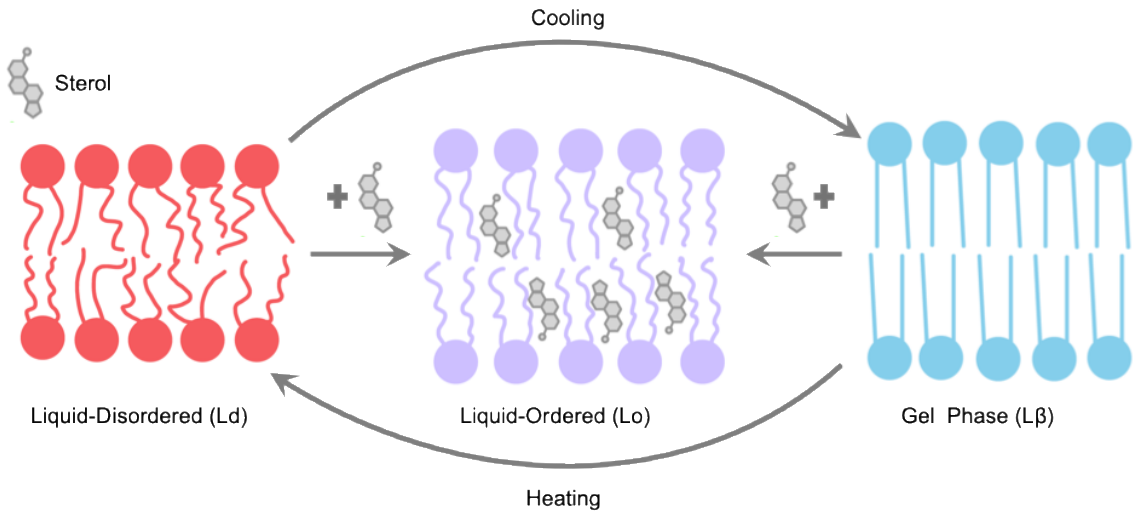


Figure 1.2) Lipid membrane phases. The Ld phase (left) forms when lipids are above their melting temperature. Sterols increase acyl chain order, leading to the Lo phase. Below the melting temperature, lipids form the Lβ phase, which becomes more fluid with the addition of sterol by disrupting chain packing. This figure is adapted from [38] with the terms of a CC-BY-4.0 license.

disordered lipids. (**Figure 1.3**) These rigid rafts are thought to possess distinct behavior and structure compared to membrane regions, such as being thicker and having increased packing density.[23-27] Due to their rigidity and density, it is thought that these rafts are ideal locations for cell signaling, protein and membrane sorting and trafficking, and viral entry and exit.[23, 26, 28]

1.3 The PM Is Asymmetric

1.3.1 The PM Has Lateral Heterogeneity

Lipid bilayers can exhibit multiple phases depending on lipid composition, temperature, and cholesterol concentration.[25, 29-37] In model membranes, unsaturated lipids generally form a thin, highly diffusive fluid phase due to acyl chains that exhibit a high degree of disorder, which is referred to as the liquid-disordered (Ld) phase.[7, 38-41] In contrast, saturated lipids below their melting point (T_M) tend to form a gel phase (Lβ), which is tightly packed, thicker and has low diffusivity.[42] The presence of cholesterol, which preferentially associates with saturated lipids, transforms the Lβ phase into the liquid-ordered (Lo) phase.[37, 38] The Lo phase, like the Lβ phase is thick and less diffusive when compared to the Ld phase.[27, 41, 43, 44] (**Figure 1.3**) While these phase behaviors are most clearly defined in simplified model membranes, they provide a useful framework for interpreting lateral heterogeneity in biological membranes. The Lo phase is thought to closely mimic raft-like regions of the plasma membrane, which are enriched in cholesterol and saturated lipids, while the Ld phase resembles the more fluid, non-raft regions composed primarily of unsaturated lipids.[45] A more detailed discussion of model membrane systems and phase behavior is provided in Section 1.5.

The lipid raft hypothesis proposes that the PM exhibits chemically distinct regions with distinctive properties. These properties differentiate more ordered, raft-like regions from the surrounding, more fluid non-raft areas. Raft-like regions are more ordered and rigid, whereas non-raft regions are relatively disordered and more fluid.[46] In living cells, these domains are generally nanoscopic in size [47, 48] Although some skepticism persists in the scientific community due to challenges in directly visualizing lipid rafts[49, 50], lateral heterogeneity has been seen in simulations[51], model membranes[8, 31, 34, 35, 52-55], and even

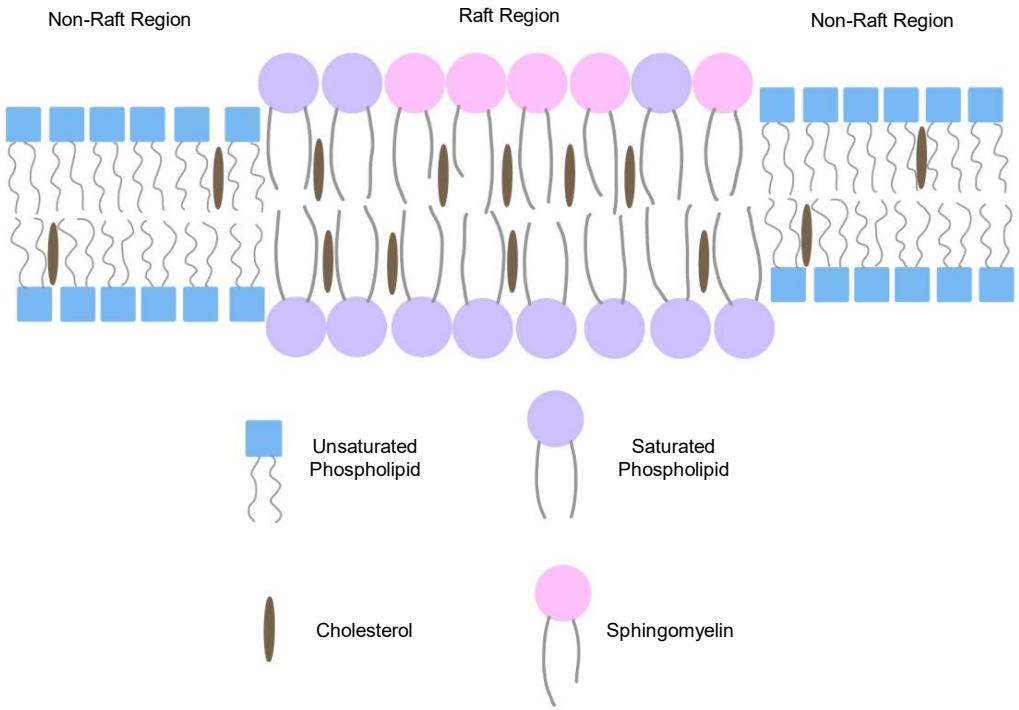


Figure 1.3) Schematic of lipid raft structure. Lipid rafts are rigid domains and enriched in saturated lipids, sphingomyelin and cholesterol. These regions are more ordered and rigid compared to the surrounding non-raft (liquid-disordered) regions, which are enriched in unsaturated phospholipids, contain lower levels of cholesterol, and are typically thinner than the raft domains. This figure has been adapted from [46] under the terms of the Creative Commons Attribution (CC BY 4.0) license

isolated PMs[50]. These findings suggest that, despite visualization challenges, lateral heterogeneity is biologically significant, particularly in processes such as membrane trafficking and signal transduction.[56]

1.3.2 The PM Leaflets Differ in Composition

The two leaflets of the PM differ in lipid composition, and this asymmetry is crucial for cell survival.[2, 57, 58] This leaflet asymmetry defies entropy and must be actively maintained. The cell requires significant amounts of energy, using enzymes to keep the lipids in place against their concentration gradients, aided by proteins such as flippases and floppases.[59, 60] This compositional asymmetry, while energetically costly, is essential for cell viability and function.[61] One study found that loss of membrane asymmetry can lead to cell death[61], which is relevant in the context of apoptotic signaling and immune clearance, where scramblase activation, scrambles PS lipids which primarily reside in the inner leaflet and marks the cell for phagocytosis.[62, 63]

Recent research has shown that headgroup charges are not the only structural differences between the lipid compositions of the two leaflets.[2] The inner (cytoplasmic) leaflet contains a significantly higher amount of charged lipids, while the outer (exoplasmic) leaflet is predominantly composed of uncharged or zwitterionic lipids. Additionally, the degree of unsaturation in the lipids also varies as shown in **Figure 1.4**.[2] Lorent et al. conducted a detailed lipidomic study revealing that lipids in the outer leaflet are more likely to have two or fewer double bonds in their acyl chains, while those in the inner leaflet usually have two or more double bonds in their acyl chains.[2] SM in the outer leaflet primarily has one or fewer double bonds in their acyl chains, suggesting even higher packing with cholesterol.[2, 58] Determining the placement of cholesterol in the PM is challenging due to the rapid rate of flip-flop it can undergo.[64] Between 60% and 80% of total cholesterol resides in the PM, and of that, almost 50% of the PM's lipidome is cholesterol.[65-67]

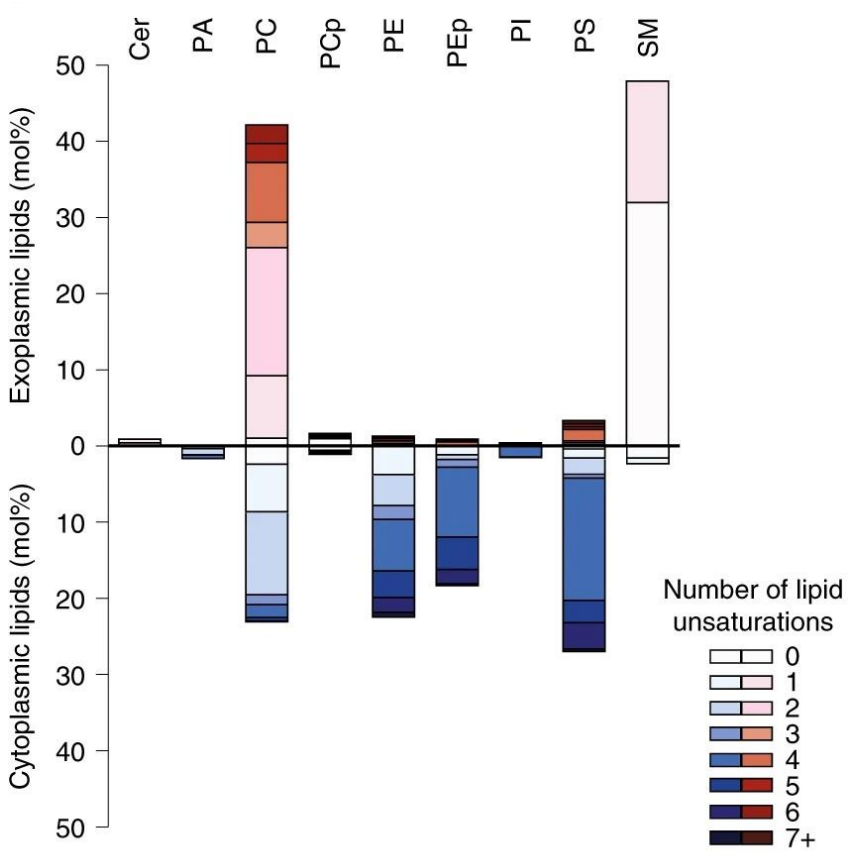


Figure 1.4) The outer leaflet of the PM is more saturated than the inner leaflet. The outer leaflet is enriched in PC and SM, which contain predominantly saturated acyl chains. In contrast, the inner leaflet is composed mainly of charged, unsaturated lipids, resulting in a marked asymmetry in lipid saturation across the bilayer. This figure is reused from [4] with permission from Springer.

1.3.3 The PM Has Lipid Number Asymmetry

It has long been established that the outer and inner leaflets of red blood cells (RBCs) possess distinctly different lipidomes.[68] These varying lipids have unique molecular shapes, indicating differing preferred curvature and packing between the two leaflets.[69, 70] Moreover, it has been hypothesized that cholesterol primarily resides in the outer leaflet due to its strong affinity for saturated phospholipids and SM.[71] Given the preferred molecular geometries and ideal APL for specific lipids, having an equal number of lipids in both leaflets may create a non-zero leaflet tension, known as differential stress which will be described later in Section 1.3.4, as a lipid may be compelled to assume a less-than-ideal shape or APL.[69, 72]

Doktorova et al. examined the location of cholesterol in lipid bilayers both in vivo and in vitro, finding that the majority of membrane cholesterol (~77%) resides in the outer leaflet.[58] This cholesterol imbalance arises because the cell needed to alleviate the differential stress that occurs since the outer leaflet contains significantly fewer phospholipids than the inner leaflet, as seen in **Figure 1.5**. This difference in the number of phospholipids introduces unique functionality into the membrane, such as increased permeability and resting tension in the cytosolic leaflet, which may aid in protein localization.[58] This cholesterol and phospholipid imbalance is another significant contributor to the diversity and robustness of the PM as a protective barrier for cells.

1.4 Molecular Dynamics (MD) Simulations to Study Model Membranes

1.4.1 MD Simulations Are Advantageous in Membrane Studies

MD simulations are incredibly powerful tools that offer insights into length and timescales that might be difficult to obtain through experiments. Since their inception in 1957, improvements in computational power and the development of force fields have significantly enhanced the effectiveness and complexity of MD simulations. For instance, all-atom MD (AA-MD) simulations represent every atom in a molecule, allowing researchers to track the movement of individual atoms or molecules over time. (**Figure 1.6**). This tracking enables the extraction of various properties such as velocities, positions, and dynamic behavior, all based on Newton's equations of motion.

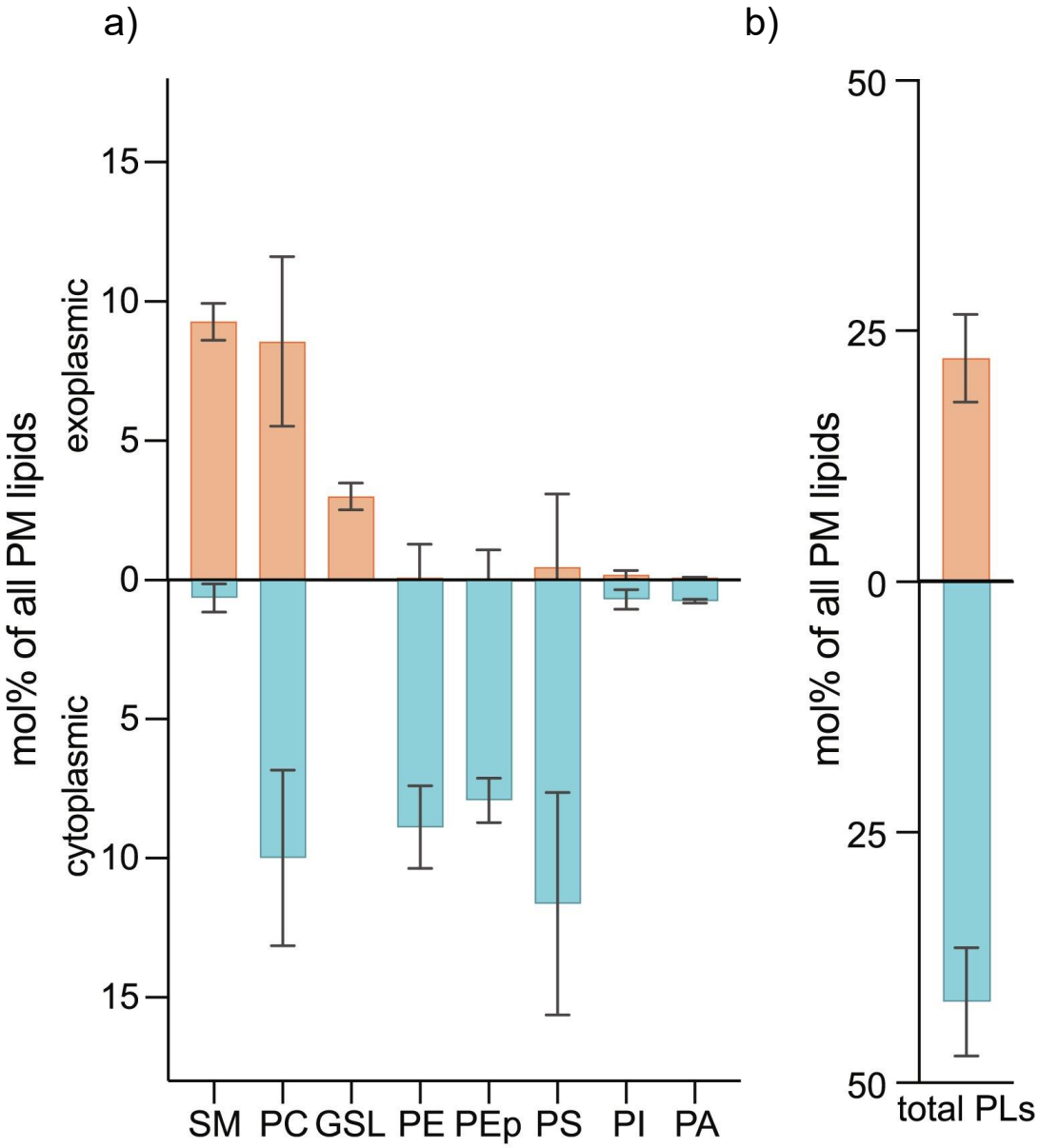


Figure 1.5) The leaflets of the RBC PM have a lipid imbalance. (a) Lipidomic analysis shows that the outer leaflet is enriched in PC and SM, but overall contains significantly fewer lipids compared to the inner leaflet. (b) Quantitatively, the outer leaflet has nearly half the total phospholipid content of the inner leaflet. This figure is reused from [60] with permission from Springer.

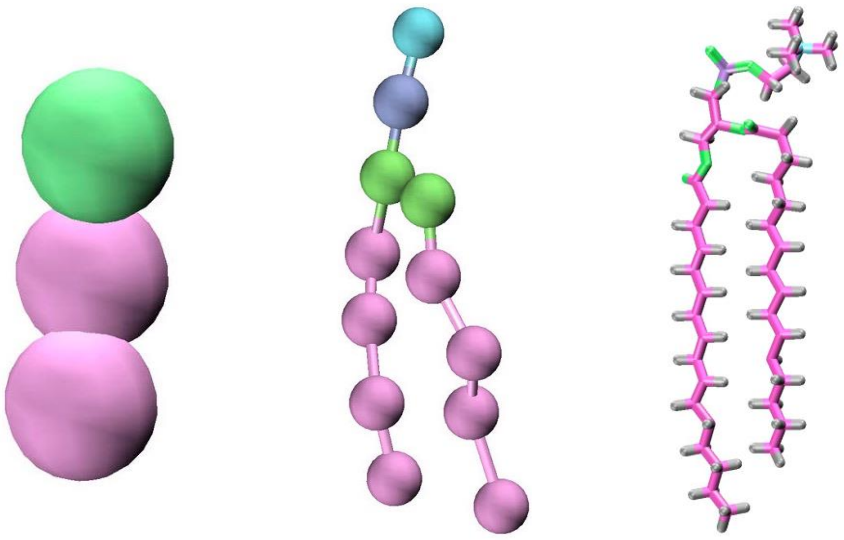


Figure 1.6) Structures of a DPPC molecule in the Cooke model, Martini CG model, and AA representation. (Left) In the Cooke model, a lipid is represented by three beads: one headgroup bead (green) and two tail beads (pink). (Middle) In the Martini CG model, multiple atoms are mapped to a single bead. For DPPC, a 4:1 mapping scheme results in 12 beads. (Right) In the AA model, each atom in the DPPC molecule is explicitly represented, totaling 130 atoms.

functions. These interactions include both strong, bound interactions (i.e., bond stretching and torsions) and weaker, unbound interactions such as van der Waals forces and electrostatic interactions. This comprehensive methodology facilitates an in-depth analysis of atomic-scale interactions, including phenomena like single lipid dynamics[73, 74], and hydrogen bonding in lipids.[75]

MD simulations have significantly advanced biological research, specifically by validating experimental results and uncovering biophysical characteristics. However, challenges arise in certain scenarios, such as phase separation, where the timescale and size of the system may not be accurately depicted in AA-MD simulations, even though they can extend to the microsecond timescale and average between 20,000 and 100,000 atoms.[75] In more complex biological systems, the size of the bilayer must be considerably larger to accurately represent bilayer or protein behavior. This increase in size can make simulations computationally expensive if every atom is modeled. To address this issue, a coarse-grained (CG) approach can be employed, which simplifies the representation by grouping atoms (usually 2 to 4) into a single bead. (**Figure 1.6**) This reduction in molecular complexity enables longer timescales, facilitating the study of compositionally asymmetric membranes and increasing the likelihood of adaptability to complex systems, such as compositionally asymmetric bilayers with induced differential stress.[76] Along with this reduction, comes certain compromises. CG simulations lack detailed local information and, as a result, are less likely to accurately capture the thermodynamic, structural, and dynamic properties of the system compared to AA-MD simulations.[77]

Applications of machine learning and artificial intelligence have introduced new opportunities for combining the speed of CG simulations with the detail of AA-MD.[78] The initial simulations are done in CG resolution, and when of interest, the portion of the simulation is then translated into increased AA-MD detail by a process called "backmapping".[78, 79] This approach enables researchers to efficiently explore large timescales and system sizes while still recovering atomistic resolution, offering significant advancements in multiscale biomolecular simulations.[78]

Basic biophysical principles also need to be explained or theorized to align with experimental observations. In some cases, an even more highly simplified model can be

useful for initial studies on biophysical phenomena. Cooke and Deserno developed a simplified MD model known as the Cooke model[80], which omits explicit water, uses simplified interactions, and represents a lipid as three beads. (**Figure 1.6**) Despite itssimplicity, this model successfully captures spontaneous bilayer formation, vesicle dynamics, and membrane remodeling.[81] This approach has proven to be particularly impactful for investigating various bilayer phases that may exist in energetic membranes, such as those found in mitochondria and thylakoid membranes.[81] Ultimately, MD simulations like these provide valuable insights into the fundamental aspects of membrane biophysics.

1.4.2 Building Bilayers and Modifying Lipid Structures from CHARMM-GUI

There are multiple ways to generate symmetric bilayer structures for MD simulations, the most common being CHARMM-GUI[82] and INSANE.py (INSert membrANE)[83] membrane builders. These methods are easy and user-friendly, including bilayer equilibration protocols. CHARMM-GUI is a web-based tool that allows users to construct biological systems for simulation, including simple membranes, all the way to complex membrane systems, including those with embedded proteins. Furthermore, CHARMM-GUI allows the user to set the boundary conditions including periodic boundary conditions (PBCs). PBCs implement a mathematical technique that mimics infinite box dimensions where the box is replicated in all directions (**Figure 1.7a**). The standard PBCs used in lipid bilayer simulations are referred to as P1 boundary conditions and are depicted in (**Figure 1.7a**). This treatment approximates an infinite membrane where lipids diffuse freely within the lateral plane of their respective leaflets. Transverse lipid diffusion (i.e., flip-flop) can occur spontaneously but is typically a rare event on the current timescales of atomistic simulations, consistent with experimental studies that report slow flip-flop rates (cholesterol is a notable exception)[84]. In contrast, a different type of PBCs referred to as $P2_1$ boundary conditions, allows lipids to readily exchange between leaflets as when they exit the unit cell from one side, they reappear not only on a different side but also on the opposite leaflet (**Figure 1.7**).[85] The $P2_1$ PBCs are currently implemented only in the CHARMM software[86] and allow for a specialized construction and simulation of asymmetric bilayers as discussed below in Section 1.4.5.

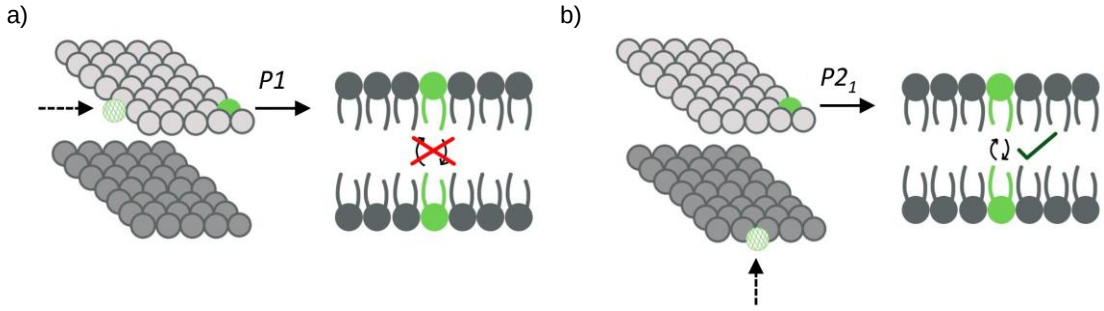


Figure 1.7) Different periodic boundary conditions (PBCs) used in bilayer simulations. (a) Standard P1 PBCs commonly used in MD simulations of lipid bilayers. When a lipid exits the unit box from one side it reappears on the opposite side in the same leaflet, prohibiting free exchange of lipids between leaflets. (b) Modified $P2_1$ PBCs where the primary simulation cell is rotated and translated to allow free passage of lipids between leaflets. When a lipid exits the unit box from one side it reappears in the opposite leaflet via an orthogonal face allowing sampling of both leaflet environments. Schematics on the left in (A,B) were adapted with permission from [85] and illustrate the lipid headgroups on the two leaflets. This figure is used from [91] under the terms of the Creative Commons Attribution 4.0 license.

The catalog of lipids readily available on CHARMM-GUI is not comprehensive and does not cover the entire lipidome of every species. Some lipids, including the ever-growing class of synthetic lipids, must be created from scratch or modified from other lipids, as testing and parameterizing them takes time. For instance, specific mixed-chain lipids were not readily available and were created for studies conducted between 2021[87, 88] and 2025[44] by modifying lipid structures from CHARMM-GUI built membranes. An example of a Tcl script to modify saturated chain symmetric lipids into saturated chain asymmetric lipids can be found in section **Appendix 1.1**.

1.4.3 Calculating the Lateral Pressure Profile for Lipid Bilayers

Because lipids are amphiphilic molecules, they spontaneously self-assemble into bilayers in aqueous environments. It is well-known that when species that are repulsive are pushed together, the pressure within the system increases. In the case of a lipid bilayer, the hydrophobic head groups are compressed. An individual lipid experiences compressive forces from neighboring lipids, which it also pushes against, while trying to shield its hydrophobic tails from the solvent.[89] As a result, these hydrophobic tails can experience some tension due to being confined between the hydrophilic head groups.

In symmetric bilayers, lipids arrange themselves in a way that minimizes the overall free energy of the system, resulting in no net tension in the plane of the bilayer. This means that the tension in each of the two monolayers is equal and opposite, effectively leading to zero net lateral tension in the bilayer.[90] Furthermore, in the absence of external forces, this balance extends even further: each individual leaflet in a symmetric bilayer is predicted to have zero tension, maintaining mechanical equilibrium across the membrane.[90, 91] However, there are still repulsive pressure components acting between the lipids, along with an overall net hydrophobic tension that encourages the lipids to segregate from the solvent. The amphipathic nature of lipid molecules results in these pressure components being inhomogeneously distributed throughout the bilayer.[92]

Certain molecules, such as proteins, may rely on the lateral pressure of lipid bilayers for their stability and functioning.[89, 92, 93] Determining the pressure contributions within bilayers is challenging and only a few successful measurements have been reported.[94] Therefore, MD simulations serve as a useful tool for determining the lateral

pressure profile of a lipid bilayer. In NAMD[95], there is a built in algorithm designed to calculate the lateral pressure profile of a bilayer. The pressure is determined using an algorithm initially developed by Lindahl and Edholm[96] with modifications from Sonne et al.[97] that include a method for handling long-range electrostatic interactions (Ewald sums) in systems with PBCs. NAMD first divides the simulation box into slabs normal to the membrane. The pressure is then derived from the virial, which includes contributions from kinetic energy, bonded interactions, nonbonded interactions and Ewald sum. The pressure profile can be determined for constant volume or constant pressure conditions. NAMD's algorithm enables the pressure profile to be subdivided by interaction and atom type, providing insights into how different lipid components and interactions contribute to the overall pressure distribution of the bilayer. This partitioning offers information on how lateral tension varies based on local membrane fluidity, curvature, and even protein interactions.

1.4.4 Leaflet Asymmetry Can Drive Differential Stress

The non-zero leaflet tension in bilayers with either number or compositional asymmetry (or both) has been termed *differential stress*.[69] It is associated with differential changes (expansion and compression) in the packing, as well as overall properties, of the two leaflets as illustrated by the single-component membranes with mismatched numbers of lipids.[98, 99] While both differential stress and any potential curvature stress in the membrane (i.e., arising from differences in the spontaneous curvatures of the two leaflets) may be alleviated if the bilayer adopts a non-zero curvature, the applied periodic boundary conditions can effectively suppress such bending and result in the accumulation of additional compensating differential stress.[69]

While the presence and effects of differential stress can be clearly seen in the compositionally symmetric systems just described, detecting differential stress in compositionally asymmetric bilayers is non-trivial. In that case, depending on the respective leaflet lipid compositions, equal numbers of lipids in the two leaflets can lead to significant differential stress that can be alleviated by introducing a particular number mismatch, resulting in a bilayer with zero leaflet tension.[100-103] This is due to the inherent variability in the structure and properties of different lipid types, as well as to the effects

of interleaflet coupling which may change those properties in ways that are not yet fully understood. Molecules such as cholesterol are also capable of reducing the stress in the bilayer, however, they may not always do so as we discuss below. Importantly, due to the prohibitively slow exchange of phospholipids between leaflets in atomistic simulations with the standard P1 boundary conditions, the lipids retain their leaflet residence for the entirety of the simulation (one notable exception is the use of the $P2_1$ boundary conditions shown in **Figure 1.7** and discussed in Section 1.3.2). While this is precisely what enables the simulation of asymmetric bilayers of defined lipid compositions, it also makes the initial bilayer construction a critical determinant of the presence and related effects of differential stress. In other words, the properties of a simulated asymmetric bilayer depend not only on its composition but also (and to a large extent) on how it is constructed.

1.4.5 Ways to Build Compositionally Asymmetric Bilayers, and How to Choose One

The protocol utilized to construct an asymmetric bilayer in silico significantly affects the resulting bilayer properties and the conclusions that can be drawn from them. This is due to both technical issues (e.g., applied PBCs, limited timescales) and physical-chemical factors inherent to lipid bilayers (e.g., slow spontaneous lipid flip-flop). Different types of methods exist to aid in this task, but which method is most appropriate depends strongly on the scientific intent of the simulations. Each approach has advantages and disadvantages, and each is uniquely suited to address specific types of questions (**Table 1.1**). Notably, the asymmetric bilayers generated with these methods are not expected to be the same since they rely on different assumptions and indirect or direct constraints to ensure asymmetric lipid distribution. However, the advantage of any model membrane study is that parameters can be clearly defined and systematically varied, and performing multiple simulations can, in principle, address the limitations of a given model. For example, if experimental data exists for validation, one can vary the numbers of lipids in one leaflet for the methods that maintain a constant lipid number asymmetry (EqN), match the surface area (or packing densities) of each leaflet (SA), eliminate differential stress (0-DS) or constrain different groups of lipids in the emulate biological

Table 1.1) Summary of the advantages, disadvantages, and suitable applications of the different methods discussed in [91]. This table is reproduced from [91] under the form of CC-BY-4.0.

Method	Pros	Cons	Suitable Applications
EqN	Does not require prior information or simulations	• Does not consider differences in lipid packing preferences • May produce membranes with varying amounts of differential stress	Biophysical properties of asymmetric model membranes prepared from symmetric membranes via 1-to-1 exchange of outer leaflet lipids with new ones
SA	Accounts for relative leaflet packing preferences from symmetric membranes	• Requires prior simulations or information about lipid packing densities • May produce membranes with varying amounts of differential stress	Biophysical properties of asymmetric model membranes in which the relative packing densities of the two leaflets match those from their respective symmetric counterparts
0-DS	Produces membranes with no differential stress	• May require multiple simulations and analysis	Effects of asymmetry on bilayer biophysical properties based on comparisons between asymmetric and symmetric membranes
EmBioAsym	$P2_1$ PBC		
	Allows lipids to sample both leaflets and equilibrate their respective leaflet concentrations	• Requires a simulation with $P2_1$ PBCs currently possible only in CHARMM • Requires constraints on the asymmetry of some lipids	Lipid distribution and biophysical properties of asymmetric membranes with fixed overall lipid composition in which the asymmetric distribution of some lipids is actively maintained (i.e., stays constant)
	Semi-grand canonical ensemble		
	Allows leaflet lipid compositions to change dynamically and equilibrate according to chemical potentials	• Requires a simulation in the semi-grand canonical ensemble currently possible only with coarse-grained models in HOOMD-blue • Requires constraints on the chemical potential difference of some lipids	Leaflet lipid compositions and biophysical properties of asymmetric membranes in which the asymmetric distribution of some lipids is actively maintained (i.e., stays constant) while the overall lipid composition can change due to e.g., the activity of lipid-modifying enzymes or access to extra lipid pools

asymmetry (EmBioAysm) approaches, to find the best match with experimentally determined properties.

Unlike symmetric bilayers, asymmetric bilayers cannot be fully characterized by their lipid composition alone, as differences in leaflet packing and interleaflet coupling significantly influence their physical properties.[69] Instead, two asymmetric bilayers with the same leaflet lipid compositions can have very different properties depending on the amount of differential stress.[101, 102] Therefore, both the leaflet lipid compositions and the relative numbers of lipids in the two leaflets (or equivalently, the resulting differential stress) are needed to fully characterize an asymmetric membrane. Controlling for, or at least reporting, the differential stress of an asymmetric membrane - be it in silico, in vitro, or in vivo - is necessary for placing the results in the right context. Importantly, even though the differential stress in biological membranes is presently unknown, much can still be learned from simulations of asymmetric model membranes if the method for constructing these models is chosen appropriately.

1.4.6 Simulated Lipid Bilayers with Leaflet Lipid Imbalance

Experimental evidence for a lipid imbalance was reported by the Van Deenen group in 1974. However, they attributed the finding to a methodological artifact, reasoning that phospholipase A_2 selectively targets specific phospholipids.[104, 105] In 2025, Doktorova et al. validated that the two leaflets of the plasma membrane exhibit a substantial asymmetry in both phospholipid and cholesterol content.[106] While MD simulations can model lipid number imbalance, experimentally quantifying the exact lipid distribution between leaflets remains challenging due to limitations in current methodologies. To maintain the integrity of the bilayer in simulations, pressure must be applied to the system. By keeping the system under constant pressure, the number of lipids in each bilayer can induce asymmetric lipid packing.[98]

Because both leaflets share the same lateral area, introducing a lipid imbalance forces the leaflet with more lipids—referred to as the overpacked leaflet—to increase its packing density, resulting in a smaller-than-ideal APL.[90, 98] Conversely, the underpacked leaflet, with fewer lipids, exhibits reduced packing density and a larger-than-ideal APL.[90, 98] This imbalance in APL alters the lateral tension in each leaflet and likely leads to

differential stress across the bilayer.[90] If the resulting tension becomes too extreme, the bilayer may destabilize, potentially exposing the hydrophobic tails to the aqueous environment and compromising membrane integrity.[69, 90]

Monolayer tension can influence the bending rigidity of bilayers. Theoretical modeling from the Deserno group has found that number asymmetry significantly affects bilayer rigidity[107] and may explain the experimentally observed stiffening of asymmetric membranes in vitro.[90]

1.4.6 Calculating the Bending Moduli from MD Simulations

Lipid bilayers can behave as thin, quasielastic sheets that can undergo both small and large deformations.[108] The bending modulus of a lipid bilayer quantifies the energy needed to deform the membrane from its intrinsic curvature to an alternative curvature state.[109] The bending modulus is essential in many biological functions including exocytosis and endocytosis, vesicle fusion and regulation of membrane protein activity.[109] Numerous techniques, in both simulations and experiments, are available for measuring the bending modulus. Although bending is widely recognized as an important physical property of biomembranes, there are ongoing controversies in the field. Discrepancies have been observed among different methods used in experiments and simulations.

1.4.6.1 Real Space Fluctuation (RSF) Method for Determining Bending Rigidity

The RSF method was developed by Khelashvili et al. in 2013.[110] In this method, lipid orientation is characterized by a lipid director vector. [108, 110-112]The splay angle between neighboring lipids is calculated throughout the trajectory. [108, 110-112]From the distribution of these splay angles, a potential of mean force (PMF) is computed, and a quadratic fit to the PMF provides the bending rigidity.[108, 110-112] The coefficient of the quadratic fit is the bending rigidity.[108, 110-112]

One advantage of this method is that it is localized, allowing for an examination of the deformation of individual lipids and how the bilayer responds to forces that change the shape of specific regions within the bilayer.[108, 110] This analysis can be performed on asymmetric, small bilayers, typically containing around 100 lipids per leaflet.[108] Additionally, a limitation of this method is its threshold for splay angles, which may

exclude some potentially impactful lipid behaviors.[113] Furthermore, RSF has been shown to overestimate some bending rigidity values in cholesterol rich and asymmetric membranes because the RSF method examines the local fluctuations rather than bilayer behavior pointing towards the use of a different method that accounts for large scale fluctuations.[113]

1.4.6.2 Transverse Curvature Bias (TCB) Method

The TCB method utilizes the correlation between the lipid director and the surface curvature to quantify the curvature sampled by a lipid along the bilayer normal. The slope of the best-fit line of the curvature sampling and depth along the bilayer normal yields the bending rigidity.[114]

One advantage of this method is how it accounts for a lipid's local curvature preferences relating to how it ultimately will orient itself in the bilayer based on the bilayer's total curvature.[114] However, this method requires much larger simulations (~400 lipid minimum). Despite the increase in bilayer size, the computational cost is much lower than the RSF method.[114, 115]

1.5 Model Membranes for Studying Phase Separation in the PM

1.5.1 Simplified Models of the PM

Identifying and isolating specific lipid-lipid interactions in the PM is challenging due to its complexity, which includes proteins, receptors, and various structural elements such as the glycocalyx and cytoskeleton. To advance the field of lipid biophysics, researchers have developed alternative techniques to create simplified models of the PM known as model membranes. These model membranes replicate biological membranes and they are usually used to explore the influence of individual lipids and lipid interactions on biomembrane physics and properties.

Model membranes often mimicking the outer leaflet of the PM usually consist of three components and have exhibited phase separation, like the hypothesized lipid rafts of the PM.[29, 52, 55] These ternary mixtures typically include a high-melting lipid (high-T_M), a low-melting lipid (low-T_M) and cholesterol (Chol). High-T_M lipids are typically saturated and can pack tightly, while low-T_M lipids are lipids that have kinks or branches that prevent tight packing. Studies on the phase behavior of these ternary mixtures typically

examine various ratios of high-T_M/low-T_M lipids and cholesterol at different temperatures to construct ternary phase diagrams.[8, 32, 34, 52, 55, 116] These ternary phase diagrams can provide valuable insights on how temperature and/or lipid composition can influence membrane structure and miscibility. By utilizing model membranes, a physical chemistry approach has been adopted to clarify specific molecular interactions, offering an understanding of lipid-lipid interactions and domain formation in the PM.

1.5.2 Types of Model Membranes

The choice of technique and the specific experimental questions being addressed should dictate the selection of the most suitable model membrane (**Table 1.2**). There are several commonly used model membranes, including supported lipid bilayers (SLBs), giant unilamellar vesicles (GUVs), multilamellar vesicles (MLVs), low lamellarity vesicles (LLVs), large unilamellar vesicles (LUVs), and small unilamellar vesicles (SUVs). These model membranes have been employed in various studies, particularly those examining phase separation.[117]

This drives the question: Does the size of the vesicle affect the phase behavior of the system? Typically, SUVs that are approximately 50 nm or larger—the minimum size typically used in phase studies—exhibit phase behaviors that are similar to those of their larger counterparts, such as GUVs.[29] This similarity arises because the curvature-induced bending stress in SUVs is relatively minor when compared to that in GUVs.[29] As a result, the ideal molecular shape of the lipids remains largely undistorted, which means that the intrinsic lipid interactions necessary for driving phase separation remain unchanged.[29, 118]

1.5.3 Domain Structure and Formation in Model Membranes

As mentioned in Section 1.5.1, model membranes to study phase separation often consist of high-T_M lipids, low-T_M lipids, and cholesterol. Raft formation is driven by the favorable and unfavorable interactions of lipids in the PM, usually saturated and unsaturated lipids. Thickness differences created by phase separation drive a phenomenon known as hydrophobic mismatch, which incurs a significant energetic cost referred to as line tension.[136] The greater the hydrophobic mismatch between phases, the higher the line tension. High line tension typically promotes the formation of larger domains to minimize domain perimeter, while low line tension facilitates smaller

Table 1.2) Model membrane sizes with applications and methods from literature.

Vesicle	Size	Protocols and Applications (Reference Number)
SUVs	<100 nm	[119-122]
LUVs	100-1000 nm	[40, 119, 123-126]
MLVs	> 500 nm	[29, 127-129]
GUVs	5 – 50 μm	[117, 130-135]

domains.[137] Dipole potential refers to the electrical potential difference that develops across the lipid headgroup region of a bilayer, caused by the alignment of dipoles in lipid molecules and interfacial water molecules.[138] However, dipole potential acts against line tension and encourages the formation of smaller domains.[137]

Despite fluid-fluid phase separation being observed in lipid-only model membranes[8, 31, 34, 35, 52-55], the biological relevance of these domains remains controversial.[2, 27, 55, 139] Most low-T_M lipids are hybridized, featuring one saturated acyl chain and one unsaturated acyl chain.[2] It has been demonstrated that some three component mixtures with a hybridized low-T_M lipid do not macroscopically phase separate; instead, they exhibit nanoscopic phase separation.[29, 53] When macroscopic phase separation occurs, the mixture is classified as a type-II mixture. Conversely, if there is no macroscopic phase separation and only nanoscopic separation is observed, the system is classified as type-I.[55, 116] This nanoscopic domain formation is thought to represent lipid rafts in living cells[140] and therefore has garnered interest, particularly with the development of techniques that go beyond the resolution limit of traditional optical microscopy. These include Förster resonance energy transfer (FRET)[29, 128, 141, 142], small angle neutron scattering (SANS)[143, 144], and cryogenic electron microscopy (cryo-EM)[8, 37, 40], which have been implemented to identify and even visualize nanoscopic heterogeneity in model membranes.

1.6 Techniques for Examining Phase Behavior in Model Membranes

1.6.1 Confocal Fluorescence Microscopy (CFM)

Fluorescence microscopy is a highly effective tool for examining biological systems at the cellular level. In studies of model membranes, particularly regarding phase behavior, phase-preferring probes can be utilized to investigate these characteristics. These probes are excited at specific wavelengths and emit photons at longer wavelengths, enabling a diverse range of applications in both membranes and proteins, including the use of multiple probes in a single sample.[8, 25, 31, 145, 146]

Confocal fluorescence microscopy (CFM) is a widely used technique for visualizing phase separation and domain formation in model membranes such as GUVs. The relatively large size of GUVs—often exceeding that of typical cells—makes them

particularly well-suited for spatially resolving lateral heterogeneity within the bilayer with high optical contrast and molecular specificity. This technique utilizes lipophilic dyes that exhibit phase preferences based on their structure. Pinhole CFM has the unique capability to excite and collect light at different wavelengths, allowing for the simultaneous visualization of both Ld and Lo domains when using probes with varying excitation and emission wavelengths. CFM captures images from a single focal plane by using a pinhole to reject out-of-focus light, resulting in improved optical sectioning. It offers fast imaging and z-plane sectioning, making it highly applicable for imaging model membranes due to its high resolution and contrast. However, it is important to note that confocal fluorescence microscopy is limited by the diffraction of light, restricting its spatial resolution to approximately 200 nanometers. The resolution limit, however, is dependent on the wavelength of the excitation laser and the numerical aperture of the objective lens. To study lateral heterogeneity at smaller length scales, other methods such as FRET and cryo-EM are necessary.

1.6.2 FRET

FRET is a photophysical process that utilizes a donor fluorophore and an acceptor fluorophore.[142] In this case, the donor fluorophore is excited and transfers its energy non-radiatively to an acceptor fluorophore.[147] The probability of energy transfer depends on the distance between the donor emission dipole and acceptor excitation dipole. Due to this distance dependence, FRET is highly sensitive to molecular length scales. The range at which FRET is effective depends on the specific FRET pairs used.[142]

This methodology has numerous applications in biological systems, including the study of membrane phase behavior.[142] Because FRET is sensitive to distance and can measure at the nanoscopic length scale, it enables the detection of nanodomains, as the probes can detect changes in lipid distribution within membranes.[29, 128] These FRET measurements for membranes are cuvette-based and are amenable to both unilamellar and multilamellar vesicles of various size and polydispersity, including LLVs prepared by rapid solvent exchange (RSE).[127, 141]

A typical FRET experiment to probe membrane phase behavior uses two probe pairs with complementary partitioning behavior: one pair consists of probes that prefer

the same phase, while the other pair prefers different phases.[148] At a phase transition, the pair that shares the same phase preference shows an increase in FRET efficiency, whereas the pair with opposing preferences demonstrates a decrease in FRET efficiency (**Figure 1.8**).[141] Due to the high resolution of FRET, this technique can detect domains as small as the Förster distance, which is ~5 nanometers.[142] The Förster distance is specific to each donor–acceptor fluorophore pair and is defined as the distance at which 50% of the excitation energy is transferred from the donor to the acceptor.[147]

1.6.3 Cryo-EM

Cryo-EM has become a valuable tool in science with angstrom-level resolution. Cryo-EM has played a fundamental role in determining the structures of multiple biomacromolecules, including proteins and membranes. Cryo-EM was first used to study membranes in the 1980s.[149] In cryo-EM an electron beam passes through the vitrified sample, and the transmitted or scattered electrons are captured by a detector to generate high-resolution images of the sample's native structure.[150] One of the most advantageous features of cryo-EM is that it is a probe-free technique relying on differences in the intrinsic electron density of biomolecules rather than external probes.[8] This characteristic, along with its high spatial resolution, allows for direct imaging of nanodomains in LUVs.[40] The identification of these nanodomains has been achieved by measuring the local thickness of the bilayer.[40] Membranes appear as two dark parallel lines in the images because of the contrast between the electron-rich headgroups and electron-poor hydrocarbon chains. Although the precise distance between the two lines depends on instrument settings like defocus length, it is proportional to the bilayer thickness. [40]Since the Lo phase is typically 5-10 Å thicker than the Ld phase, this information can be used to determine the presence of domains in Cryo-EM images.[40]

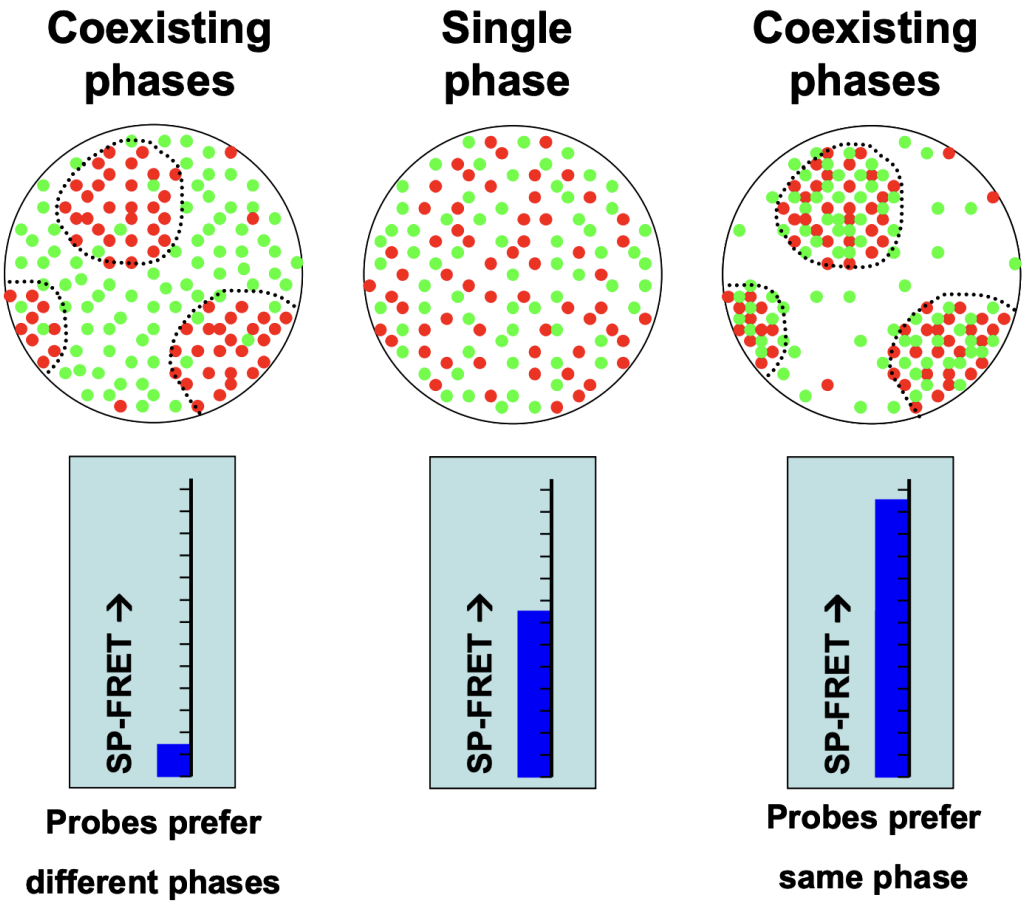


Figure 1.8) Dual probe method for SP-FRET in lipid membranes. Starting with a uniformly mixed (b), if the two probes prefer different phases they separate and FRET signal intensity decreases (a). If the two probes prefer the same phase, decreasing the temperature increases FRET signal intensity. This figure is from [140] and reused with permission from the American Physical Society

CHAPTER 2

QUANTIFYING ACYL CHAIN INTERDIGITATION IN SIMULATED BILAYERS VIA DIRECT TRANSBILAYER INTERACTIONS

A version of this chapter was originally published as listed below and is reproduced with under the therms CC-BY 4.0 .

Emily H. Chaisson, Frederick A. Heberle, Milka Doktorova. "Quantifying Acyl Chain Interdigitaiton in simulated bilayers via direct transbilayer interactions" *JCIM* 2025; *65* (8), 3879-3885

This chapter describes algorithms designed by E.H.C., F.A. H., and M.D. Data analysis was performed by E.H.C and F.A.H. The manuscript was prepared by myself, F.A. H., and M.D.

2.1 Abstract

In a lipid bilayer, the interactions between lipid hydrocarbon chains from opposing leaflets can influence membrane properties. These interactions include the phenomenon of interdigitation, in which an acyl chain of one leaflet extends past the bilayer midplane and into the opposing leaflet. While static interdigitation is well understood in gel-phase bilayers from X-ray diffraction measurements, much less is known about dynamic interdigitation in fluid phases. In this regard, atomistic molecular dynamics simulations can provide mechanistic information on interleaflet interactions that can be used to generate experimentally testable hypotheses. To address limitations of existing computational methodologies, which provide results that are either indirect or averaged over time and space, here we introduce three novel ways of quantifying the extent of chain interdigitation. Our protocols include the analysis of instantaneous interactions at the level of individual carbon atoms, thus providing temporal and spatial resolution for a more nuanced picture of dynamic interdigitation. We compare the methods on bilayers composed of lipids with equal total number of carbon atoms but different mismatches between the sn-1 and sn-2 chain lengths. We find that these metrics, which use freely available software packages and are easy to implement, provide complementary details that help characterize various features of lipid-lipid contacts at the bilayer midplane. The new frameworks thus allow for a deeper look at fundamental molecular mechanisms underlying bilayer structure and dynamics and present a valuable expansion of the membrane biophysics toolkit.

2.2 Introduction

Biological membranes are chemically complex, consisting of a lipid bilayer with hundreds of chemically distinct lipids and various types of proteins that interact with them. The structure and physical behavior of the bilayer are determined in part by the structure and thermodynamic properties of its constituent lipids. As one example, lipids with two chains of varying lengths (i.e. asymmetric chain lipids), have been hypothesized to affect the fluidity of the membrane in both prokaryotic and eukaryotic cells[2, 4-6, 151-153]. Asymmetry in the effective chain lengths of the lipids can arise both from unequal numbers of carbons as well as from the tilt of the glycerol backbone, which naturally

allows the *sn*-1 chain to reach deeper into the hydrophobic core of the bilayer than the *sn*-2 chain. Thus, the resulting length mismatch within a lipid molecule can range from negligible (for some lipids with chains differing by 0 or 2 carbons[154]) to extreme, as in the case of some sphingomyelin species[155].

A large mismatch in effective chain length increases the probability of interdigitation, a phenomenon where an acyl chain in one leaflet penetrates past the bilayer midplane into the opposing leaflet. In principle, enhanced interactions between the two leaflets in an interdigitated state could effectively 'zip' the leaflets together and thereby affect interleaflet friction. These interactions may also impact the overall flexibility of the bilayer and its mechanical properties although further studies and robust interdigitation metrics are needed to elucidate the exact relationship. Being an internal property of the lipid bilayer, interdigitation likely incurs an energy cost similar to those of lipid tilt and splay[156-159] but the detailed form of the energy functional has yet to be determined.

Interdigitation in vitro has been studied with techniques such as X-ray and neutron diffraction[156, 158-160], differential scanning calorimetry[156, 158], vibrational spectroscopy[156, 158], nuclear magnetic resonance, electron microscopy and electron spin resonance[158], scattering techniques[4, 158, 159, 161, 162], and fluorescence[4, 158, 159, 161, 162]. Rather than directly quantifying interdigitation, these methods reveal its effects on membrane properties such as thickness, order, lateral lipid diffusion, and transition temperature. Though such indirect information is useful, many of these techniques suffer from poor spatial and/or temporal resolution, and may require extrinsic probes that can locally perturb the bilayer environment, potentially interfering with the measurement.[163]

Molecular dynamics (MD) simulations offer a complementary approach for characterizing membrane structure and dynamics by tracking the positions of individual lipid atoms over time. Interdigitation in simulated bilayers has previously been quantified in two ways: (1) by calculating the overlap of mass density distributions for atoms in opposing leaflets or specific atom groups, such as the terminal methyl and its hydrogens[87, 159, 164-167]; (2) by measuring the distance along the bilayer normal between terminal methyl carbons of lipids in opposing leaflets[39, 168], or (3) by measuring changes

in the position of individual atoms along the bilayer normal.[156] For the latter, the underlying assumption is that transverse movement of these atoms brings the entire chain closer to, or further away from, the bilayer midplane and thus correlates with the extent of interdigitation. While these measurements constitute a reasonable starting point for interrogating interleaflet interactions, to our knowledge a detailed examination of pairwise contacts between lipid atoms from opposing leaflets has not yet been demonstrated.

Here, we develop three alternative ways of analyzing interdigitation in MD simulations to complement and expand on previous methods. Each new metric provides unique insight into different aspects of acyl chain interdigitation, such as specific trans-leaflet carbon–carbon interactions and the shape and evolution of the leaflet–leaflet interaction region. The three methods are: (1) **nISA** (normalized Interfacial Surface Area), which utilizes 3D Voronoi tessellations to define and quantify the interleaflet contact surface; (2) **ccMat** (carbon contact Matrix), which fills a matrix with counts of the average number of direct interactions between carbon atom pairs in opposing leaflets; and (3) **doMat** (density overlap Matrix), which computes the overlap area of number density distributions for pairs of carbons in opposing leaflets. We benchmark these tools using two symmetric bilayers, 1,2-dipalmitoyl-sn-glycero-3-phosphocholine (16:0-16:0 PC, DPPC) and 1-myristoyl-2-stearoyl-sn-glycero-3-phosphocholine (14:0-18:0 PC, MSPC), that are expected to differ substantially in the extent of chain interdigitation.[153]

2.3 Methods

2.3.1 Simulation details.

When we started this work, 14:0-18:0 PC (MSPC) was not available in the CHARMM-GUI web server.[82] To build this lipid, we first used CHARMM-GUI to construct a bilayer of 18:0-18:0-PC with 100 lipids per leaflet (200 lipids total) and hydrated with 45 waters per lipid without any salt ions. Following the protocol described in ref.[87], 14:0-18:0 PC was then built by removing the terminal methyl and two adjoining methylene segments of the *sn*-1 chain (C316-C318 in CHARMM notation) as well as the two hydrogens on C315. A new terminal methyl, C314, was then created by converting C315 to hydrogen (H14Z) by changing its atom name, type, and partial charge. The two

hydrogens on the C314 atom were also changed to match the atom name, type, and partial charge to reflect the characteristics of hydrogens in a terminal methyl group.

All simulations were run using the NAMD software[169] and the CHARMM36 force field [86, 170] for lipids. The MSPC bilayer was energy minimized for 1200 steps, then simulated for a total of 1 ns with an integration time-step of 1 fs before the production run, which used a 2 fs time-step. The DPPC bilayer was equilibrated using the CHARMM-GUI 6-step equilibration protocol. Simulations were run at a constant temperature of 50°C (323.15 K) and a constant pressure of 1 atm using NAMD's Langevin thermostat and Nose-Hoover barostat, respectively. Long-range interactions were modeled with a 10-12 Å Lennard-Jones potential using NAMD's *vdwForceSwitching* option. Hydrogen bonds were constrained with the *rigidbonds* parameter set to "all." The Particle Mesh Ewald (PME) method was used and grid spacing was set to 1 Å to model the electrostatic interactions. An autocorrelation function from ref. [171]was used to evaluate the equilibration of bilayer area; after convergence, each system was simulated for an additional ~ 1 μs. The length of the analyzed trajectory was 0.991 μs for MSPC and 1.02 μs for DPPC. We also ran an additional NP γT simulation starting from the end of the DPPC trajectory and applying a tension of $\gamma = -5$ mN/m in the *xy* plane which effectively compressed the bilayer area.[172] (**Appendix 2.1**) This simulation was run for a total of 0.4 μs with the last 0.36 μs used for analysis. Prior to analysis, the systems were centered in Visual Molecular Dynamics (VMD)[173] by moving the center of mass of the lipid terminal methyl groups to $z = 0$. The top leaflet was then defined as the leaflet in which the headgroup phosphorus atom had an average $z > 0$.

2.3.2 3D Voronoi tessellation

Voronoi tessellations (VT) of simulated bilayers have previously been used to estimate areas and volumes of individual lipids.[174, 175] Here, we used the atomic coordinates of lipid and water atoms as generators (i.e., the points used to construct Voronoi cells) to perform a 3D VT in each simulation frame using the software *voro++*.[176] The Voronoi cells generated by the tessellation - each composed of a set of vertices, edges, and faces -represent the physical space occupied by individual atoms and

enable various calculations as described below. We used a custom *Python* script to reformat the *voro++* output for subsequent analyses in MATLAB [12].

2.3.3 Normalized Interfacial Surface Area (nISA)

The midplane *interfacial surface area* is expected to directly correlate with the extent of interdigitation, as shown in **Figure 2.1**. When this quantity is normalized by the bilayer area projected onto the *xy* plane, the resulting dimensionless quantity - which we term *nISA* - represents the fractional increase in the interfacial surface area due to interdigitation. We calculated the interfacial surface area between top and bottom leaflet lipids for each frame as follows. All pairs of neighboring atoms (defined as those whose Voronoi cells share a face) in which the two atoms also belonged to different leaflets were identified, and the areas of their shared faces summed to give the total interfacial surface area. This area was then divided by the cross-sectional area of the box in the frame to yield $nISA$, i.e.,

$$nISA = \frac{\sum a_{ij}}{A_{xy}} \tag{2.1}$$

In Eq. 2.1, a_{ij} is the area of the face f_{ij} common to the Voronoi cells for atom i in the top leaflet and atom j in the bottom leaflet, and A_{xy} is the lateral area of the simulation box. The interleaflet contact surface can be visualized in 3D by plotting a mesh grid of the vertex coordinates of the common faces (**Figure 2.2a**), or in 2D by projecting thecoordinates onto the *xy* plane and using grayscale to represent the height in the z-dimension (**Figure 2.2b**).

2.3.4 Carbon Contact Matrix (ccMat).

In addition to the interfacial surface area, interdigitation in a bilayer can also be quantified by the number of direct interactions between acyl chain carbons of lipids in opposing leaflets. We counted these interactions by using a cutoff distance of 4 Å to define atomic contact[177]. A matrix was constructed in which each row and column represent distinct chain carbons of the top and bottom leaflet lipids, respectively, and each matrix element represents the time averaged number of contacts between these

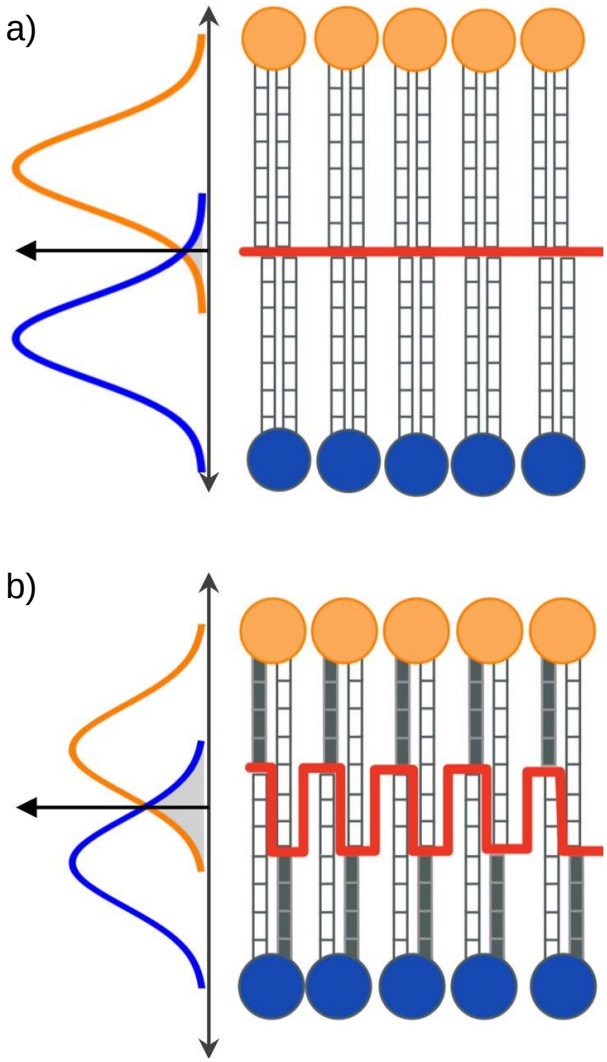


Figure 2.1) Figure 1. Schematic illustration of interdigitation quantified by the normalized interfacial surface area (nISA) and the Interdigitation tool in MEMBPLUGIN (memIT, see Appendix A2.1). (a) nISA is calculated as the midplane surface area (in red) divided by the lateral bilayer area. In the absence of interdigitation, the interfacial surface area per lipid is equal to the average area per lipid and nISA = 1. memIT, quantified by the overlap of the total mass density profiles of the top (orange) and bottom (blue) leaflets, is also shown as a gray shaded area. (b) Increased interdigitation in a mixed-chain bilayer results in a greater mass density overlap and a more dimpled midplane surface, leading to an increase in both memIT (larger mass density overlap) and nISA (larger interfacial surface).

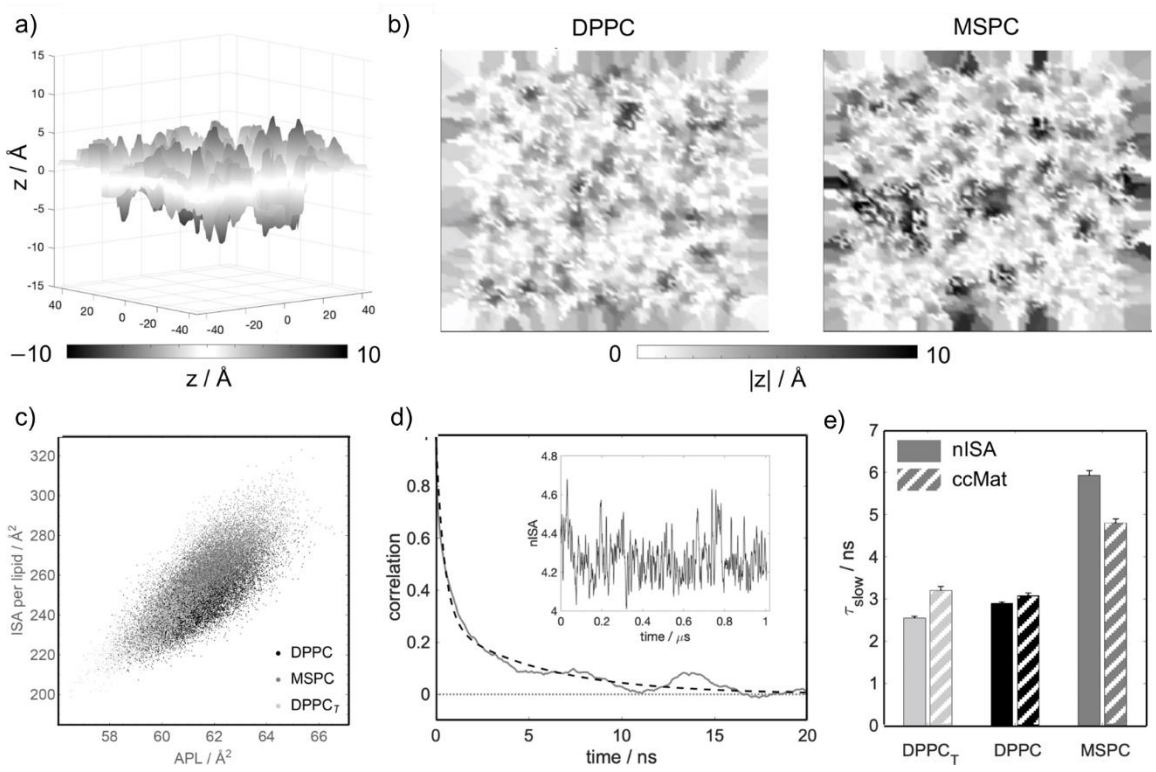


Figure 2.2) Interdigitation quantified with nISA. (a) 3D visualization of the interleaflet contact surface of DPPC from a representative trajectory frame. The surface is defined as the set of Voronoi cell faces shared by neighboring interleaflet atom pairs as described in Methods**. (b) Contact surfaces shown as 2D intensity maps of |*z*| where darker shades correspond to greater interdigitation of acyl chains for DPPC and MSPC. (c) Interfacial surface area per lipid is correlated with the average area per lipid across all bilayers (correlation of 0.75). (d) Time autocorrelation function of nISA calculated for MSPC (solid line) and its best fit to a double exponential function (dashed line). Inset shows the raw data as a function of time. (e) Slow correlation times for nISA and ccMat for the three bilayers. Data and fits are shown in Appendix 2.1 and Appendix 2.3**

carbon atoms. The data is visualized as a heatmap in which the color intensity of the pixel represents the average number of opposing leaflet carbon pair interactions.

2.3.5 Density Overlap Matrix (doMat)

Interactions between lipid carbon atoms from opposing leaflets can also be quantified from the overlap of the carbons' number density profiles (NDPs). We used VMD's Density Profile tool to calculate the NDP for each carbon of the top and bottom leaflet lipid chains. The overlap area, Ω_{ij}, was then calculated as:

$$\Omega_{ij} = \int min\left[\rho_{i,top}(z), \rho_{j,bot}(z)\right]dz. \quad (2.2)$$

In Eq. 2.2, $\rho_{i,top}(z)$ is the NDP for carbon i in the top leaflet, $\rho_{j,bot}(z)$ is the NDP for carbon j in the bottom leaflet, and the integral is computed over all z (in practice, the lower and upper bounds of the simulation box in the z-dimension). A matrix similar to that calculated for the ccMat method was then constructed, with each entry corresponding to the overlap for one carbon pair. The sum of intensities in the four quadrants and the whole matrix provide alternative metrics for the extent of interdigitation.

Additional methodological details are described in **Appendix 2.4.**

2.4 Results and Discussion

To investigate interdigitation, we simulated two bilayers made of lipids with either matching (DPPC) or mismatched (MSPC) chain lengths and shown recently in scattering experiments to have substantially different extents of interdigitation.[87] As an additional control, we simulated DPPC under a constant negative surface tension ($DPPC_T$), which compresses the bilayer area (**Appendix 2.1)** and should decrease interdigitation. We first used the standard method for quantifying interdigitation by calculating the overlap of the mass densities of all atoms in the two leaflets (memIT, see **Appendix 2.4** and **Table 2.1**). This calculation confirmed that MSPC chains have the highest degree of interdigitation, followed by DPPC and $DPPC_T$, as expected (**Appendix 2.5**). The trend is consistent with results obtained from analysis of small-angle scattering data, which showed a 28% increase in the overlap of terminal methyl carbons for MSPC compared to DPPC.[87]

Next, we used 3D Voronoi tessellation to examine the interface that separates the two leaflets. A representative snapshot of the interfacial surface reveals that MSPC lipid

chains penetrate deeper into the opposing leaflet compared to the chains of DPPC (**Figure 2.2a, b**). We also calculated a dimensionless normalized interfacial surface area, nISA, from the 3D Voronoi analysis (Eq. 2.1, **Table 2.1**). In the DPPC bilayer, nISA was 4.03 ± 0.010, indicating that the interfacial surface area per lipid is four times larger than the average area per lipid projected onto the *xy* plane, consistent with the three-dimensional nature of the true interleaflet contact surface compared to idealized interactions at a flat bilayer midplane. In the MSPC bilayer, nISA was 4.26 ± 0.010, indicating a greater extent of interdigitation compared to DPPC in agreement with the trend seen in memIT values (**Table 2.1, Appendix 2.5**). Similarly, the compressed $DPPC_T$ bilayer had the smallest nISA of 3.94 ± 0.011, as expected. The data also allows for extraction of the specific contributions of the *sn*-1 and *sn*-2 chains to the nISA surface, revealing their relative abundance in cross-leaflet interactions (**Appendix 2.6**). Furthermore, the high temporal resolution of the simulations enables an examination of interdigitation dynamics. For example, we find that the interfacial surface area is dynamically correlated with the projected box area (**Figure 2.2c**), confirming that increased interdigitation leads to a decrease in thickness and increase in bilayer area (with area and thickness being strongly correlated across all bilayers, **Appendix 2.7**) Analysis of the nISA time autocorrelation function (**Figure 2.2d**) reveals the presence of slow- and fast-decaying processes that are 2 to 4 times longer for MSPC compared to DPPC and $DPPC_T$, indicating longer-lived interleaflet contacts for the more interdigitated MSPC membrane (**Appendix 2.2**, **Figure 2e**, and **Appendix 2.3**)

Applying a conceptually different approach, we then compared the number of pairwise contacts between acyl chain carbon atoms of lipids in opposing leaflets by calculating a carbon-contact matrix, ccMat (**Figure 2.3**). The MSPC bilayer had on average ∼27% more cross-leaflet carbon–carbon contacts per frame than DPPC and ∼33% more contacts than $DPPC_T$ (**Table 2.1**, **Appendix 2.5**). For DPPC, interleaflet contacts were greatest for the terminal methyl carbons and decreased systematically with increasing distance from the terminal methyls, with only minor differences in *sn*-1/*sn*-1, *sn*-2/*sn*-2, and *sn*-1/*sn*-2 interactions. The asymmetry in the MSPC matrix is consistent with the longer chain extending deeper into the opposing leaflet and engaging in a greater

Table 2.1) Interdigitation Quantified by Various Methods[1] reused from[4] by the terms of CC-BY-4.0.

system	memIT (dimensionless)	nISA (dimensionless)	ccMat (contacts/frame)	doMat ($Å^{-2}$)
DPPC	0.282 ± 0.0013	4.03 ± 0.010	270 ± 1.1	0.750 ± 0.009
MSPC	0.324 ± 0.0014	4.26 ± 0.010	342 ± 1.5	0.88 ± 0.011
$DPPC_T$	0.270 ± 0.0019	3.94 ± 0.011	257 ± 1.5	0.69 ± 0.024

[1]memIT was calculated using all leaflet atoms; nISA is the fractional increase of the lateral bilayer area at the interfacial surface; ccMat corresponds to the average number of total trans-leaflet carbon–carbon contacts per frame; and doMat is the sum of the overlap number density integrals of all trans-leaflet carbon–carbon pairs (see Section 2.3 and **Appendix 2.4**). Errors were calculated with block averaging, as detailed in **Appendix 2.4.**

total number of contacts with the longer chain of the lipids therein chains (i.e., *sn*-1/*sn*-2), followed by the terminal methyl carbons of the longer chain (*sn*-2/*sn*-2). The asymmetry in the MSPC matrix is consistent with the longer chain extending deeper into the opposing leaflet and engaging in a greater total number of contacts with the longer chain of the lipids therein (**Figure 2.3a**, bottom right quadrant), as also observed in the nISA analysis of specific chain interactions (**Appendix 2.6**). Comparison of the interdigitation dynamics quantified with ccMat across all bilayers shows the same trend as that of nISA (**Appendix 2.2**, **Figure 2.2e**, **Appendix 3.3d-f**)

The ccMat analysis uses an arbitrary cutoff distance for interatomic contacts. To circumvent this requirement, we also quantified interdigitation from the overlap of the number density profiles of individual cross-leaflet carbon pairs, an approach that we termed doMat. **Figure 2.3b** shows doMat for MSPC and DPPC, again revealing a relatively symmetric matrix for DPPC and an asymmetric matrix for MSPC, consistent with the differences in chain mismatch for these lipids. Qualitatively, doMat features are similar to ccMat, with the overlap of cross-leaflet carbon atoms systematically decreasing with distance from the tail ends (**Figure 2.3b**). While *sn*-1/*sn*-2 interactions are similar in the two bilayers, DPPC has a more than 3-fold larger overlap of *sn*-1/*sn*-1 number densities compared to MSPC (and more than 4-fold increase in close contacts from the ccMat analysis, **Figure 2.3a**), indicating that cross-leaflet interactions between two shorter chains in the sn-1 positions are infrequent for chain-asymmetric lipids. Furthermore, consistent with ccMat, doMat for MSPC shows extensive overlap between carbons in the *sn*-2 chains of opposing leaflet lipids (**Figure 2.3b**, lower right quadrant). Interestingly, the *sn*-2/*sn*-2 terminal carbon interactions are more pronounced than the *sn*-1/*sn*-2 interactions in doMat, in contrast to the trend in ccMat. This can be explained by the larger conformational space sampled by the longer stearoyl chains, which results in atomic number densities extending further into the opposing leaflet and a concomitant increase in interleaflet carbon overlap. The sum of the doMat matrix elements showed 17% and 27% more carbon–carbon overlap in the MSPC bilayer compared to DPPC and $DPPC_T$, respectively (**Table 2.1**, **Appendix 2.5 and Appendix 2.8b**).

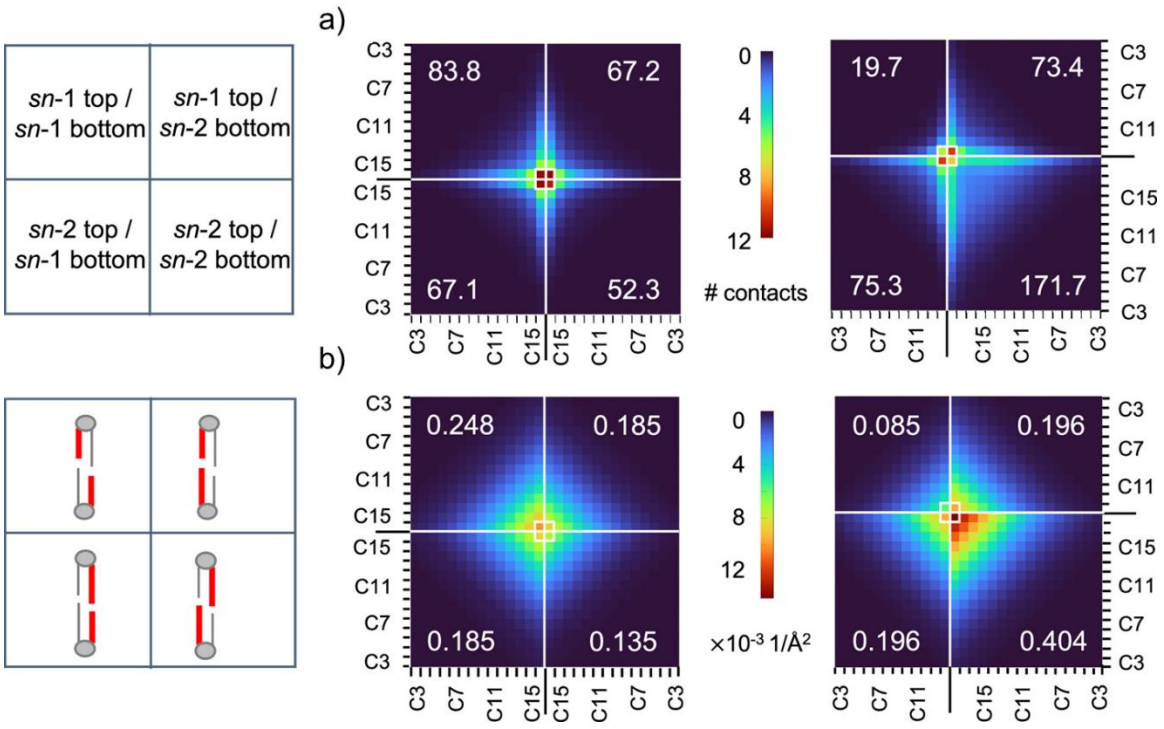


Figure 2.3) Matrix-form quantification of lipid interdigitation in DPPC (left) and MSPC (right) bilayers. Quadrants correspond to interactions between carbon atoms in the *sn*-1 and *sn*-2 chains of opposing leaflets as indicated in the cartoons on the left. (a) Carbon contact matrices (ccMat) where each matrix element represents the time-averaged number of close contacts for the specific interleaflet carbon pair. (b) Atomic density overlap matrices (doMat) where each matrix element represents the overlap of time-averaged atomic number density profiles for the interleaflet carbon pair calculated from Eq 2.2. The mean quadrant sums are indicated in the corresponding four corners of each matrix and their errors are listed in Appendix 2.1.

The code for the three methods, as well as detailed instructions and examples, have been deposited on Zenodo (doi.org/10.5281/zenodo.14605924) and should be straightforward to implement. The provided implementation uses a structure PSF file and a simulation trajectory in DCD format and is based on mostly freely available software packages (the only exception is the analysis in MATLAB which can be easily ported to, e.g., python). **Appendix 2.9** lists the required software and libraries. Of the three methods, nISA takes the longest to compute (~1 min/frame for bilayers with 200 lipids); however, the trajectory can be analyzed in multiple blocks in parallel for more efficient performance.

2.5 Conclusion

The modes of interleaflet interaction in a lipid bilayer are tightly coupled to properties such as membrane thickness and local leaflet elasticity[178, 179]. Here, we present three methods for quantitatively characterizing the physical contact between the leaflets as manifested by the degree of lipid interdigitation. While some of them, as for instance the number of cross-leaflet contacts and overlap of number densities, can be calculated with existing tools for specific atom selections (as in memIT), analysis of the trends along the entire lipid chains (as in ccMat and doMat) provides additional details and allows for a more comprehensive representation of lipid interdigitation. Furthermore, quantification of the entire spatially resolved midplane surface and its time evolution enables in-depth analysis of the dynamics of all direct leaflet–leaflet interactions, something that existing methods do not provide.

While the three methods can in principle be applied to bilayers of varying sizes, it is important to consider their limitations. One advantage of ccMat is that it is based on local analysis of interleaflet carbon contacts and therefore should not be affected by membrane undulations that are often observed in larger bilayers. In contrast, doMat relies on number densities calculated in flat slabs along the bilayer normal making the results sensitive to membrane curvature. As currently implemented, nISA will also be affected by undulations since the quantity is normalized by the instantaneous (projected) bilayer area (Eq 2.1). Normalizing the interfacial surface area by the number of lipids instead can help alleviate this problem.

The computational results obtained from these methods can be validated by ensuring consistency with experimental measurements when available; for example, lipid volumes calculated from the 3D Voronoi tessellation protocol can be compared to those obtained from densitometry measurements[180, 181]. Reliable simulation findings can be used to investigate the energetics of leaflet–leaflet interactions and their contribution to bilayer mechanics, examine the relationship between interdigitation and other local lipid dynamics like lipid protrusion, and generate testable hypotheses for the mechanisms of interleaflet coupling. The methods and results can thus provide valuable insights for general structure - property relations in lipid bilayers.

CHAPTER THREE
STRUCTURAL CONSEQUENCES OF CHAIN-LENGTH MISMATCH IN SIMULATED PC LIPID BILAYERS

A version of this chapter is in preparation to be submitted. Some of this data is represented in Chapter 2 and is reused under the terms of the Creative Commons Attribution CC BY 4.0 license.

This chapter describes research designed by **Emily H. Chaisson**, Milka Doktorova, and Frederick A. Heberle. The simulations and data analysis was performed by E.H.C.. The manuscript was written and edited by F.A.H., M.D., and E.H.C..

3.1 Abstract

Phospholipid structure drives distinct bilayer properties and interleaflet coupling. A central challenge in membrane biophysics is deconvoluting contributions of specific lipid species given the complexity of the native lipidomes. To address this, simplified model membranes are often used to elucidate fundamental biophysical mechanisms. One interesting subclass of lipids shown to have biological significance is mixed chain lipids, where the two saturated acyl chains differ in the number of carbons. Recent neutron spin echo experiments revealed that bilayers composed of mixed-chain lipids with the greatest disparity in acyl chain length exhibit the lowest bending moduli, despite a presumed increase in interdigitation and interleaflet friction.[1] However, direct quantification of interdigitation or interleaflet coupling in these systems is lacking. In this study, we used all-atom molecular dynamics simulations to investigate lipid bilayers composed of asymmetric lipids with a total of 32 acyl chain carbons, using symmetric DPPC as a reference. By systematically increasing the *sn*-1 chain length while decreasing the *sn*-2 chain length, we examined how acyl chain asymmetry modulates interleaflet coupling and lipid and bilayer properties including acyl chain conformational flexibility (i.e., backbending), area compressibility and bending rigidity. Our simulations reveal that lipids with greater chain length asymmetry exhibit enhanced interdigitation, yet interleaflet mechanical coupling remained unchanged. This apparent contradiction arises from the increased propensity of these asymmetric lipids to adopt backbent conformations, which effectively decouple interleaflet motions despite deeper and more frequent chain penetration into the opposing leaflet. These findings establish a mechanistic basis for how chain asymmetry alters mechanical interleaflet coupling and provide a quantitative framework for interpreting the biophysical behavior of mixed-chain lipids in both synthetic and biological membranes.

3.2 Introduction

Lipid bilayers are ubiquitous in biology and are functionally important for a variety of biological phenomena.[7, 23] Over time, these membranes have also adapted to be more efficient in helping to maintain homeostasis.[153, 182] One predicted way this is achieved in nature is by having hundreds of structurally distinct lipids.[2] These structurally distinct

lipids can differ in headgroups, backbone, acyl tail length, and unsaturation.[2, 58] These slight structural changes in lipids have been shown to drive differences in membrane properties such as thickness, compressibility, and bending.[183-186] For example, increasing the chain length in a saturated lipid increases the bilayer thickness, and this change in thickness can significantly increase the energy needed to bend the membrane.[186]

An underexplored class of lipids consists of fully saturated glycerophospholipids with two acyl chains of differing lengths. Although these species are present at low abundance in eukaryotic membranes, highly abundant sphingomyelins can exhibit even greater acyl chain length asymmetry of up to 10 carbons in extreme cases.[187] Notably, these lipids are upregulated in some organisms during environmental or physiological stress, with average acyl chain length differences ranging from 6 to 8 carbons.[152, 153] These chain asymmetric lipids have been shown to alter acyl chain packing, which can lead to changes in membrane melting temperature, temperature sensitivity, oxygen adaptability, and fluidity.[5, 87, 188-191] To accommodate the mismatch in chain length, membranes typically adopt two main structural responses: interdigitation, in which longer chains penetrate into the opposing leaflet, and backbending or snorkeling, where chains fold back toward the aqueous interface.[88, 160, 164, 188, 189, 192].[162] These dynamic structural adaptations influence a wide range of biophysical membrane properties and have been observed in both molecular dynamics simulations and experimental systems.[88, 193] Understanding how these asymmetric lipids affect membrane structure and mechanics is crucial for clarifying their role in influencing membrane properties biologically.

The two modes of chain packing (i.e., interdigitation and backbending) can have a significant influence on membrane behavior. In one case, it was shown that increasing the difference in chain length between the acyl chains promotes interdigitation.[88, 164, 188, 190] This increased interdigitation increases van deer Waals interactions between the two leaflets resulting in greater the interleaflet friction.[6, 194, 195] Additionally, another study demonstrated that the acyl chains in chain asymmetric lipids are highly dynamic.[190] This dynamic behavior can generate voids within the membrane, and acyl tails must continually adjust to fill these spaces, as unfilled voids can introduce local stress and destabilize membrane structure.[72] As a result, acyl chains are more likely to interact with

carbons in their own leaflet, reducing interactions between two leaflets and leading to the formation of softer bilayers. While it has already been shown that asymmetric lipids form more compressible, softer membranes[5, 196, 197], to our knowledge, quantification of these acyl chain dynamics – including interdigitation and backbending – has not yet been done.

Here, we employed all-atom molecular dynamics simulations to quantify the propensity of acyl chains to interdigitate and backbend, in order to determine whether the positional arrangement of acyl chains on the glycerol backbone differentially influences interleaflet mechanical coupling, or if all forms of acyl chain asymmetry exert equivalent effects on bilayer mechanics. We examine a series of lipids that each contain a total of 32 carbon atoms across their two acyl chains but vary in the degree of chain length asymmetry. We then quantify the extent of interdigitation in the bilayers and implement a modified methodology from ref[198] to assess acyl chain backbending. These simulations enable a direct comparison of how the positional arrangement of acyl chains on the glycerol backbone in chain-asymmetric lipids influences bilayer structural and mechanical properties.

3.3 Methods

3.3.1 Simulation Protocol

For this work, we followed a similar protocol to that decribed ref.[87] When we started this project, all mixed-chain lipids (MSPC, 15:0-17:0PC, 17:0-15:0PC, and SMPC) were unavailable in the CHARMM-GUI web server. To build these lipids, we first constructed bilayers using 100 lipids per leaflet (200 lipids total) of 18:0-18:0 PC. Each bilayer was solvated with 45 waters per lipid and no salt ions. The mixed-chain lipids were generated by removing the terminal methyl group and the appropriate number of methylene segments from the *sn*-1 and/or *sn*-2 chains, along with all their associated hydrogens, to achieve the desired chain length. For example, for 15:0-17:0 PC, modifications were made on the *sn*-1 chain, (C317-C318 in CHARMM Notation), while on the *sn*-2 chain, only the hydrogens from the C218 chain were altered. A new terminal methyl group was formed by converting the final two carbons (C316 and C218) to hydrogens by updating their atom names, types and partial charges accordingly. The two

hydrogens on the new terminal methyl carbon were also adjusted to match the atom name, type, and partial charge characteristic of terminal methyl group hydrogens.

All simulations were run with NAMD software[199] using the CHARMM36 force field[86, 170] for lipids. The mixed-chain bilayer systems (MSPC, 15:0-17:0PC, 17:0-15:0PC, and SMPC) were energy minimized for 1200 steps, then simulated for a total of 1 ns with an integration time-step of 1 fs before the production run, which used a 2 fs time-step. The DPPC bilayer was equilibrated following the CHARMM-GUI 6-step equilibration protocol. All simulations were run at a constant temperature of 50°C (323.15 K) and a constant pressure of 1 atm using NAMD's Langevin thermostat and Nose-Hoover barostat, respectively. Long-range interactions were modeled with a 10-12 Å Lennard-Jones potential using NAMD's *vdwForceSwitch-rigidbonds* parameter set to "all". The Particle Mesh Ewald (PME) method with grid spacing set to 1 Å was used to model electrostatic interactions. An autocorrelation function from ref[171] was used to confirm bilayer area convergence. Once equilibration was confirmed, each system was simulated for an additional ~ 1 μs. The length of the trajectories were: MSPC, 0.991 μs; 15:0-17:0 PC, 1.01 μs; DPPC, 1.02 μs; 17:0-15:0 PC, 1.04 μs, and SMPC, 0.983 μs. For the MSPC and DPPC simulations, the data has previously been published in ref[88]. Prior to analysis all systems were centered with Visual Molecular Dynamics (VMD)[173] by using the center of mass (COM) of the terminal methyl groups to $z = 0$. We define the top leaflet as that in which the average *z*-position of the headgroup phosphorus atoms has a positive value.

3.3.2 Analysis Methods

To determine the biophysical properties of each of the membranes, we evaluated eight key properties: (1) area per lipid, APL; (2) bilayer thickness; (3) area compressibility modulus, K_A; (4) bending rigidity, κ; (5) polymer brush mechanical coupling constant, β; (6) *sn*-1 and *sn*-2 order parameters, S_{CD}; (7) acyl chain interdigitation; and (8) acyl chain backbending. All reported values represent time-average measurements over the production trajectories. Unless otherwise stated, errors were calculated using a blocking method described in ref.[200]

In each system, when chain length difference is referenced, it corresponds to the length asymmetry between the two acyl chains adjusted for the tilt of the glycerol backbone. This is quantified using the following equation from ref[201].

$$Chain\ Inequivalence = \left|\frac{n_1 - n_2 + 0.5}{CL}\right| \quad (3.1)$$

where n_1 and n_2 are the number of carbons in the *sn*-1 and *sn*-2 chains, respectively, and CL is the length of the longer acyl chain. The quantity +0.5 in the numerator accounts for the ability of the *sn*-1 chain to extend deeper into the bilayer due to the inherent tilt of the glycerol backbone as described in ref[201].

3.3.2.1 Area per lipid, bilayer thickness, and chain order parameters.

To calculate the APL, the *x*- and *y*-dimensions of the simulation box were multiplied to obtain the total bilayer surface area, which was then divided by 100 (the number of lipids per leaflet). The area per chain (APC) is typically defined as the APL divided by the number of acyl chains per lipid. Although the relationship between APC and bending rigidity has been shown to follow a power law in symmetric bilayers,[108, 202] these studies have largely focused on lipids where the chains have similar length.[108] For lipids where the two acyl chains differ substantially in length, it cannot be assumed that each chain occupies an equal area. Therefore, we computed the area per chain using a two-dimensional Voronoi tessellation implemented via an in-house MATLAB[203] script.

Bilayer thickness was determined by calculating the distance between the center of mass of the phosphorus atoms in the top leaflet and that of the bottom leaflet.

Chain order parameters were calculated using Eq (3.2)[204]:

$$\boldsymbol{S_{CD} = \frac{1}{2}\langle 3cos^2\theta - 1\rangle} \quad (3.2)$$

where θ is the instantaneous angle between a given C-H bond vector and the bilayer normal. To characterize the overall acyl chain order, we averaged S_{CD} over the entire length of each acyl chain. This approach allows for comparisons of chain order between lipid species that differ only in how their asymmetric chains are positioned, while having the same acyl chain composition and/or total number of carbons.

3.3.2.2 Bending rigidity and area compressibility

The area compressibility, K_A, was calculated using the per-leaflet method described by Doktorova et al.[205] This approach allows compressibility to be determined independently for each leaflet rather than as a bulk bilayer property. This method uses MEMBPLUGIN[177] heightmap in VMD tool to determine the local thickness fluctuations per leaflet. Although our bilayers are symmetric in both composition and lipid number, we used the per-leaflet method because it reduces noise from global bilayer undulations and provides more precise, localized measurements of membrane mechanics.[205] This method has also been validated against the polymer brush model (PBM)[205], which we applied later in our analysis. The error in this method is calculated by a 2D bootstrapping method described in ref[205].

Multiple approaches exist for determining the bending rigidity of simulated lipid bilayers.[206] Here, we implemented the real space fluctuation (RSF) method from ref[108]. This method builds on the theoretical foundation of the Helfrich Hamiltonian connecting local real-space fluctuations, such as lipid tilt moduli and thickness variations, to macroscopic mechanical properties. In the RSF method, each lipid is assigned a director vector from its hydrocarbon tail to its head. The splay angle between a lipid's director vector and those of its neighbors within a 10 Å radius is computed over time. A potential of mean force (PMF) is then constructed from the probability distribution of these splay angles. In the regime of small splay angles (< 20°), the PMF is fit with a quadratic function, which yields the splay modulus as the coefficient. The splay modulus can be related to the bending rigidity of the bilayer through elastic theory.[110, 207]

3.3.2.3 The polymer brush model

The polymer brush model describes the behavior of polymer chains that are tethered to a surface.[208] At high grafting densities, steric repulsions between chains drives chain extension to minimize overlap.[209] If the chains are unable to sufficiently cover the surface area, the chains adopt a more disordered conformation to maximize area coverage. This theory has been applied to lipid bilayers to describe interleaflet mechanical coupling and its effect on membrane elasticity. The mechanical coupling of the two leaflets is defined by Eq (3.3).[209, 210]

$$\frac{\kappa}{K_A} = \beta d^2 \quad (3.3)$$

where d is bilayer thickness and β is the dimensionless mechanical coupling constant. In the context of lipid bilayers, it has been theorized that if the two leaflets can slide freely past each other, then β will approach a value of 1/48. Conversely, if the two leaflets are strongly coupled, then β will approach a value 1/12. [211]This theory suggests that the β that most accurately describes lipid bilayers is 1/24.[205, 211]

3.3.2.4 Interdigitation

Interdigitation refers to the phenomenon where one acyl chain extends past the bilayer midplane and interacts with atoms from the opposing leaflet.[88] To quantify this behavior, we implemented four methods for quantifying interdigitation as described in ref[88]: the MEMBPLUGIN *Lipid Interdigitation* tool (memIT), carbon contact matrix (ccMat), density overlap matrix (doMat), and normalized interfacial surface area (nISA). Briefly:

1. memIT has three approaches for quantifying interdigitation for user-selected atoms: (1) calculates the width of the mass density overlap (w_p), (2) the fraction of interleaflet atomic contacts within 4 Å (I_C), (3) the fraction of the mass overlap (I_p) between acyl chain carbons of the two leaflets. In this study, we employed the third metric, I_p, to quantify the degree of interdigitation.
2. Additionally, interdigitation can be quantified by the number of direct carbon–carbon interactions between the two leaflets. A matrix is populated where each cell represents a specific carbon–carbon interaction between carbons in opposing leaflets. The sum of this matrix quantifies the average number of carbon contacts between leaflets and is referred to as the ccMat.[88]
3. The doMat method uses number density profiles of individual carbon atoms from each leaflet. The overlap area between density distributions of opposing leaflet carbons is calculated and stored in a matrix, similar to ccMat, where each cell represents the area of density overlap for a specific carbon–carbon pair.
4. Our previous work has shown that the midplane surface area per lipid is correlated with the extent of interdigitation.[88] This effect is quantified by nISA

calculated from a 3D Voronoi tessellation. Atoms from opposite leaflets are considered neighbors if their respective Voronoi cells share a face. The sum of these shared face areas defines the total interfacial surface area. This value is then normalized by the average area per lipid (APL) to obtain the interfacial surface area per lipid.

All methods employed a cutoff distance of 4 Å to define interleaflet interactions except nISA where cutoff distances are inapplicable.[88]

3.3.2.5 Acyl chain backbending

In fluid-phase bilayers, acyl chains exhibit flexibility, and their terminal methyl groups may transiently bend back toward the headgroup region - a phenomenon known as lipid snorkeling or backbending.[43, 212] While inherently difficult to define due to the absence of a strict spatial threshold, backbending is further complicated by the need to identify interactions occurring within the same acyl chain and with other molecules in the same leaflet. This contrasts with interdigitation, which can easily be defined by molecular interactions of atoms in opposing leaflets.

A previous study attempted to quantify backbending by measuring the distance between a headgroup carbon and the center of mass of the terminal methyl group.[198] However, applying this method directly to our chain-asymmetric systems is challenging, as the inherent chain length differences (i.e., between 14:0 and 18:0 chains) affect the spatial interpretation of snorkeling. To account for this, we calculated the maximum extension length of each acyl chain, defined as the distance between each *sn* carbonyl carbon and the center of mass of the terminal methyl group. We then defined snorkeling events using threshold values ranging from 90% to 10% of this maximum length, in 10% intervals. We observed that thresholds between 70% and 40% of the maximum chain length most reliably captured backbending behavior, minimizing over- and under sampling artifacts. An example of what the histograms and threshold values look like are shown in (**Appendix 3.1**) These thresholds better identified meaningful backbending events, whereas more permissive or restrictive thresholds disproportionately captured noise or missed significant interactions.

3.4 Results and Discussion

Our primary goal was to investigate how fully saturated mixed-chain lipids influence bilayer properties by comparing single-component bilayers composed of lipids with the same total number of acyl chain carbons, but with those carbons distributed unequally between the two chains. Specifically, we examined four mixed-chain phosphatidylcholines—MSPC, 15:0-17:0 PC, 17:0-15:0 PC, and SMPC—in which the total acyl chain length remains constant at 32 carbons (**Figure 3.1**). Although some of these lipids differ only in the positional arrangement of the acyl chains on the glycerol backbone, the intrinsic tilt of the glycerol backbone causes a vertical offset in which the *sn*-1 chain extends deeper into the bilayer. To isolate the effects of glycerol backbone tilt in the absence of chain asymmetry, we also examined DPPC, which has identical saturated chains in both *sn*-1 and *sn*-2 positions.

3.3.4 Chain Length Mismatch Drives Changes in Bilayer Structure

In this study, all examined lipids possess identical total numbers of carbon atoms distributed between their two acyl chains and share the same headgroup. Consequently, we hypothesized that the APL would remain approximately constant given all lipids have the same number of acyl chain carbons. This hypothesis is consistent with previous small-angle neutron scattering data for SMPC, MSPC, and DPPC.[87] However, our findings show that the APL differs slightly across all five lipid species studied and are within error from previously determined values for MSPC, SMPC and DPPC[87] (**Figure 3.2a**). This trend persists when considering both the chain length difference and the carbon number disparity between the two acyl chains. Notably, an increase in chain mismatch correlates with an increase in APL.

Changes in acyl chain length typically influence bilayer thickness.[213] Since one chain is being lengthened while the other is shortened, the change in bilayer thickness will depend on the midplane acyl chain interactions such as interdigitation and backbending. Greater interdigitation promotes tighter leaflet packing, which manifests as a thinner bilayer (discussed further in Section 3.3).[214, 215] Accordingly, we observe a reduction in bilayer thickness that scales with increasing chain mismatch. **(Figure 3.2b)**

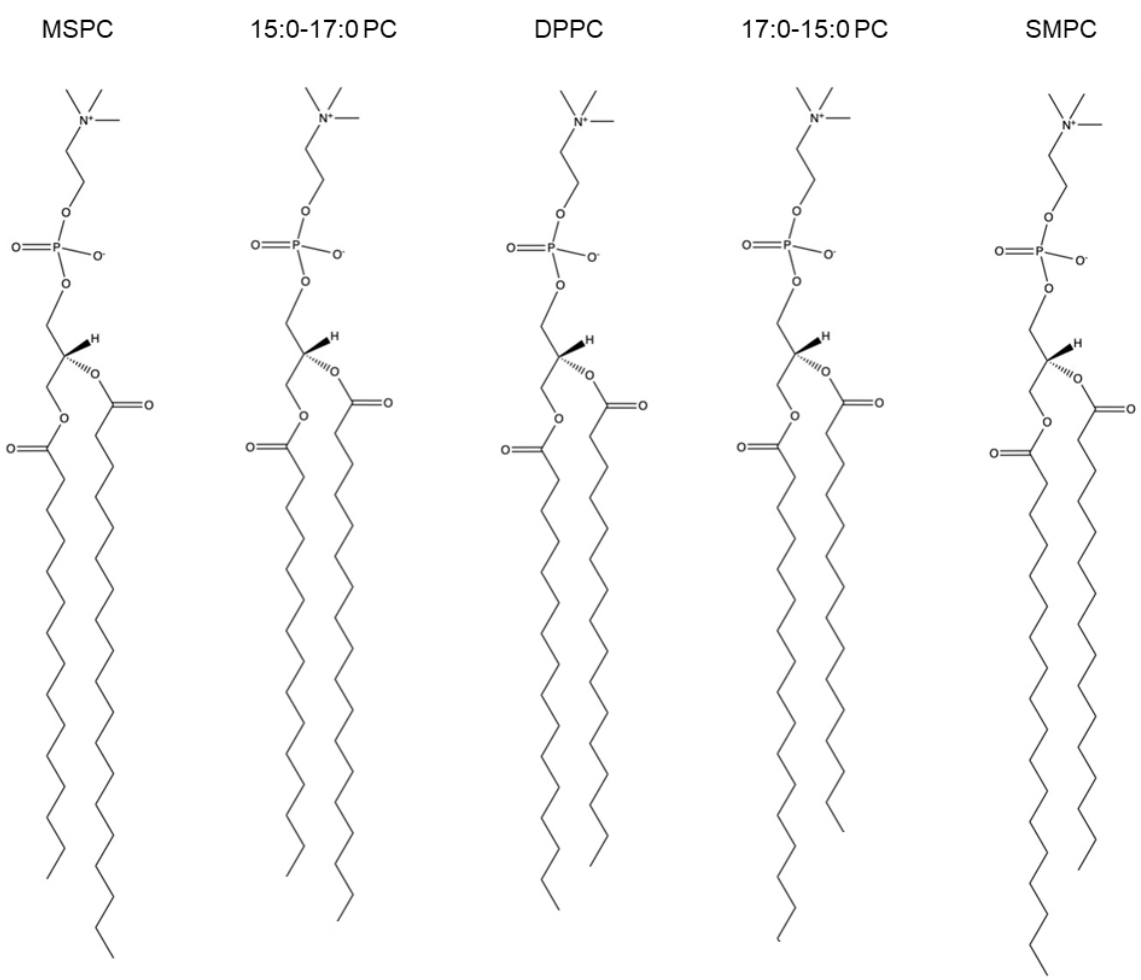


Figure 3.1) Lipids in this study. From left to right, the sn-1 chain increases in carbon number while the sn-2 chain decreases to maintain a total of 32 acyl chain carbons.

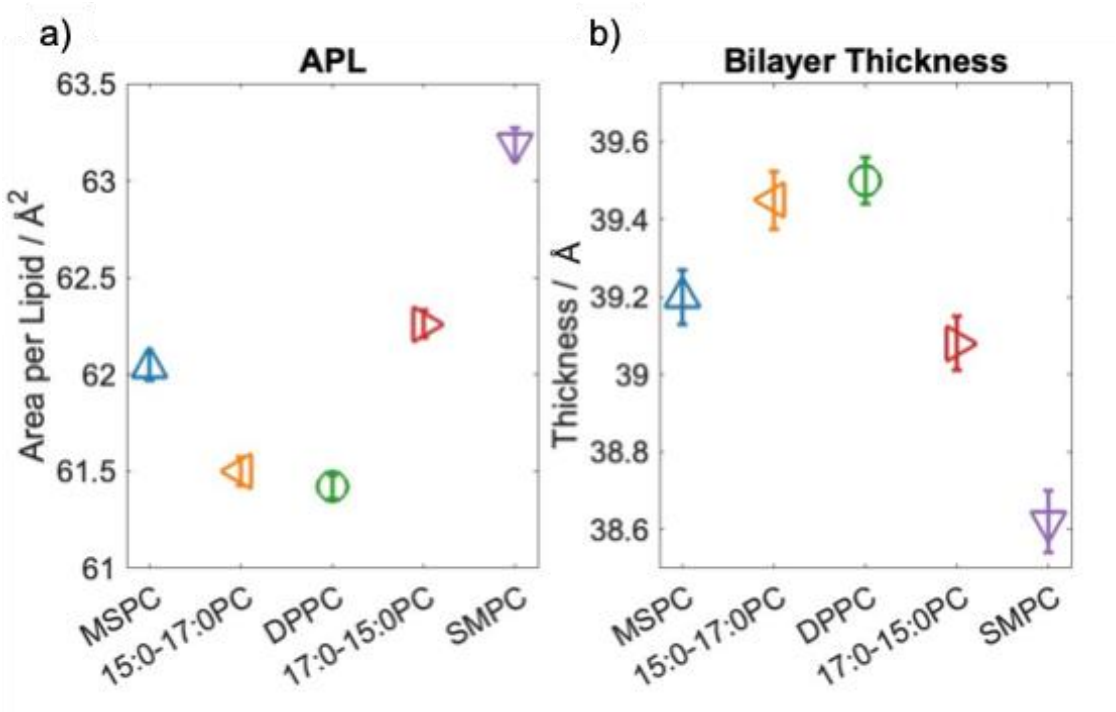


Figure 3.2) APL and bilayer thickness of mixed chain lipid bilayers. (a) APL for lipid bilayers with increasing chain mismatch. The lipid with the highest chain length difference has the highest APL. Knowing that the higher APLs form thinner bilayers, the trend agrees in (b) where the APL and bilayer thickness are inversely proportional.

Chain order also plays a critical role in modulating bilayer thickness and APL.[4, 157, 166] Although longer acyl chains have more conformational degrees of freedom, they tend to adopt more ordered configurations in fluid-phase bilayers due to increased van der Waals interactions and tighter packing.[39, 213] This increase in flexibility is typically attributed to either an increase in acyl chain length or the introduction of unsaturation. In our analysis of chain order parameters, the shorter 14:0 chains exhibit higher order compared to the longer 18:0 chains. (**Appendix 3.2**) Moreover, the positional dependence of chain order becomes more pronounced with increasing chain length, supporting the notion that *sn*-2 chains display greater disorder than *sn*-1 chains. (**Figure 3.3**). This disparity intensifies as chain length increases suggesting that the backbone tilt is a contributor to acyl chain dynamics.

3.4.2 Chain Mismatch Drives Changes in Mechanical Properties.

Lipid bilayers can be imagined as a hydrophobic region sandwiched between two headgroup layers. Depending on how tightly the acyl chains are packed, this can influence K_A and therefore change its compressibility, or how easy the bilayer can be compressed. It has been previously reported that chain asymmetric bilayers are more compressible than their symmetric bilayer counterparts.[5, 196, 197] The bilayers that had the longer chain on the *sn*-1 position had lower K_A values than that the lipids that have the chains transposed (**Figure 3.4a**). This further suggests that the positioning of the acyl chains on the glycerol backbone is highly influential in bilayer properties.

K_A quantifies a bilayer's resistance to lateral expansion or compression, while κ describes its resistance to bending. These moduli are often correlated as both are strongly influenced by the degree of acyl chain packing.[185, 216] This correlation remains true in the case of mixed-chain lipid bilayers (**Figure 3.4a**). All lipids examined adhere to the previously established power-law relationship between APC and κ described in ref.[202] (**Appendix 3.3**) Furthermore, increasing chain length mismatch is associated with a decrease in κ, a trend also observed in earlier work[6].

Some simulations have shown that K_A may exhibit size-dependent behavior which can result in an artificial correlation of κ, particularly in systems with structural or compositional complexity.[205, 217, 218] To account for these complexities, researchers have

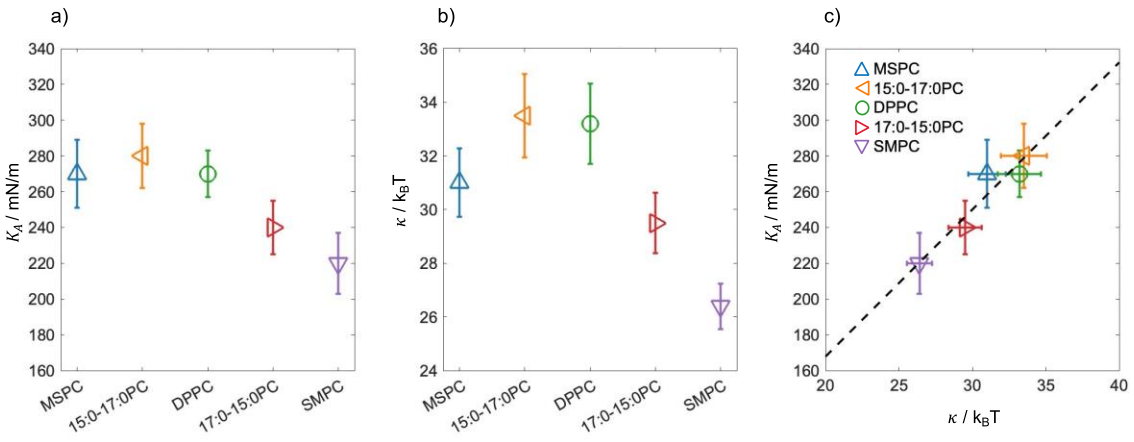


Figure 3.3) Mechanical properties of mixed chain lipid bilayers. (a) is the bilayer K_A for each of the mixed chain bilayers. (b) is κ for each of the mixed chain bilayers. K_A and κ are positively correlated. Mixed-chain lipid bilayers maintain this trend (c).

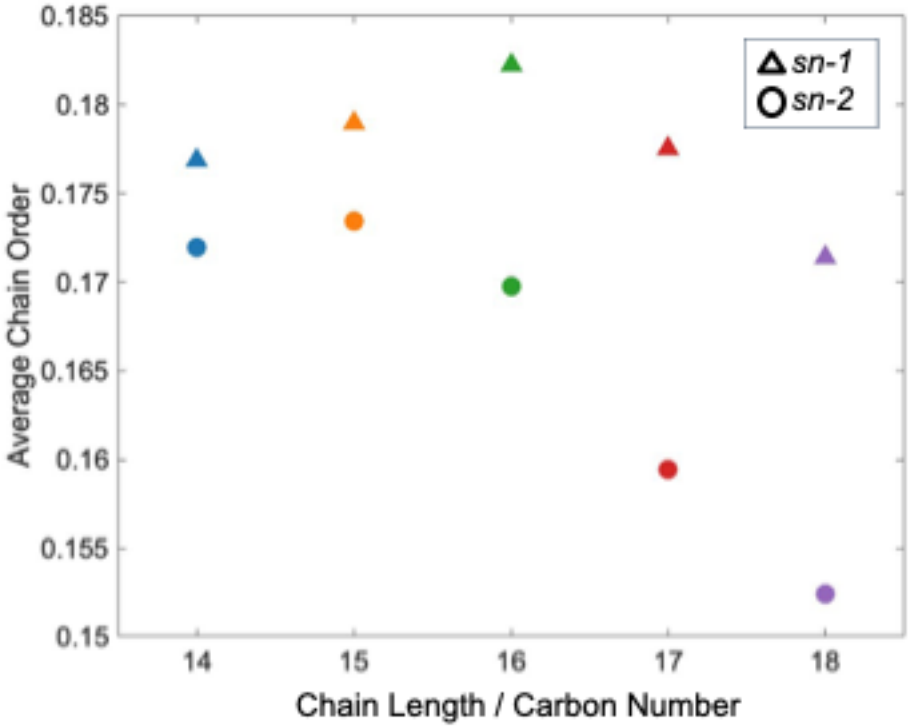


Figure 3.4) Average order parameters for *sn*-1 and *sn*-2 chains. The values represent the mean order parameters across the entire acyl chains, plotted as a function of acyl chain length and backbone position. Increasing chain length reveals differences in backbone positioning associated with disorder.

implemented the PBM to quantify the mechanical coupling of two leaflets in a bilayer.[211] In principle, increased interdigitation should enhance the mechanical coupling of the two leaflets, and should be reflected by an increase in κ. However, this assumption does not hold in all cases: both experiments[6] and simulation results indicate mixed chain lipids deviate from this assumption, forming bilayers significantly less coupled than their symmetric counterpart (here, DPPC) with the exception of 15:0-17:0 PC which has a similar chain length difference comparable to DPPC. To describe the mechanical coupling of the two leaflets we calculated β from the PBM and found that increasing the chain length mismatch did not significantly change the mechanical coupling of the two leaflets. (**Figure 3.5**)

3.4.4 Chain asymmetric lipids have a higher propensity to interdigitate and backbend.

It has been shown that other chain asymmetric lipids prefer to adopt two predominant conformations: interdigitated, or back-bent.[190] Nevertheless, lipid acyl chains are highly dynamic in the fluid phase[75] and are capable of rapidly sampling multiple conformations on short timescales[88] and should also occur transiently and dynamically within fluid bilayers. While interdigitation is often conceptualized as a complete "zippering" of the leaflets into a specific phase[214], we instead focus on instantaneous interdigitation recognizing it as a transient, dynamic phenomenon in fluid phases.

To quantify the extent of interdigitation in each of these systems, we applied the four methods described in ref[88]. The values for each of these methods are presented in **Figure 3.6** and in **Appendix 3.4**. All four methods consistently indicate that increasing the chain length disparity between the two acyl chains enhances the extent of interdigitation between the leaflets. When normalized, these metrics exhibit the same overall trend that is best fit with a second order polynomial (**Appendix 3.5 and 3.6**), confirming that greater chain length mismatch leads to increased interdigitation. This finding challenges the traditional view that enhanced interleaflet interactions, such as those arising from interdigitation, should result in stiffer bilayers.[219] As seen in **Figure 3.4b**, and in an experimental study[6], increasing the chain mismatch decreases the bending modulus of the bilayer. However, it has been seen that highly chain asymmetric lipids like to adopt two main conformations: interdigitated and backbent configurations.[190]

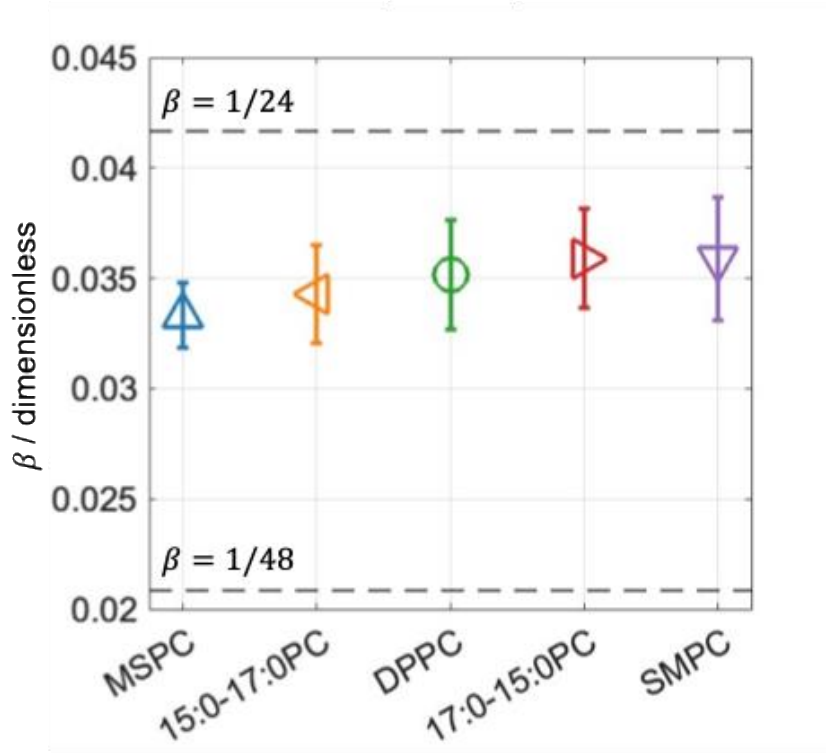


Figure 3.5) PBM values for mixed-chain bilayers. Increasing chain-length mismatch does not significantly alter the mechanical coupling constant, despite observable differences in other mechanical properties.

.

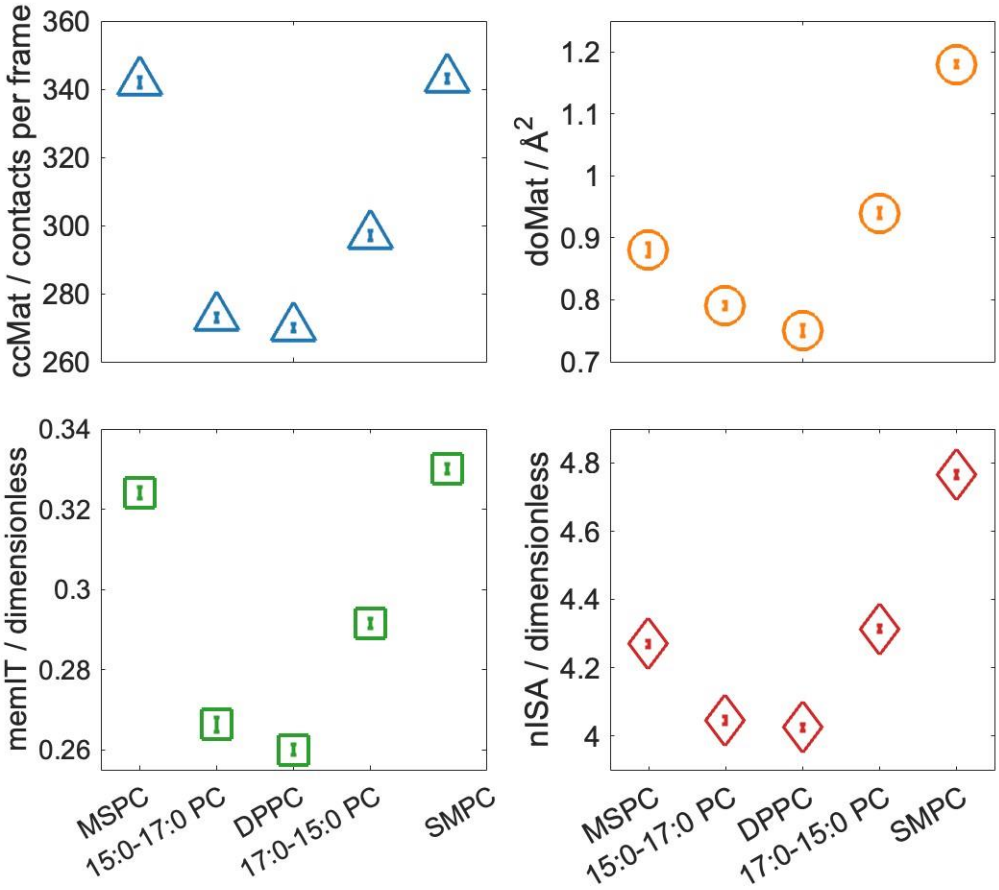


Figure 3.6) Quantification of interdigitation using four methods: ccMat, doMat, memIT, and nISA. All methods consistently show that increasing ΔCL results in greater interdigitation. Panels show (a) ccMat sums, (b) doMat sums, (c) memIT values, and (d) nISA values. While the absolute values differ across methods, normalization reveals highly similar trends (Appendix 3.5).

chains to backbend. At 80 ps intervals, we computed the distance between the carbonyl carbon and the terminal methyl group for each acyl chain and evaluated whether this distance fell below a series of incrementally adjusted thresholds, thereby classifying chains as backbent or not. The use of the carbonyl carbon as a reference point accounts for intrinsic chain offset caused by the tilt of the glycerol backbone, ensuring that differences observed are attributable to chain disorder rather than chain positioning. This distinction is important, as it was determined that the *sn*-1 position on the glycerol backbone is intrinsically more ordered than the *sn*-2 position **(Figure 3.3**). As shown in **Figure 3.7**, the relative ranking of backbending behavior across systems remains consistent regardless of the specific threshold applied (expressed as a percentage of the maximum chain length). This supports the notion that systems with a higher degree of interdigitation also exhibit an increased propensity for backbending. Moreover, increasing the chain length mismatch appears to follow a second-order polynomial with both interdigitation and backbending **(Appendix 3.5, 3.6, and 3.7**), suggesting a shared underlying mechanism related to chain asymmetry and packing disorder previously established.[87]

Although the trends between interdigitation and backbending are similar, it is not necessarily accurate to conclude that increasing chain length mismatch directly induces the same second order polynomial increase in backbending propensity. Importantly, our data suggest that the propensity to backbend correlates more strongly with acyl chain mismatch in all threshold levels than with interdigitation. This distinction is critical, as interdigitation is not solely a monolayer property. For an acyl chain to interdigitate, two conditions must be met: (1) the packing density within its own leaflet must be sufficiently high to drive the chain into the opposing leaflet, and (2) the opposing leaflet must contain a void large enough to accommodate the intruding chain. In contrast, backbending is governed primarily by intraleaflet physical properties, such as chain flexibility and local packing. This difference is particularly evident under the strictest classification threshold (40% of the maximum chain length), where the correlation between chain mismatch and backbending is strongest, with an R^2 value of 0.993. The R^2 values for all other threshold models are listed in **Appendix 3.7**.

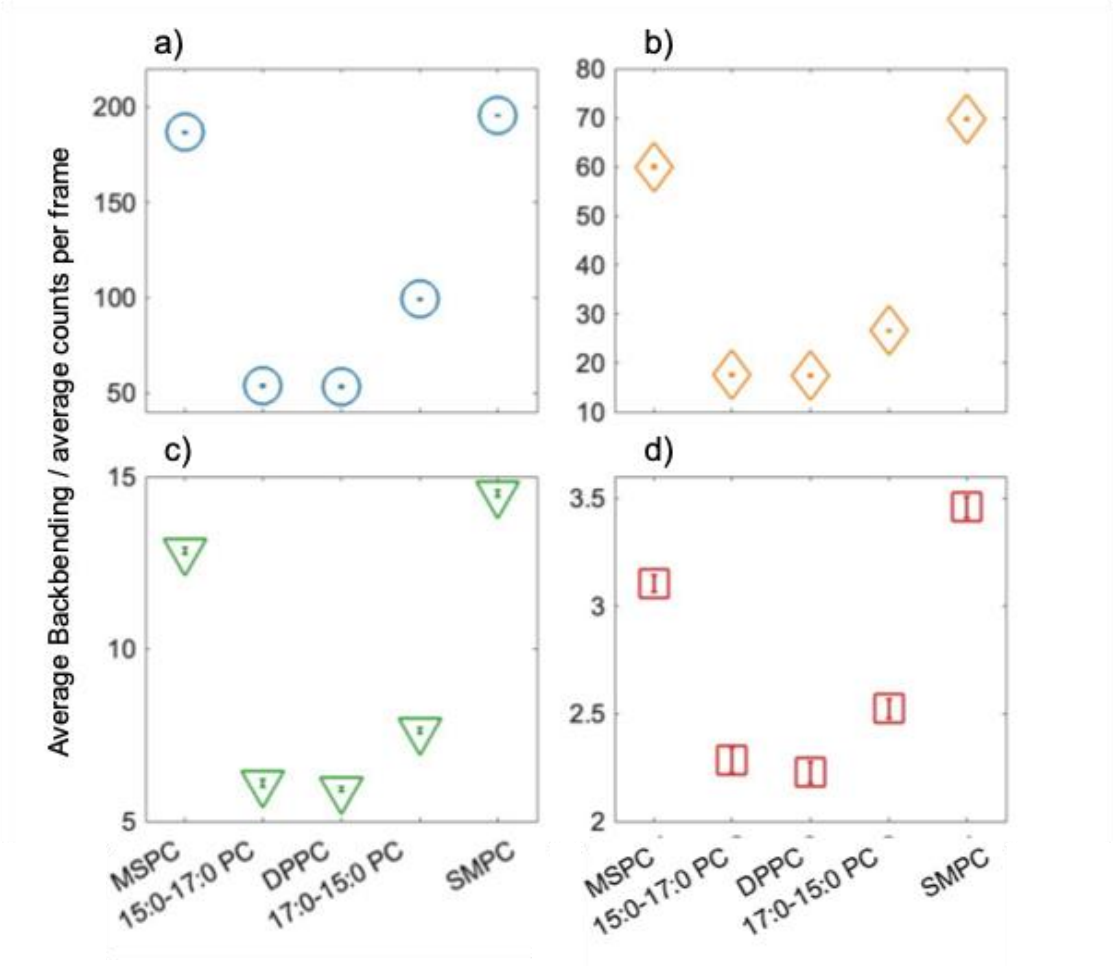


Figure 3.7) Average number of backbending acyl chains as a function of increasing fractional chain length threshold. Reducing the threshold from 70% to 60% of the maximum chain length (panel a) results in over a 50% decrease in the number of identified backbending chains. Despite changes in threshold criteria (down to 50% and 40%), SMPC consistently exhibits the highest number of upward-snorkeling chains. Fitting the data with a second-order polynomial reveals a strong correlation between backbending and carbon chain-length difference

3.5 Summary and Conclusions

One leaflet of a lipid bilayer is mechanically coupled to the opposing leaflet, and the strength of this coupling depends on both the structural features of the constituent lipids and additional properties such as lipid composition and asymmetry.[4, 164] We investigated how a difference in acyl chain length of chains on the same backbone affects the physical properties of the bilayers that they form. Specifically, we examined lipids with saturated acyl chains ranging from 14:0 to 18:0, varying the carbon number on one chain while decreasing it on the other, to assess whether chain positioning on the glycerol backbone influences bilayer behavior.

We observed modest variations in structural properties, such as an increase in APL with greater chain length mismatch. This may be attributed to enhanced chain dynamics in systems like SMPC, where the more disordered chain resides in the inherently more dynamic *sn*-2 position. This configuration appears to promote a softer bilayer, increased backbending, and higher APL, consistent with the idea that more dynamic chains reduce frictional interactions between the leaflets. This reduction in interleaflet friction could help explain the observed softening of bilayers in both simulations and experimental measurements[6]. Furthermore, these findings may clarify why SMPC and MSPC—despite differing only by the positional swap of the two acyl chains—exhibit distinct physical and mechanical bilayer properties.

Biologically, many naturally occurring lipids are asymmetric, possessing chains of differing lengths and degrees of unsaturation.[2] This basic biophysical analysis demonstrates how minor structural variations can lead to significant differences in bilayer properties, potentially offering insight into why such lipidomic diversity is essential for cellular function. In some organisms such as yeast, shifts in mixed-chain lipid composition are observed under stress, possibly as a protective or adaptive mechanism.[189] Future studies are needed to explore how these hybrid lipids behave in more complex, biologically relevant systems (for example, compositionally and numerically asymmetric bilayers) to determine whether chain mismatch continues to dominate leaflet coupling dynamics under such conditions.

CHAPTER FOUR
PHENOMENOLOGICAL MODELS FOR DETERMINING PHASE BEHAVIOR OF LIPOSOMES FROM SP-FRET

A version of this chapter is being prepared for submission as a manuscript.

Emily H. Chaisson, Deeksha Mehta, and Frederick A. Heberle "Phenomenological models for determining phase behavior of liposomes from SP-FRET"

This chapter describes experiments and method development. D.M., and E.H.C., performed the FRET experiments. E.H.C performed the analysis. D.M., E.H.C., and F.A.H. designed the research, analyzed the data, and wrote the manuscript. D.M., E.H.C., and F.A.H. edited the manuscript.

4.1 Abstract

Steady-state probe partitioning Förster Resonance Energy Transfer (SP-FRET) has been a widely used technique for identifying nanoscopic heterogeneity in model membranes. The use of two-probe-pair acceptor fluorescence measurement systems has enabled detailed characterization of phase behavior in phase-separated systems on a nanoscopic scale.[29] Historically, this method has relied on one or two probe pairs to qualitatively estimate the miscibility transition temperature of lipid mixtures. More recently, quantitative models incorporating up to five fitting parameters have been developed.[8] In this work, we introduce an algorithm to assess whether a given system undergoes a miscibility transition over a defined temperature range. Our approach compares the reduced chi-square χ^2_{red} from each model to determine if it is statistically just to use the more complex model values from 3-, 4-, and 5-parameter model fits and establishes empirical thresholds to determine when the added complexity of a higher-order model is statistically justified. We validated this method using well-characterized homogeneous and phase-separated lipid mixtures and demonstrated that it reliably detects phase separation, including in nanoscopically heterogeneous systems. We have provided an open-source, user-friendly, implementation of this analysis framework for application in SP-FRET in biomembrane studies.

4.2 Significance

FRET can determine phase behavior in lipid membranes using two probe pairs: one in which both probes prefer the same phase and another in which both probes prefer different phases. Despite FRET being used to resolve nanoscopic heterogeneity, determining whether an increased signal is an artifact of the method, or the result of the sample being a non-ideal mixture is still challenging. Here, we implement 3-, 4-, and 5-parameter models to assess if a system has domain formation. This method has been used to determine the miscibility transition temperature in phase separated samples for two well-studied mixtures, DPPC/DOPC/Chol and DPPC/POPC/Chol, and to fit a single component system (DOPC). Additionally, we determine the phase boundary in a 1:1 (DPPC/DOPC) + various amounts of cholesterol trajectory using the χ^2_{red} of the model fits.

4.2 Introduction

Förster resonance energy transfer (FRET) is a photophysical process where a fluorophore (donor) is electronically excited and transfers its excitation energy to another fluorophore (acceptor). For FRET to occur, the emission spectra of the donor fluorophore (*D*) must overlap with the excitation spectra of the acceptor fluorophore (*A*). The transfer of energy is distance-dependent and can yield measurements on the nanoscopic scale, making FRET highly applicable for many biological applications[142, 147]. One specific application utilizes steady-state probe-partitioning fluorescence resonance energy transfer (SP-FRET), which exploits the tendency of phase-preferring probes to partition selectively into distinct membrane domains.[141] SP-FRET has been used to determine the phase behavior[8], miscibility transition temperatures[8, 220], and even domain size in lipid bilayers[128]. SP-FRET is used to assess these properties by quantifying subtle changes in the FRET efficiency. An increase or decrease the FRET efficiency is governed by the distance between the *D* and *A*. In these studies, *D* and *A* are fluorescent lipid probes, and because the FRET mechanism is distance-dependent, FRET between donor and acceptor lipids depends on their average separation. Since *D* and A are themselves lipids capable of freely diffusing within the membrane plane, their separation follows a distribution of separation distances rather than a single fixed value. As a result, the FRET efficiency for any individual excited *D* is unique and depends on its instantaneous local environment, with the observed FRET representing an average over all such *D* molecules in the system. Any change that causes spatial reorganization of *D* and *A* lipids will alter the distribution of separation distances, and thus, the observed FRET efficiency**.**

One example of a change that induces spatial reorganization is temperature change in a phase-separated system. Qualitatively, there are two possibilities when a uniform mixture (**Figure 4.1c**) phase separates: (a) *D* and *A* prefer the same phase and become concentrated in the same domains, therefore FRET increases (co-localization) (**Figure 4.1a**); (b) *D* and *A* prefer different phases and therefore, FRET decreases because *D* and *A* are concentrating in different domains (segregation) (**Figure 4.1b**)

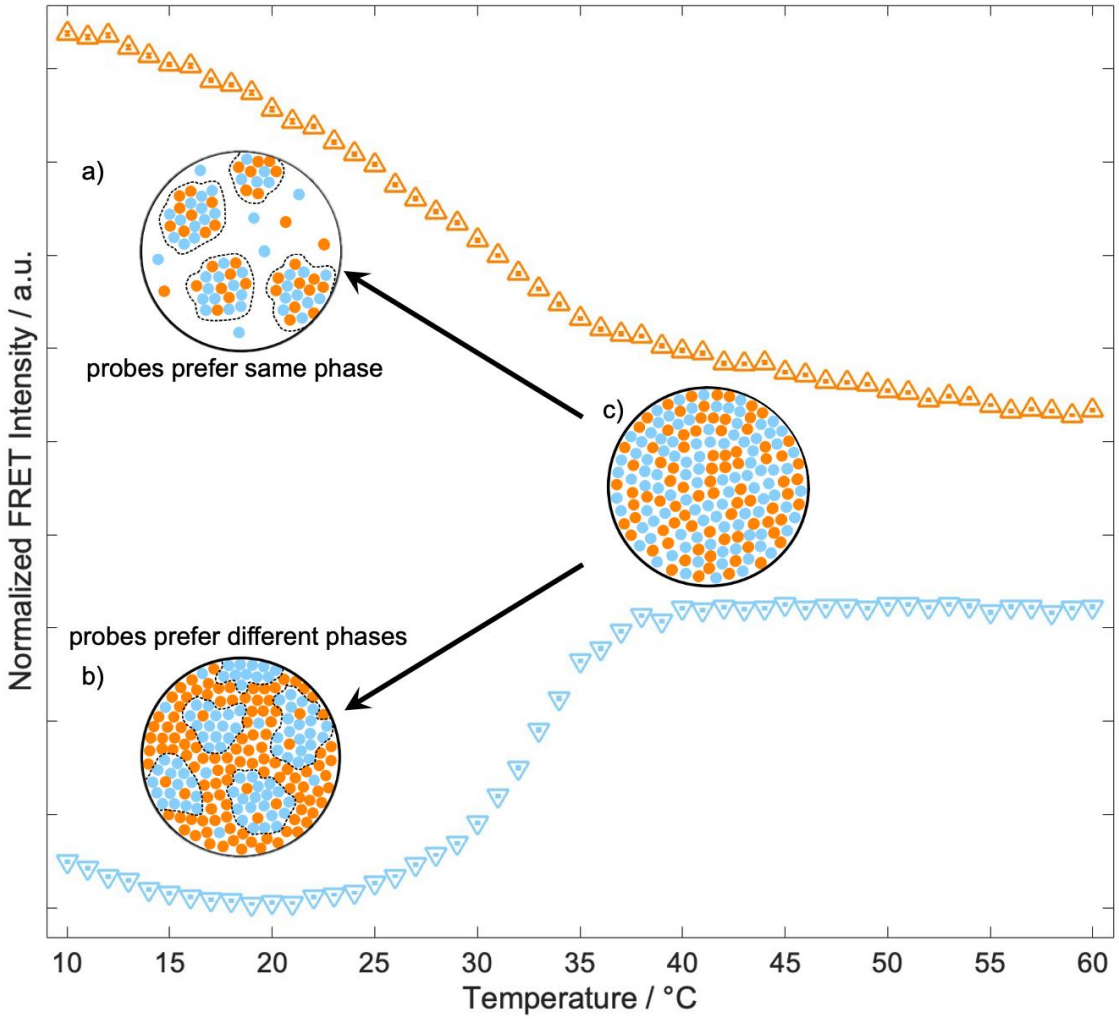


Figure 4.1) Dual probe partitioning in SP-FRET. (a) For two probes that prefer the same phase, at lower temperature regimes, the FRET intensity is going to be higher. Conversely, if two probes prefer different phases, in lower temperature regimes, then FRET intensity will be lower. (b) In temperatures above the miscibility temperature, then the sample and probes are uniformly mixed. (c) This figure is an adaptation from [140] with permission from American Physical Society.

induces a local change in environment, where the probe pair that exhibits the same phase preference has an increase in FRET intensity because of probe co-localization, while the probe pair that exhibits contrasting phase preference has a decrease in FRET intensity because of probe segregation[29]. However, in cases where there is no phase separation, there is no abrupt change in FRET efficiency. In each of these cases, the FRET intensity curves should be fit with a model to determine the phase behavior and, when applicable, the miscibility transition temperature. Here, we present a previously established methodology[8, 220] alongside a novel algorithm designed to determine whether a sample exhibits a miscibility transition over a given temperature range, and when applicable, to quantify the transition temperature. We have implemented these methods into an open-source, user-friendly tool that enables other researchers to adapt the approach for their own studies. Difficulties arise in selecting the best model when the phase behavior of the sample is unknown, leading to the main question: What model is best suited for the data, and can it be used to determine phase behavior?

4.4 Materials and Methods

4.4.1 Chemicals

Phospholipids, 1,2-dioleoyl-*sn*-glycero-3-phosphocholine (DOPC), 1-palmitoyl-2-oleoyl-*sn*-glycero-3-phosphocholine (POPC), and 1,2-dipalmitoyl-*sn*-glycero-3-phosphocholine (DPPC) were purchased from Avanti Polar Lipids (Alabaster, AL). Cholesterol was purchased from Nu-Chek Prep (Elysian, MN). 1-palmitoyl-2-(dipyrromethene boron difluoride)undecanoyl-*sn*-glycero-3-phosphocholine (TFPC) was obtained from Avanti Polar Lipids, 1,1′-dioctadecyl-3,3,3′,3′-tetramethylindodicarbocyanine, 4-chlorobenzene sulfonate salt (DiD) was obtained from ThermoFisher Scientific (Waltham, MA), and naphtho[2,3-*a*]pyrene] (naphthopyrene, Naph) was obtained from TCI America (Portland, OR). All phospholipids, dyes, and cholesterol were dissolved in HPLC-grade chloroform and stored at -20 °C until use. The concentration of cholesterol (Chol) was determined gravimetrically, and the concentration of phospholipids was determined using an inorganic phosphate assay.[221] The concentration of the fluorescent dyes was determined from absorbance measurements using the following extinction coefficients: 23,800 M^{-1} cm^{-1} (Naph), 96,900 M^{-1} cm^{-1} (TFPC), 249,000 M^{-1} cm^{-}

[1] (DiD). Ultrapure water was obtained from a Milli-Q IC 7000 purification system (Millipore Sigma, Burlington, MA).

4.4.2 Sample preparation

Vesicles of low average lamellarity (LLVs) were prepared as previously described in [127] using the rapid solvent exchange (RSE) method. First, the desired lipid and probe mixtures were prepared by dispensing stock solutions into 13 x 100 mm glass screw-cap test tubes containing 25 µL of chloroform. 500 µL of ultrapure water was added to each test tube, which was then immediately mounted on the RSE device, placed under vacuum, and subjected to vigorous vortexing for 90 s. During RSE, Ar was slowly introduced into the test tube to facilitate the removal of chloroform. After 90 s, the sample was vented to Ar and transferred to a plastic centrifuge tube.

4.4.4 FRET measurements

Following the protocol from Mehta and Crumley et al.[8], FRET samples were prepared by adding 100 µL aliquot of LLVs consisting of 0.625 µL (total lipid) and 1900 µL of ultrapure water into a plastic centrifuge tube and vortexed before adding it to fluorometer cuvette with a flea stir bar.[8] FRET from these samples was measured using a HORIBA FluoroLog 3 spectrophotometer (HORIBA USA, Irvine, CA) equipped with a temperature-controlled cuvette holder (Quantum Northwest, Liberty Lake, WA). Each sample contained three probes comprising two *D*/*A* FRET pairs: Naph/DiD and TFPC/DiD. The probe-to-lipid ratios were as follows: 1/200 Naph, 1/1500 TFPC, 1/1000 DiD. Fluorescence intensity was measured in five channels (excitation/emission λ in nm): Naph direct signal (427/545), Naph/DiD FRET (427/664), TFPC direct signal (499/551), TFPC/DiD FRET (499/664), DiD direct signal (646/664). Excitation and emission channels were selected based on the spectral overlap between each donor probe's emission and the acceptor's excitation, as shown in **Appendix 4.1**. Proper spectral overlap is essential for efficient FRET; if the donor emission and acceptor excitation spectra do not overlap, energy transfer cannot occur. We chose excitation wavelengths to maximize donor excitation while minimizing excitation of other probes. Likewise, emission channels were selected to capture the peak emission of each probe while avoiding signal overlap between channels. These considerations were critical to

accurately quantifying FRET and avoiding misinterpretation due to spectral cross-talk. In **Appendix 4.1**, excitation and emission wavelengths for each channel are shown as superimposed vertical lines, color-coded by channel, to illustrate the rationale for their selection. Excitation and emission slit widths were between 2-3 nm, and the signal integration time was 0.1 s. To establish the temperature dependence of FRET, data were collected from 60 to 10 °C in -1°C increments with an equilibration time of 2 min at each temperature, with a minimum initial equilibration time of 15 min. We refer to the Naph/DiD intensity as FRET1 and TFPC/DiD intensity as FRET2. For this application, FRET is measured by monitoring changes in acceptor fluorescence intensity, rather than the conventional approach of tracking changes in donor fluorescence.

4.3.3 FRET fitting with 3-,4- and 5-parameter models

FRET was calculated from the intensity measured in the FRET channel. The FRET (F_A^{Dem}) channel contains direct measurements from both the *D* (F_D^{Dem}) and *A* (F_A^{Aem}) fluorophores. First, we must normalize the FRET intensity using the geometric mean of the *D* and *A* shown in Eq (4.1)[8, 29].

$$FRET = \frac{F_A^{Dem}}{\sqrt{F_D^{Dem} \cdot F_A^{Aem}}} \tag{4.1}$$

As discussed previously, same-phase probes exhibit increased FRET intensity (FRET2) when the temperature is below the miscibility transition temperature ($T < T_{misc}$, where T is the current temperature and T_{misc} is the miscibility temperature). In contrast, opposing-phase probes show a decrease in FRET intensity (FRET1) under the same conditions. While these individual changes in FRET can be subtle, taking the ratio of FRET2 to FRET1 - hereafter referred to as F_{Ratio} - amplifies the sensitivity to probe co-localization and more clearly reveals the T_{misc}.222 Previously, the F_{Ratio} was fit with a 4-parameter model (or two intersecting linear regimes)[223] Eq (4.2) for both modes of the curve, with T_{misc} being the breakpoint of the piecewise function.

$$FRET(T; T_{misc}, F_{misc}) = \begin{cases} a_1(T - T_{misc}) + F_{misc} & T < T_{misc} \\ a_2(T - T_{misc}) + F_{misc} & T \geq T_{misc} \end{cases} \quad (4.2)$$

This model identifies regions of low miscibility, where $T < T_{misc}$. In this region, a_1 describes the slope and b_1 is the y-intercept. However, in regions of high miscibility, where $T \geq T_{misc}$, a_2 is the slope and $b_2 = a_1 T_{misc} + b_1 - a_2 T_{misc}$. This model neglects one aspect of dual probe FRET measurements; these probes show a gradual change in intensity throughout the experiment in a uniformly mixed bilayer with an increase in temperature or composition.[8, 141] Therefore, the 4-parameter model truncates the data to two linear regimes. Including this parabolic behavior, a more robust 5-parameter model can determine the T_{misc} by the Eq (4.3) shown below.[8, 220]

$$FRET(T; T_{misc}) = \begin{cases} \left(T^2 - {T_{misc}}^2\right) + b(T - T_{misc}) + F_{misc} & T < T_{misc} \\ c(T - T_{misc}) + F_{misc} & T \geq T_{misc} \end{cases} \quad (4.3)$$

This model identifies regions of high miscibility, where $T \geq T_{misc}$. In this region in Eq (4.3), parameter c describes the slope. The fitting regime of phase separation is more complex, where parameters a and b control the shape of the curve. In both regions, F_{misc} represents the FRET value when these two regions intersect. However, some systems, particularly uniform systems, are better fit with a 3-parameter model Eq (4.4) that will account for this gradual increase in probe signal coming from the change in temperature effect on the quantum yield rather than a change in the environment caused by preferential probe partitioning into specific phases shown by single component DOPC (**Appendix 4.2**). Parameters a, b, c all describe the fit for a simple quadratic.

$$FRET(T) = aT^2 + bT + c \quad (4.4)$$

In cases where the system is known to be phase-separated, such as DPPC/DOPC/Chol[52], determining which model best fits the data can appear arbitrary, as a phase-separated model (with 4- or 5-parameters) will always fit significantly better than a uniform (3-parameter) model. However, the 5-parameter model is often preferred over the 4-parameter model because it enables direct comparison with the 3-parameter model

without reducing the dataset size, thereby maintaining sample size consistency across model comparisons.

Many metrics can be used to evaluate the goodness-of-fit and determine the most appropriate model for a given dataset. Commonly employed criteria include the sum of squared residuals, root mean square error, and the reduced chi-squared statistic (χ^2_{red})

$$\chi^2_{red} = \frac{\chi^2}{\nu} \tag{4.4}$$

Among these, χ^2_{red} statistic is particularly informative because it incorporates the degrees of freedom as shown in Eq (4.4) where ν is the degrees of freedom, calculated by $\nu = k - n$, where k being the number of data points and n is the number of fit parameters. To determine whether a given χ^2_{red} supports a miscibility transition (i.e., phase separation), we compare the fits of a uniform model (3 parameters) against phase-separated models (4- or 5-parameter). While increasing the number of parameters often improves fit, the principle of parsimony cautions against overfitting and promotes choosing the simpler model unless the improvement in fit is statistically significant. χ^2_{red} statistic enables a fair comparison by penalizing excessive model complexity. Therefore, comparing the χ^2_{red} values -specifically, the ratio of a uniform model to the phase separated model - provides a quantitative measure of whether the improved fit from a phase-separated model justifies its added complexity.

4.5 Results and Discussion

To establish an empirical guideline for determining miscibility transitions, we examined a sample set with well-characterized phase behavior: uniform (DOPC), nanoscopic (DPPC/POPC/Chol, 40/40/20 mol%), and macroscopic (DPPC/DOPC/Chol) phase separation. We use data from Mehta & Crumley et al.[8] for mixtures spanning the known phase transition space along the 1:1 DPPC/DOPC/Chol line as cholesterol concentration varies. For each mixture, we fit the data using 3-, 4-, and 5-parameter models and report the corresponding χ^2_{red} values. The primary objective is to establish empirical criteria grounded in a set of reference samples with well-characterized miscibility behavior. This is achieved by quantifying and comparing the ratios of χ^2_{red}

values obtained from fits to DOPC, which remains homogeneous across the entire temperature range, against those derived from ternary mixtures exhibiting miscibility transitions.

4.5.1 Determining the best model in sample replicates

We examine DOPC with 10 sample replicates. This mixture is uniform, as shown in **Figure 4.2A**. Each of the 10 replicates was fit independently, and the resulting χ^2_{red} for each model and sample replicate is shown in **Appendix 4.3a**. Taking the ratio of the $\chi^2_{red_3}$:$\chi^2_{red_4}$, $\chi^2_{red_3}$:$\chi^2_{red_5}$, and $\chi^2_{red_4}$: $\chi^2_{red_5}$ for DOPC all ratios are ~1 indicating no model is a statistically better fit than the others. However, in DPPC/POPC/Chol (40/40/20mol%), the χ^2_{red} ratios increase, while the largest ratios come from the macroscopically phase-separated model of DPPC/DOPC/Chol (40/40/20mol%) as seen in **Appendix 4.3c**. The increase in the χ^2_{red} ratios suggests that the χ^2_{red} ratios have the sensitivity to resolve better fits in both nanoscopically and macroscopically phase-separated systems.

4.5.2 Determining phase behavior with different cholesterol concentrations

The 1:1 line of DPPC/DOPC/Chol has been well established to exhibit phase-separated cholesterol concentrations in some cases and uniform concentrations in others.[8, 52] Using the data from Mehta and Crumley et al.[8] for the 1:1 line of DPPC/DOPC/Chol, we fit the data with the 3-, 4-, and 5-parameter models. **Figure 4.3** shows the $F_{Ratio}(T)$ for DPPC/DOPC/Chol for increasing Chol concentrations. For each, the best model is shown in **Figure 4.3**. All curves were fit with a 3-, 4-, and 5-parameter model (**Appendix 4.4**). The best curve fit for each $F_{Ratio}(T)$ was determined by the χ^2_{red} ratios (**Appendix 4.5**) and are shown in **Figure 4.2**. The analysis indicates that the system remains phase separated up to approximately 35 mol% cholesterol, consistent with previous findings reported by ref[8,52]. However, the T_{misc} values reported in GUV studies were slightly higher, likely due to the resolution limits imposed by the diffraction of light inherent to optical microscopy.

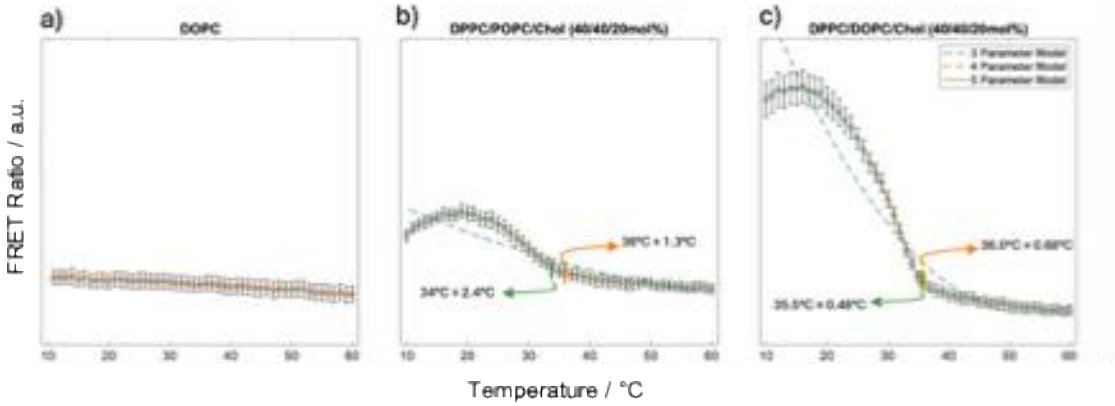


Figure 4.2) Model Fits for a uniform, nanoscopic, and macroscopically phase-separated system. (a) 100% DOPC fit with all three models. Interpreting differences between the 4- and 5-parameter model fits is not phenomenologically justified in this case, as the system is compositionally uniform and lacks detectable phase heterogeneity. However, in both (b) DPPC/POPC/Chol and (c) DPPC/DOPC/Chol the T_{misc} determined by the 4-parameter model is shown with an orange vertical line and the T_{misc} determined by the 5-parameter model is shown with a green vertical line. Each sample had 10 replicates, and the error bars are standard error of the mean. The error is determined from the error of the parameter in a weighted fit model.

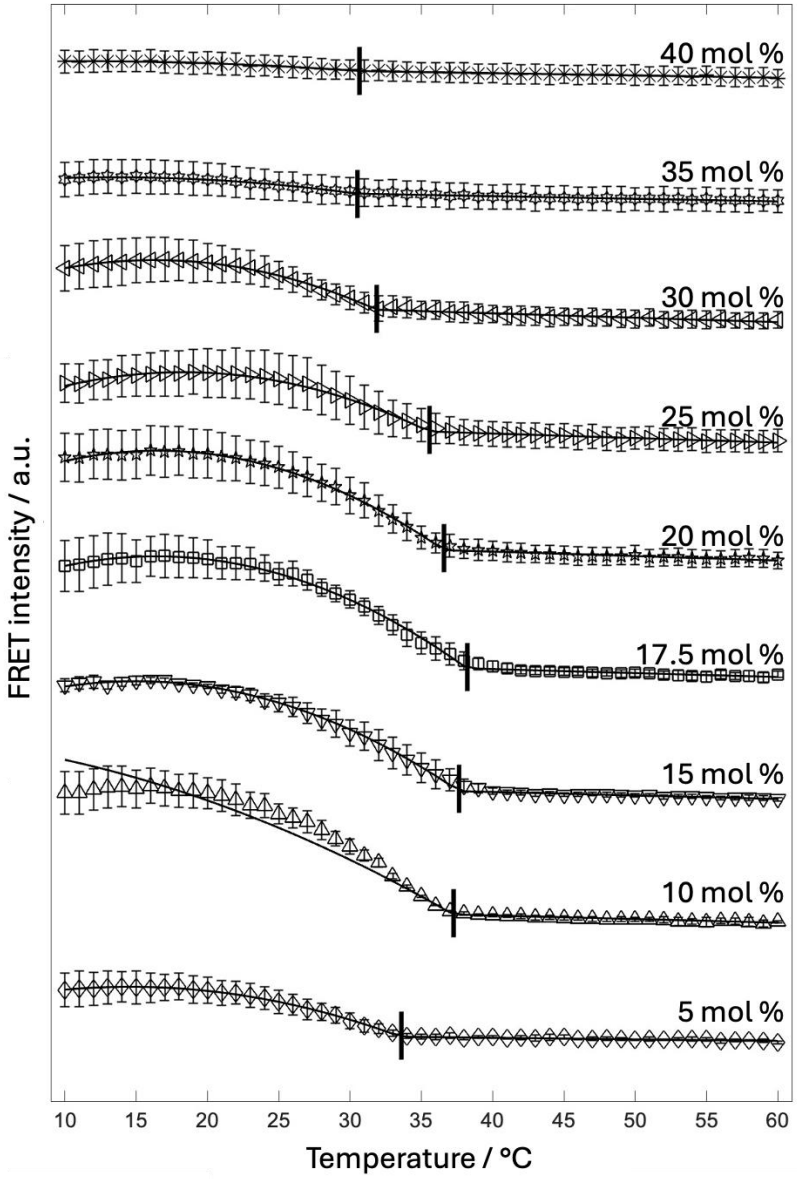


Figure 4.3) Model Fits for ternary DOPC/DPPC/Cholesterol system at a fixed 1:1 DPPC:DOPC ratio and varying cholesterol concentration. Each $F_{Ratio}(T)$ curve was fit with all three models and the best fit model was determined by χ^2_{red}ratio. The black vertical lines are the determined T_{misc} values.

4.5.3 Determining the T_{misc} using a single probe pair

Previous studies have only used one probe pair to determine the T_{misc} of a sample.[29, 141] In this method, we independently determined the T_{misc} values from each probe pair and compared them to the $F_{Ratio}(T)$ T_{misc}, using weighted sample replicates of DPPC/POPC/Chol (40/40/20mol%), and DPPC/DOPC/Chol (40/40/20mol%). In **Figure 4.4,** each row shows the FRET1 curve, FRET2 curve, and $F_{Ratio}(T)$ fit with all three models. The T_{misc} value from each is reported in **Appendix 4.6**. This method can be used to fit each replicate curve for FRET1, FRET2, and $F_{Ratio}(T)$.

4.6 Conclusion

FRET is a valuable tool for determining phase behavior in model membranes. However, there are few protocols for fitting SP-FRET data and mathematically determining the T_{misc}. Here, we present a user-friendly code that implements both previously established algorithms and novel methodologies to assess the phase behavior of a sample based on the χ^2_{red} metric. The code also reports the T_{misc}; however, this parameter is physically meaningful only when the system exhibits phase separation, despite it being reported in all cases. Within this method, we explored previously known samples such as 100% DOPC, DPPC/POPC/Chol (40/40/20mol%), and DPPC/DOPC/Chol (40/40/20mol%). For these samples, we demonstrated the sensitivity of this method and showed that it can resolve domain size, even in nanoscopically phase separated systems such as DPPC/POPC/Chol. Furthermore, we extended our study to see if this method can determine the phase boundary in the well-studied 1:1 + Cholesterol trajectory of DPPC/DOPC/Chol. The methodology was able to confirm that 35 mol% Chol is uniform, as previously determined by Mehta and Crumley et al. Methods for determining phase behavior in a mixture are crucial in phase behavior studies using SP-FRET.

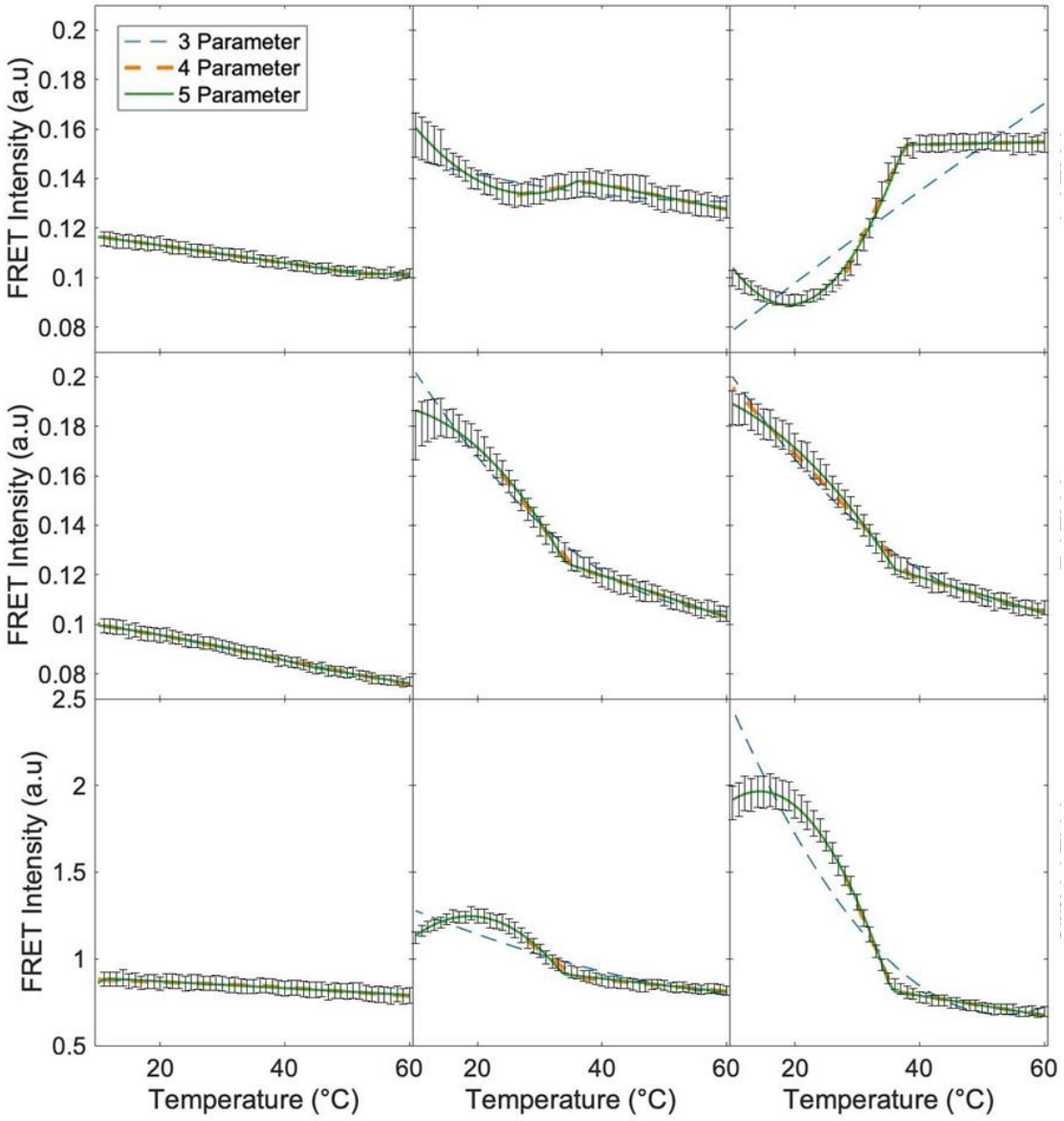


Figure 4.4) Weighted curves for 100% DOPC, DPPC/POPC/Chol (40/40/20mol%) and DPPC/DOPC/Chol (40/40/20mol%). Column (A) is 100% DOPC weighted curve for FRET 1 (row 1), FRET 2 (row 2) and FRET Ratio (row 3). Each curve is fit with the 3 (blue dash), 4 (orange dash), and 5 parameter (green solid) model. Column (B) is DPPC/POPC/Chol (40/40/20mol%) and column (C) is DPPC/DOPC/Chol (40/40/20mol%). The error bars are standard error of the mean. Each composition had 10 sample replicates.

CHAPTER FIVE

THE INFLUENCE OF MIXED CHAIN LIPIDS ON MEMBRANE PHASE BEHAVIOR AND NANODOMAIN FORMATION

A version of this chapter is being prepared for submission as a manuscript.

Emily H. Chaisson*, Deeksha Mehta, Averi M. Cooper, Maryam Ahmed, M. Neal Waxham and Frederick A. Heberle "The Influence of Mixed Chain Lipids on Membrane Phase Behavior and Nanodomain Formation " (*indicates authors contributed equally)

Detailed author contributions for this chapter are as follows:

1. Ternary phase diagrams determined from confocal microscopy of GUVs. D.M. was primarily responsible for MSPC/DOPC/Chol and 15:0-PC/DOPC/Chol; E.H.C. was primarily responsible for SMPC/DOPC/Chol; A.M.C. and M.A., undergraduate researchers working under the mentorship of D.M. and E.H.C., each contributed by examining approximately 10 compositions across the three phase diagrams.

2. Miscibility transition temperatures determined from confocal microscopy of GUVs. E.H.C. and D.M. performed the experiments; D.M. analyzed the data.

3. Nanoscopic phase behavior and miscibility transition temperatures from FRET experiments. E.H.C. and D.M. performed the experiments; E.H.C. analyzed the data.

4. Cryo-EM imaging. E.H.C. and D.M. prepared samples; M.N.W. cryo-preserved the samples, conducted the imaging, and processed the image data; E.H.C. analyzed the SMPC/DOPC/Chol and DPPC/DOPC/Chol samples; D.M. analyzed the MSPC/DOPC/Chol and 15:0-PC/DOPC/Chol samples.

5. Manuscript preparation. D.M., E.H.C., and F.A.H. wrote the first draft; D.M., E.H.C., M.N.W., and F.A.H. edited the manuscript.

5.1 Abstract

Membranes, predominantly composed of lipids, are a fundamental feature of all biological systems found in nature. In particular, the eukaryotic plasma membrane is asymmetric and chemically diverse. A subclass of lipids in eukaryotic membranes is those where the two acyl chains are different in structure, referred to as hybrid lipids. Previous studies have focused on the hybridization of the low-melting lipid. However, it has been shown that yeast enhances the biosynthesis of the hybridized high-melting lipids or ordered hybrid lipids (OHL) under stressful conditions. This increase in OHL synthesis was hypothesized to occur due to OHLs' ability to alter membrane properties. The phase behavior of these hybridized high-melting lipids has yet to be explored. Here, we investigate how chain mismatch and acyl-chain position on the glycerol backbone influence the phase behavior of ternary mixtures of cholesterol, DOPC, and either MSPC (14:0-18:0 PC) or SMPC (18:0-14:0 PC) as the high-melting lipid. To eliminate any effect of lipid-dependent melting point, we also included 15:0-PC, which has a T_M between the two hybridized lipids. Our confocal fluorescence microscopy data suggest that transposing the *sn*-1 and *sn*-2 chains of MSPC and SMPC results in dramatically different phase behavior. Specifically, liquid-ordered (Lo) + liquid-disordered (Ld) phase coexistence was observed over various compositions and temperatures in the MSPC/DOPC/Chol system, but not in the SMPC/DOPC/Chol system. We have recently shown that cryo-EM can directly image and distinguish between Lo and Ld phases at nanoscopic length scales based on the intrinsic differences in the thickness and electron density of the two phases. Here, we use cryo-EM along with FRET to investigate the presence of nanoscopic domains in SMPC/DOPC/Chol mixture. Our cryo-EM and FRET results show that SMPC/DOPC/Chol shows nanoscopic lateral heterogeneity at 22°C. We also compare our results to a mixture containing 15:0-PC as the high-T_M lipid with *sn*-1 and *sn*-2 chains of equal length. We saw that the phase behavior of 15:0-PC/DOPC/Chol is similar to that of MSPC/DOPC/Chol.

5.2 Introduction

It is now widely established that lateral heterogeneity is a fundamental defining property of eukaryotic cell membranes.[224, 225] Despite continued uncertainty regarding the structural and functional nature of the domains, their presence is well supported by experimental evidence.[226] Given the presence of hundreds of distinct lipid species in the plasma membrane, it is likely that specific lipids, based on their structural features, will exhibit preferential interactions with some lipids while interacting unfavorably with others.[227, 228] Such differential affinities contribute to lipid clustering and phase separation within the membrane.[229] Compartmentalization is a key feature of the plasma membrane, which is crucial for cells to perform specialized functions such as intercellular and intracellular signaling [46, 230] One such mechanism of compartmentalization is the formation of lipid rafts.[231] Raft formation is the result of unfavorable interactions between sphingolipids and phospholipids combined with favorable interactions between sphingolipids and cholesterol, leading to phase separation within the membranes.[232] Ordered raft domains contain more cholesterol due to the favorable interactions between cholesterol and saturated lipids, which are thicker and more rigid than those found in non-raft regions.[233, 234] These rafts organize membrane-resident proteins based on their affinity for either raft or non-raft domains, contributing to essential cellular processes such as protein trafficking, signaling, and pathogen-host interactions.[235, 236] Despite substantial biochemical and spectroscopic evidence supporting the existence of lipid rafts, their direct visualization remains challenging due to their small size and transient lifetimes, making them difficult to characterize experimentally.[226] Therefore, studies using simplified model membrane mixtures have been crucial in defining the physicochemical principles underlying raft formation.[36]

Ternary mixtures consisting of a high-T_M lipid, a low-T_M lipid, and cholesterol serve as well-established models for the outer leaflet of the plasma membrane.[32, 35] The compositional phase behavior of such three-component systems is broadly classified into type-I and type-II, based on the size and visibility of the coexisting domains. In mixtures where the low-T_M lipid contains unsaturation in both acyl chains, such as DOPC, micron-scale domain formation is observed at room temperature using confocal fluorescence

microscopy (CFM), indicative of type-II behavior.[116, 237] These mixtures typically exhibit Ld + Lo or Ld+ Lβ + Lo phase coexistence.[36] In contrast, most biologically relevant glycerophospholipids, such as POPC, contain a saturated *sn*-1 chain and a cis-unsaturated *sn*-2 chain.[238] Substituting DOPC with POPC in otherwise identical ternary systems results in GUVs that appear optically uniform.[239] Nonetheless, nanoscale liquid-liquid phase separation persists and can be detected using techniques with sub-diffraction resolution, such as Förster resonance energy transfer (FRET), electron spin resonance (ESR), small-angle neutron scattering (SANS), and cryogenic electron microscopy (cryo-EM).[240 148, 241-243] This nanoscale domain behavior is characteristic of type-I mixtures.[55 116]

This distinction between type-I and type-II phase behavior highlights the sensitivity of domain formation to lipid structure. Previous studies have extensively characterized specific ternary systems, such as DPPC/DOPC/Chol, DSPC/DOPC/Chol, and DMPC/DOPC/Chol across a wide temperature range of 15–45 °C.[239] Notably, DPPC/DOPC/Chol and DSPC/DOPC/Chol display type-II behavior, with macroscopic Lo + Ld phase separation observed across multiple lipid ratios.[33, 35, 237] In contrast, type-I mixtures like DPPC/POPC/Chol, DPPC/SOPC/Chol, DPPC/DLPC/Chol exhibit nanoscopic heterogeneity that cannot be resolved by phase-preferring fluorescent probes, highlighting the challenge in visualizing domains.[237] This concept of type-I and type-II promotion has traditionally been considered in the context of the low-melting lipid within the ternary mixture. Similarly, changes in the acyl chain length of the high-T_M lipid can also affect phase behavior.[33, 35, 239] For example, increasing chain length from DMPC to 15:0-PC alters the mixture's behavior at 22 °C with 20% Chol and changes the system from type-I to type-II.[33] However, hybridization of the low-T_M lipid has resulted in nanoscopic rather than macroscopic heterogeneity.[52] In this study, we investigated ternary mixtures where the low-melting lipid DOPC, which is typically associated with type-II phase behavior, was kept constant. Simultaneously, the high-melting component was systematically varied by utilizing different ordered hybrid lipids (OHLs).

While most biological lipids typically have acyl chains of similar lengths[244], there exists a lesser-studied class of lipids in which the two chains differ in length. In some

cases, this chain length difference can be extreme, like sphingomyelin, where the shortest possible chain can be two carbons and the longest possible chain can be 28 carbons.[245, 246] In some yeast systems, these mixed-chain lipids are found in high concentrations and are upregulated under stress, suggesting a biological role.[247] Furthermore, this chain mismatch is known to alter the melting point compared to its chain symmetric counterparts, potentially leading to differences in phase behavior.[191]

While previous studies have explored the effects of hybridizing the low-T_M lipid (i.e., DOPC with POPC)[35], little is known about hybridizing the high- T_M lipid in ternary mixtures. Nevertheless, single-component systems simply transposing the 14:0 and 18:0 chains in MSPC to SMPC, leads to significant differences in physical behavior, such as interdigitation[248] and bending moduli.[87] These results highlight the importance of understanding chain mismatch and its effects on biomembranes properties, particularly in biologically relevant model membranes.

Here, we investigated the effect of substituting the high-T_M lipid with an OHL that contains one acyl chain from a high-T_M lipid that is known to form a type-I mixture at 22°C with DOPC and Chol and another from a lipid that forms type-II mixtures with DOPC and Chol. We focused on two OHLs -SMPC and MSPC- differing only in the position of the two acyl chains on the glycerol backbone. To assess whether differences in phase behavior are due to melting point variations, we also included a chain-symmetric lipid with an intermediate T_m. Our study explores how structural differences in saturated OHL influence phase behavior in ternary systems, using di15:0 PC as a reference point.

5.2 Materials and Methods

5.2.1 Materials

Phospholipids 1,2-dioleoyl-sn-glycero-3-phosphocholine (DOPC), 1,2-dimyristoyl-sn-glycero-3-phosphocholine (DMPC), 1,2-dipentadecanoyl-sn-glycero-3-phosphocholine (15:0-PC), 1,2-dipalmitoyl-sn-glycero-3-phosphocholine (DPPC), 1,2-distearoyl-sn-glycero-3-phosphocholine (DSPC), 1-myristoyl-2-stearoyl-sn-glycero-3-phosphocholine (MSPC), and 1-stearoyl-2-myristoyl-sn-glycero-3-phosphocholine (SMPC) were purchased from Avanti Polar Lipids (Alabaster, AL). Cholesterol was purchased from Nu-Chek Prep (Elysian, MN). Fluorescent dyes 1,2-dioleoyl-sn-glycero-

3-phosphoethanolamine-N-(lissamine rhodamine B sulfonyl) (ammonium salt) (LRPE), 1,2-distearoyl-sn-glycero-3-phosphoethanolamine-N-(7-nitro-2-1,3-benzoxadiazol-4-yl) (ammonium salt) (NBD-DSPE, NBD), and 1-palmitoyl-2-(dipyrromethene boron difluoride)undecanoyl-sn-glycero-3-phosphocholine (TopFluor-PC, TFPC) were purchased from Avanti Polar Lipids. The fluorescent dye 1,1′-dioctadecyl-3,3,3′,3′-tetramethylindodicarbocyanine, 4-chlorobenzenesulfonate salt (DiD) was purchased from ThermoFisher Scientific (Eugene, OR) and naphtho[2,3-*a*]pyrene (naphthopyrene, Nap) was purchased from TCI America (Portland, OR). All lipids and dyes were suspended in HPLC-grade chloroform and stored at -20°C until use. The concentration of the phospholipid stocks was determined using a colorimetric inorganic phosphate assay[249], and the concentration of the cholesterol stock was determined gravimetrically. Dye concentrations were determined from absorbance measurements using the following extinction coefficients in units of $M^{-1}cm^{-1}$: 95,000 (LRPE); 23,800 (Nap); 96,904 (TFPC); and 249,000 (DiD). Ultrapure water was obtained from a Milli-Q IC 7000 purification system (Millipore Sigma, Burlington, MA).

5.2.2 Confocal Fluorescence Microscopy

Giant unilamellar vesicles (GUVs) were prepared using a modified electroformation procedure.[133] Briefly, a mixture of lipids and probes was prepared in the desired ratio by dispensing stock solutions into a 13 x 100 mm glass culture tube containing 100 μL of chloroform. The solution was then spread onto two indium tin oxide (ITO)-coated glass slides on a hot plate set at 55 °C (Delta Technologies, Stillwater, MN) and placed under a vacuum for 2 h. A chamber was formed from the two slides using an O-ring spacer filled with 600 μL of 100 mM sucrose solution and then placed into an aluminum holder heated to 55 °C. GUVs were formed by applying a 2.0 V peak-to-peak, 10 Hz AC waveform to the chamber for 2 h while the holder was maintained at 55 °C, followed by cooling to 22 °C at a rate of 2.66 °C per hour. GUVs were harvested from the chamber and stored in a plastic microfuge tube.

Prior to imaging, 50 μL of freshly harvested GUVs in 100 mM sucrose was suspended in 1.5 mL of 100 mM glucose in a glass culture tube. After ~ 30 min, a 5 μL

aliquot was taken from the bottom of the tube and sandwiched between a glass slide and a cover slip for microscopy observations. Imaging was performed with a Nikon C2+ point scanning system attached to a Nikon Eclipse Ti2-E microscope (Nikon Instruments, Melville, NY) equipped with a Plan Apo Lambda 60×/1.4 NA oil immersion objective. An objective cooling collar maintained a sample temperature of 22°C (Bioptechs, Butler, PA). NBD-DSPE and LRPE were excited with 488 nm and 561 nm laser lines, respectively, with quarter-wave plates (ThorLabs, Newton, NJ) inserted into the excitation path to correct for polarization artifacts.

To determine the miscibility transition temperature (T_{misc}) of GUVs composed of ternary mixtures, the sample temperature was controlled using a VaHeat heating stage (Interherence, Erlangen, Germany), with the objective cooling collar used to access temperatures below 22 °C for some mixtures. For each composition, a field of view with at least 10 phase-separated vesicles was selected. The temperature was then incrementally increased by 1°C and, after waiting 30 s for equilibration, the number of uniform and phase-separated vesicles was counted. This process was repeated until all vesicles appeared uniform. The fraction of phase-separated vesicles vs. temperature was fit to a sigmodal function to determine T_{misc} as described in the Supporting Information.

5.2.3 Fluorescence Spectroscopy

Vesicles of low average lamellarity (LLVs) for FRET measurements were prepared using the method of rapid solvent exchange (RSE) as previously described.[141] Stock solutions of lipids and probes in the desired ratios were dispensed into 13 x 100 mm glass screw-cap culture tubes containing 25 μL of chloroform. After adding 500 μL of ultrapure water, the tube was immediately mounted on the RSE device and exposed to vacuum while undergoing vigorous vortexing. During RSE, a slow leak of Ar was introduced into the tube to facilitate chloroform removal. After 1.5 min under vacuum, the sample was vented to Ar and transferred to a plastic centrifuge tube.

FRET was measured using a HORIBA FluoroLog 3 spectrophotometer (HORIBA USA, Irvine, CA) equipped with a temperature-controlled cuvette holder (Quantum Northwest, Liberty Lake, WA). Samples contained three probes comprising two

donor/acceptor FRET pairs: Nap/DiD and TFPC/DiD. Probe/lipid ratios were 1/200 for Nap, 1/1500 for TFPC, and 1/1000 for DiD. For fluorescence measurements, a 0.100 mL aliquot of a 0.625 mM (total lipid) sample was added to 1.90 mL of water in a fluorescence cuvette while stirring at 1000 rpm using a flea stir bar. Fluorescence intensity was measured in five channels (excitation/emission wavelengths in nm): Nap direct signal (427/545); Nap/DiD FRET (427/664); TFPC direct signal (499/551); TFPC/DiD FRET (499/664); and DiD direct signal (646/664). Excitation and emission slit widths were 2-3 nm, and the signal integration time was 0.1 s. Data were collected from 60 to 10°C in -1°C decrements with an equilibration time of 2 min at each temperature. The number of sample replicates was 10 for SMPC/DOPC/Chol, DPPC/DOPC/Chol, and DOPC, and 3 for MSPC/DOPC/Chol, 15:0-PC/DOPC/Chol, and DMPC/DOPC/Chol.

Sensitized acceptor emission was calculated from the intensity measured in the FRET channel after correcting for direct fluorescence contributions from donor and acceptor, as described previously.[241] Following Mehta et al.[8], T_{misc} was determined by fitting the ratio of the FRET signals from the two probe pairs (i.e., TFPC/DiD FRET divided by Nap/TFPC FRET) to a phenomenological piecewise model consisting of a linear function at $T > T_{misc}$ and a quadratic function at $T < T_{misc}$. Each dataset was also fit to a simpler quadratic function over the entire temperature range to serve as a null model (i.e., the absence of a miscibility transition).

5.2.4 Cryo-EM Imaging

Large unilamellar vesicles (LUVs) were prepared as previously described.[250] Briefly, aqueous lipid dispersions with a total lipid concentration of 3 mg/mL were made by first mixing the required volumes of lipid stocks in chloroform using a glass Hamilton syringe. The solvent was then evaporated using an inert gas stream, and the sample was kept under vacuum overnight. Dried lipid films were hydrated with ultrapure water preheated to 55 °C and incubated for ~1 h with vortex mixing every 15 min, followed by five freeze/thaw cycles between liquid nitrogen and a 55 °C water bath. This suspension was then extruded 31 times through a 100 nm polycarbonate filter using a handheld mini-

extruder (Avanti Polar Lipids) maintained at 55 °C. The size and polydispersity of the LUVs were determined using dynamic light scattering (LiteSizer 100, Anton Paar U.S.A., Vernon Hills, IL) immediately after preparation and again before cryo-preservation, which was typically performed 1 day after LUV preparation.

Cryo-preservation was performed by adding 4 μL of LUVs to a Quantifoil 2/2 carbon-coated 200 mesh copper grid (Electron Microscopy Sciences, Hatfield, PA) that was glow-discharged for 30 sec at 20 mA in a Pelco Easi-Glow discharge device (Ted Pella, Inc., Redding, CA). This was followed by manual blotting at room temperature, in which the grids were plunged into liquid ethane cooled with liquid nitrogen. The cryo-preserved grids were subsequently stored in liquid nitrogen.

Cryo-EM image collection was performed at ~ 2 μm under focus on a Titan Krios operated at 300 keV equipped with a Gatan K2 Summit direct electron detector operated in counting mode. Data collection was conducted in a semi-automated fashion using Serial EM software operated in low-dose mode. Briefly, areas of interest were identified visually, and 8×8 montages were collected at low magnification (2400×) at various positions across the grid, with desired areas marked for automated data collection. Data was collected at 2.7 Å/pixel. Movies of 30 dose-fractionated frames were collected at each target site with the total electron dose being kept to < 20 $e^{-}/Å^2$ to avoid beam-induced damage.[251] Dose-fractionated movies were drift-corrected with MotionCor2. Defocus and astigmatism were assessed with CTFFind4.[252] Finally, a high-pass filter was applied along with phase flipping using the 'mtffilter' and 'ctfphaseflip' routines in the IMOD v4.11 software package.

Projection images of vesicles were analyzed in Wolfram Mathematica v. 13 (Wolfram Research Inc., Champaign, IL) as previously described[243] to obtain spatially resolved intensity profiles (IPs) in the direction normal to the bilayer. Briefly, vesicle contours (i.e., the set of points corresponding to the midplane of the projected bilayer as defined by a relatively bright central peak) were first generated using a neural network-based algorithm (MEMNET) that is part of the TARDIS software package.[253] The MEMNET contour was resampled at arc length intervals of ~ 5 nm, resulting in a

polygonal representation of the 2D contour. For each polygon face, all pixels within a 5×20 nm rectangular region of interest centered at the face were selected, and their intensities binned at 1 Å intervals in the long dimension (i.e., normal to the face) and subsequently averaged in the short dimension to produce a local segment IP. To determine the phase state of each bilayer segment, we subjected the local IP vectors to 2-means clustering using Mathematica's FindClusters algorithm with the distance function set to Euclidean and all other parameters set to their default values. We also calculated the local bilayer thickness, D_{TT}, as the distance between the two minima of the local IP. Two methods were used to locate the minima: (1) a 'model-free' method, in which a local 5-point Gaussian smoothing was first performed, and the distance between the two absolute minimum intensity values on either side of the central peak was determined; (2) a 'model-fit' method that fits the profile as a sum of four Gaussians and a quadratic background, with the troughs corresponding to the two absolute minimum intensity values on either side of the central peak. The two methods typically agree to within 1 Å, and the values we report are the average of the two measurements.

5.3 Results and Discussion

Our primary goal was to determine how high-melting saturated lipids with mismatched acyl chains (i.e., having different length) influence the phase behavior of ternary mixtures that are models for the composition of the eukaryotic plasma membrane outer leaflet. We examined two such mismatched lipids, MSPC and SMPC. Each of these lipids possesses fully saturated 14-carbon and 18-carbon chains, but the position of the chains on the glycerol backbone is different as shown in **Figure 5.1**: the shorter chain is in the *sn*-1 position for MSPC and in the *sn*-2 position for SMPC. The natural tilt of the glycerol backbone results in a vertical offset of ~ 0.5 Å between the *sn*-1 and *sn*-2 chains of fluid-phase PC bilayers, with the *sn*-2 chain residing at the higher position[87]; this backbone tilt slightly lessens the effective chain length mismatch of MSPC and slightly enhances it for

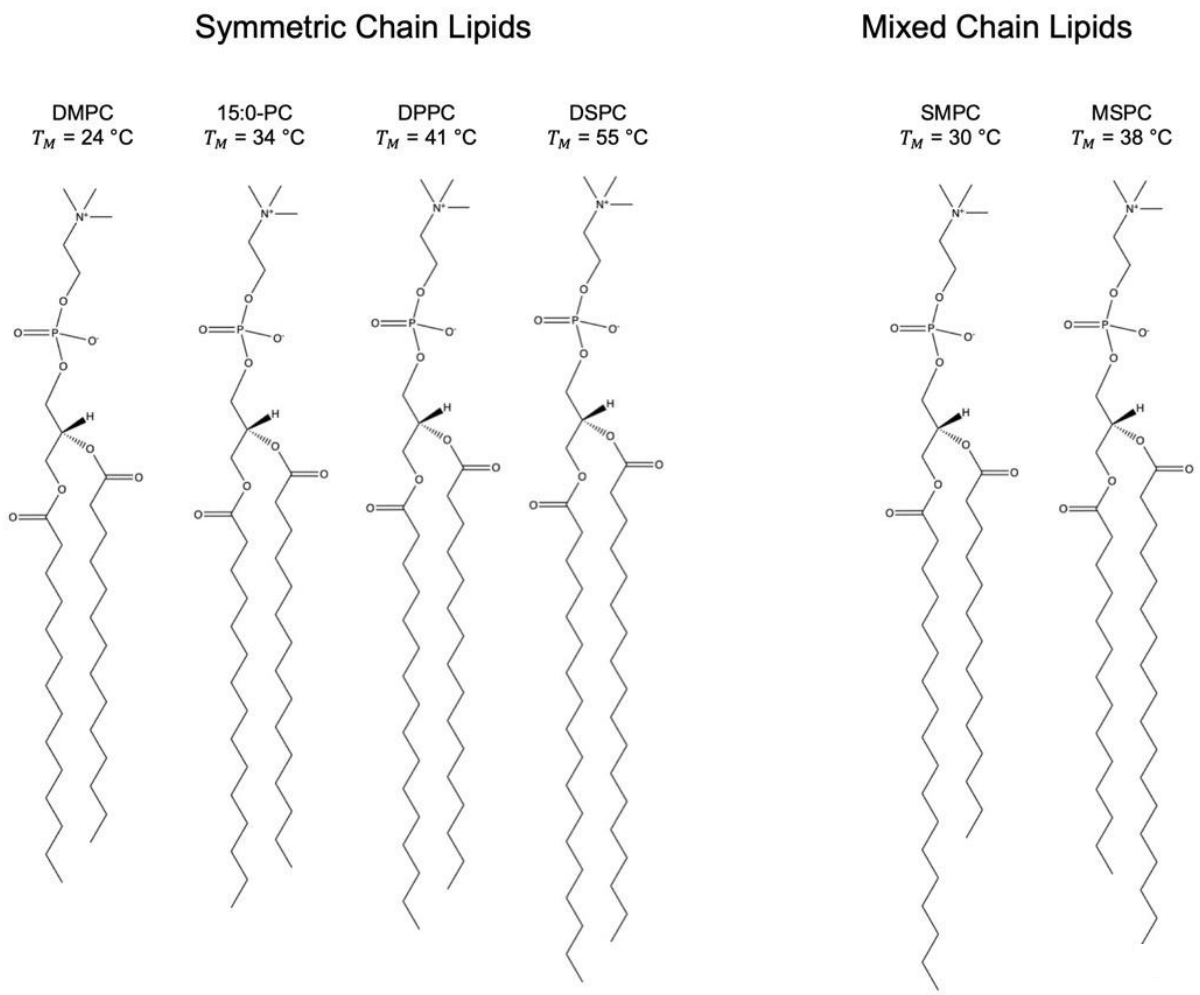


Figure 5.1) High-T_M lipids in this study. From left to right: DMPC (14:0-14:0 PC); 15:0-PC (15:0-15:0PC); DPPC (16:0-16:0PC); DSPC (18:0-18:0PC); SMPC (18:0-14:0PC); and MSPC (14:0-18:0 PC).

SMPC. In addition to the high-T_M lipid, each of the studied mixtures included cholesterol and the low-melting lipid DOPC. As a baseline for comparison, we also examined mixtures that contained 15:0-PC as the high-T_M species, as this lipid has two identical chains and a main chain transition temperature between that of MSPC and SMPC.

5.3.1 Macroscopic phase behavior from fluorescence imaging

We used confocal fluorescence microscopy (CFM) to examine the macroscopic phase behavior of GUVs composed of ternary mixtures of cholesterol, the low-T_M lipid DOPC, and a high-T_M lipid: MSPC, SMPC, or 15:0-PC. **Figure 5.2** shows confocal slices near the GUV cap for representative GUVs composed of a 1:1 ratio of MSPC:DOPC (top row), 15:0-PC: DOPC (middle row), and SMPC: DOPC (bottom row) with varying cholesterol concentration as indicated at 22°C. In the mixtures containing MSPC (top row) or 15:0-PC (middle row), Ld+Lβ coexistence was observed at low cholesterol concentrations (≤ 10 mol%) as indicated by the irregularly shaped, dark domains with rigid boundaries. At 20 mol% cholesterol, the boundaries appear to be smoother, and domains showed an increased tendency for rounded shapes, behaviors that are consistent with coexisting liquids (i.e., Ld+Lo). At 40 mol% cholesterol, uniform mixing was observed for both compositions. In contrast to the behavior for MSPC and 15:0-PC, mixtures containing SMPC (**Figure 5.2, bottom row**) showed no evidence of phase separation except at the lowest cholesterol concentration of 5 mol%, where GUVs had a distinctive patchy appearance.

Figure 5.3 summarizes the macroscopic phase behavior of MSPC/DOPC/Chol, 15:0-PC/DOPC/Chol, and SMPC/DOPC/Chol as assessed from GUVs. The diagrams for MSPC/DOPC/Chol and 15:0-PC/DOPC/Chol **(Figure 5.3a and 5.3b, respectively**) are similar and broadly consistent with other type-II mixtures[33, 35, 237], revealing regions of coexisting Ld+Lβ (blue triangles) and Ld+Lo (green circles) at 22°C. Although we did not observe conclusive visual evidence of Ld+Lβ+Lo coexistence, we can infer from the Gibbs phase rule that a three-phase coexistence region must be present between the Ld+Lβ and Ld+Lo regions due to the absence of an intervening single-phase region. A

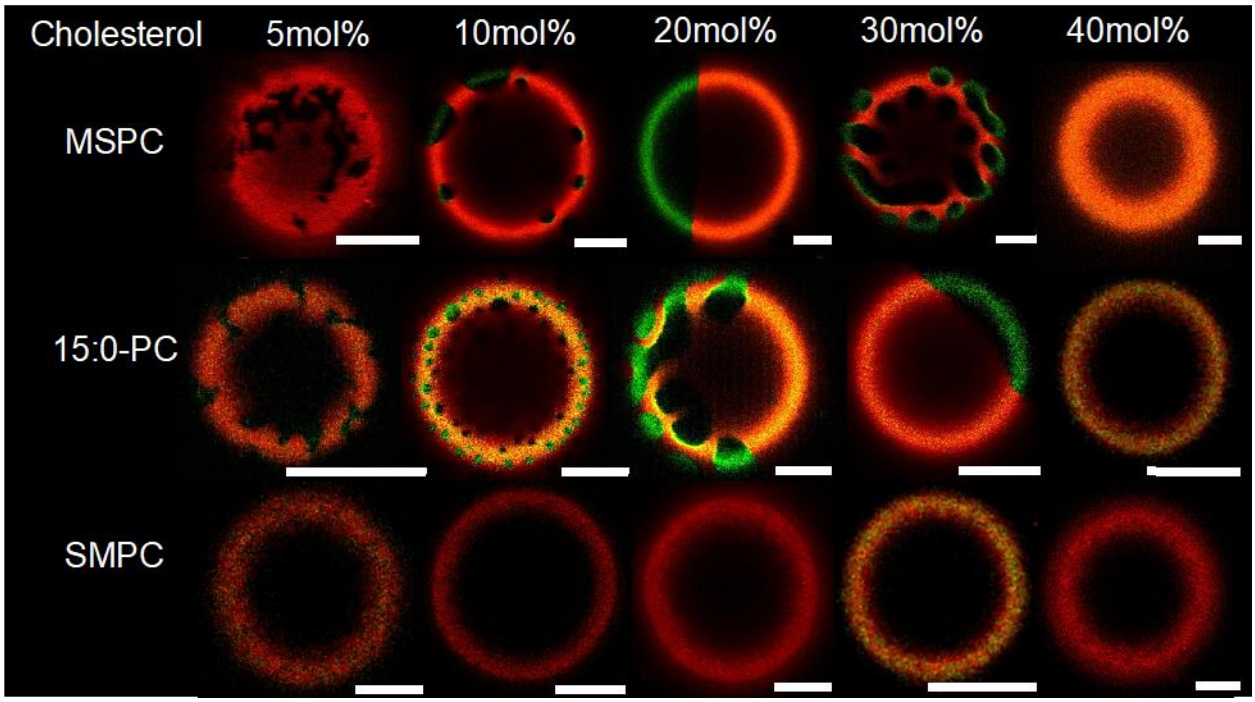


Figure 5.2) Confocal fluorescence images of GUVs at 22°C. Shown are slices near the GUV cap for three-component mixtures containing 1:1 high-T_M/DOPC with increasing Chol mol% and different high-T_M lipid as indicated: MSPC (top row); 15:0-PC (middle row); and SMPC (bottom row). GUVs were labeled with fluorescent dyes LRPE (red) and NBD (green). Each image shows the composite of the red and green channels. Scale bar is 5 μm.

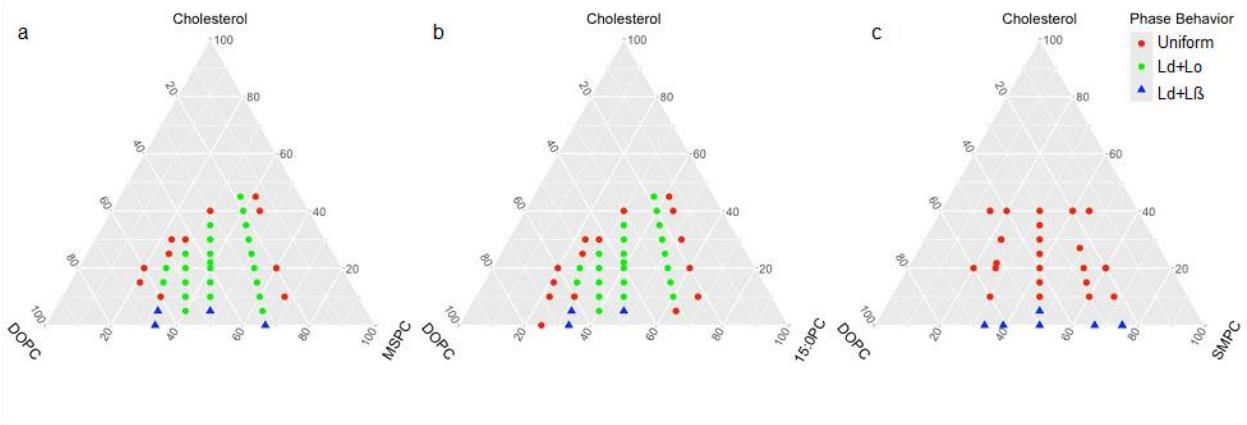


Figure 5.3) Phase behavior of GUVs at 22°C. Shown are ternary plots of GUV phase behavior for: MSPC/DOPC/Chol (a); 15:0-PC/DOPC/Chol (b); and SMPC/DOPC/Chol (c). Each point in the diagram shows the predominant phase behavior at a specific composition: blue triangles indicate Ld+Lß phase coexistence, green circles indicate Ld+Lo phase coexistence, red circles indicate uniform mixing, and black asterisks indicate compositions that showed approximately equal populations of phase-separated and uniformly mixed vesicles.

qualitatively different diagram was found for SMPC/DOPC/Chol (**Figure 5.3c**), which shows only a narrow region of Ld+Lβ below 5 mol% cholesterol and no evidence of Ld+Lo coexistence, consistent with type-I behavior at 22°C. These results highlight the substantial impact of acyl chain positioning within the high-T_M lipid on the macroscopic phase behavior of ternary mixtures.

5.3.2 Miscibility transition temperature from fluorescence imaging

We next determined the T_{misc} using CFM by controlling the temperature on the substrate as described in Section 5.2.2. We started at 17°C, where all systems were phase separated, and we continued the experiment until the sample exhibited uniform behavior. The temperature was increased in 1 °C increments with a 30 sec equilibration time, and three sample replicates were performed for each system. We counted the number of phase-separated vesicles at each temperature reading, as shown in t**Appendix 5.1)**. We then fit the data to a sigmoidal function (**Appendix 5.2**) as shown in **Figure 5.4** to calculate T_{misc}.

5.3.3 Nanoscopic phase behavior from cryo-EM imaging

It is well established that some type-I mixtures exhibit nanoscopic lateral heterogeneity at physiologically relevant cholesterol concentrations.[29] Although these heterogeneities are smaller than the resolution limit of conventional optical microscopy (~ 200 nm), their presence can often be inferred from spectroscopic and scattering experiments. In principle, nanoscopic domains can be directly visualized using cryo-EM.[37, 254] Unlike fluorescence microscopy, which requires strong partitioning of a probe molecule between the coexisting phases to distinguish them, the analogous contrast in cryo-EM images arises from intrinsic differences in the bilayer thickness and electron density of ordered and disordered phases.

We used cryo-EM to image LUVs at a composition, high-T_M lipid/DOPC/Chol 40/40/20 mol%, that exhibits Ld+Lo phase separation in type-II mixtures.[33] Representative images are shown in **Figure 5.5,** and full field of view images are shown in (**Appendix 5.2**). Consistent with the macroscopic behavior in GUVs, LUVs in which the high-T_M lipid

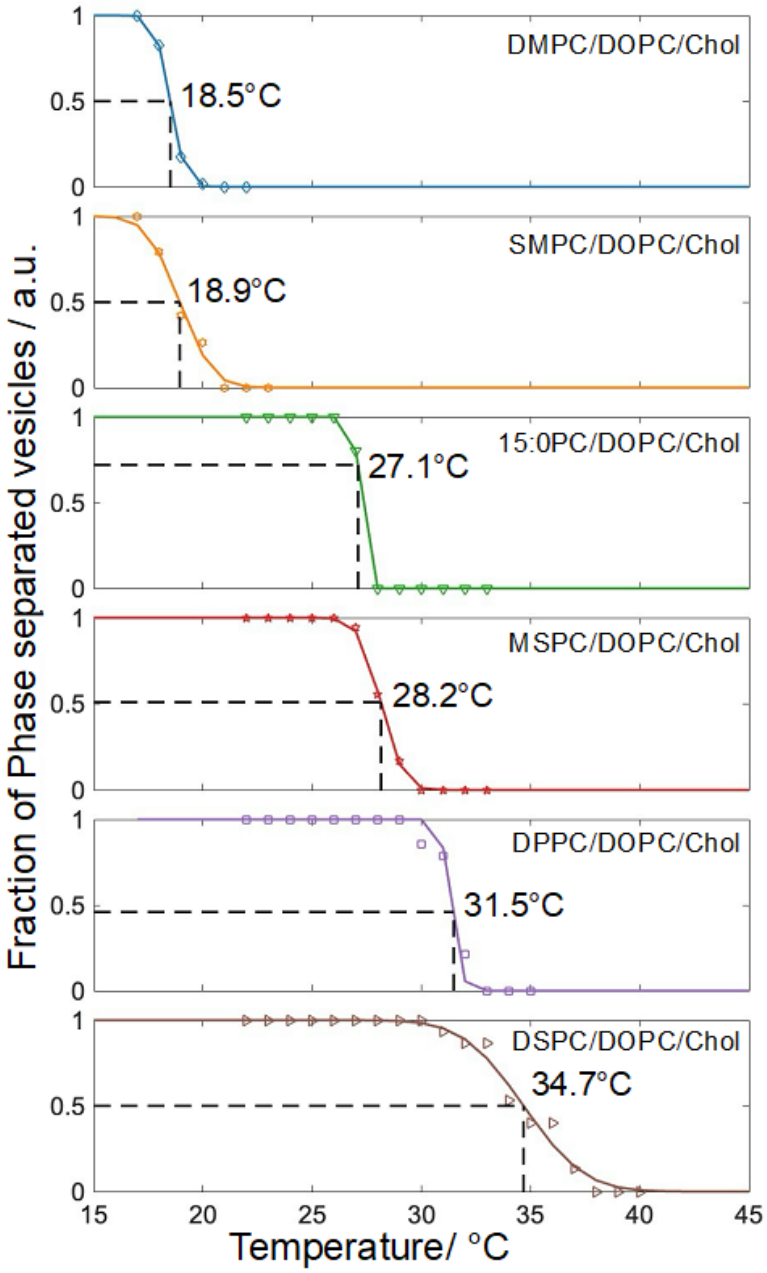


Figure 5.4) Representative sigmoidal fits for ternary mixtures used to determine T_{misc} from CFM data. Each plot displays the fraction of phase-separated vesicles as a function of temperature, fitted with a sigmoidal curve to extract T_{misc}. Shown are data from one of the three experimental replicates.

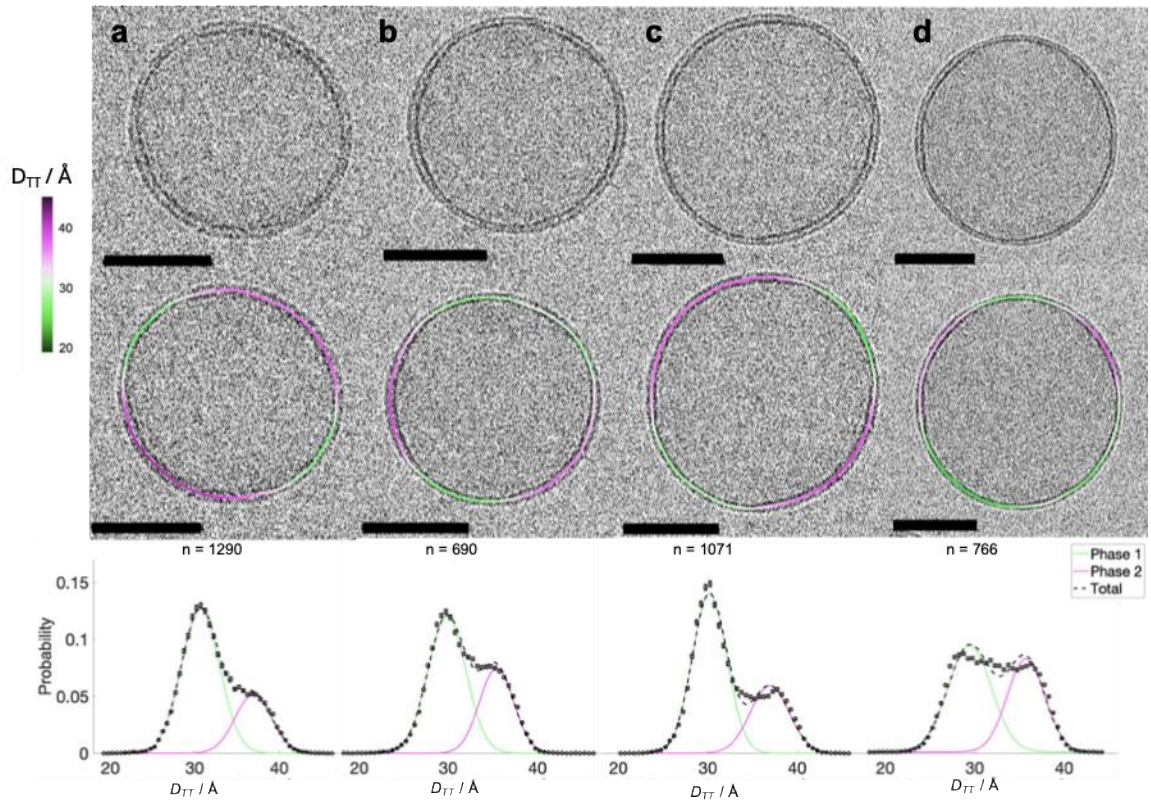


Figure 5.5) Cryo-EM images of ternary LUVs. All compositions are 40/40/20 mol%: DPPC/DOPC/Chol (a); MSPC/DOPC/Chol (b); 15:0-PC/DOPC/Chol (c); and SMPC/DOPC/Chol (d). Shown is a representative vesicle for each composition without (top row) and with (middle row) an overlay of the local bilayer thickness, D_{TT}, as indicated by the color scale bar. Black image scale bars are 50 nm. Plotted in the bottom row are histograms of local bilayer thickness calculated as described in Methods, with the total number of vesicles contributing to each histogram denoted by *n*.

was DPPC, MSPC, or 15:0-PC **(Figure 5.5a**, **5.5b**, and **5.5c**, respectively) showed two coexisting environments with average thicknesses of ~ 31 Å and 37 Å. These values are similar to the thicknesses of Ld and Lo phases measured with X-ray and neutron scattering.[233, 255] Remarkably, similar thickness variability was also observed for LUVs that contained SMPC (**Figure 5.5c**) despite the uniform appearance of GUVs with this composition **(Figure 5.2**).

Further insight can be gained from histograms of the local bilayer thickness obtained from the full population of vesicles (**Figure 5.6**, bottom row). For each of the four mixtures, these histograms show a bimodal thickness distribution consistent with the visual appearance of the LUVs. Fitting the distributions as a sum of two gaussians yields values for the mean thickness and area fraction of each phase as shown in **Table 5.1**. Notably, for all mixtures except SMPC/DOPC/Chol, the probability density peak is larger for the thinner Ld phase compared to the thicker Lo phase. In contrast, SMPC/DOPC/Chol exhibits a smaller Ld peak and a greater probability of thicknesses between that of pure Ld or Lo. Intermediate thickness values correspond to domain boundaries where density from both phases contributes to the projected image. Because the frequency of boundary segments should increase with increasing domain perimeter in the vesicle, we speculate that SMPC (and to a lesser extent, MSPC) promotes smaller domains with a concomitant increase in domain interface..

5.3.4. Miscibility transition temperature from FRET spectroscopy

To more fully characterize the phase behavior of the 40/40/20 mol% samples, we used FRET to determine their miscibility transition temperatures, T_{misc}. This technique is sensitive to changes in the spatial organization of donor and acceptor lipid probes that occur when the bilayer undergoes a miscibility transition. Provided these probes partition non-uniformly between the coexisting phases, the FRET signal changes abruptly upon formation of domains whose size exceeds the Förster distance, R_0, of the donor-acceptor pair. As R_0 is typically in the range of 2-6 nm, FRET can inform on nanoscopic phase separation that cannot be detected by optical microscopy. Our experiments utilized three

Table 5.1) Analysis of cryo-EM images of LUVs

System	D_{TT} / Å		Phase 1 area fraction	Chi square
(40/40/20 mol%)	Phase 1	Phase 2		
DPPC/DOPC/Chol	37.0 ± 2.2	30.7 ± 2.3	0.28	2.77
MSPC/DOPC/Chol	36.9 ± 2.2	30.2 ± 1.9	0.36	10.03
15:0-PC/DOPC/Chol	35.4 ± 1.9	29.9 ± 2.6	0.36	6.82
SMPC/DOPC/Chol	35.7 ± 2.1	29.4 ± 2.4	0.43	25.43

fluorescent lipid probes comprising two donor-acceptor pairs: (1) Nap donor to DiD acceptor; and (2) TFPC donor to DiD acceptor. Co-localization of TFPC and DiD within the Ld phase results in enhanced FRET efficiency at temperatures below T_{misc}. However, because Nap preferentially partitions to the Lo phase, FRET between Nap and DiD decreases upon Ld+Lo phase separation (**Appendix 5.3**). The use of two probe pairs with complementary partitioning behaviors in the same sample allows us to distinguish between changes in probe spatial organization due to phase separation and other, confounding factors that can also influence FRET efficiency, such as temperature-dependent variation in molecular packing density that would be expected to change the two FRET signals in a similar way. For quantitative analysis, we fit the ratio of the two FRET signals (i.e., TFPC:DiD / Nap:DiD) to a phenomenological piecewise model that captures the different behavior of the regimes above and below T_{misc}. We find that taking the ratio of the FRET signals reduces noise and provides a more robust determination of T_{misc}.**Figure 5.6** plots the FRET ratio for the various mixtures as a function of temperature. We included two additional symmetric high-T_M lipids, DMPC and DSPC, as well as a single-component control sample, DOPC. As expected, the FRET ratio for DOPC is featureless, consistent with the absence of a phase transition in the temperature range of 10-60 °C. In contrast, each of the other mixtures shows a more complicated behavior as temperature is lowered from 60°C; for these datasets, the best fit curve corresponding to the piecewise model is shownas a solid line, and the best fit . T_{misc} value is indicated by a short vertical bar. In every case, a flat regime at high temperature (where the bilayer is in a uniformly mixed, Ld phase) is interrupted by a relatively abrupt increase in signal that marks the formation of Lo domains at T_{misc}. For the mixtures with the highest miscibility transition temperatures, the signal plateaus and eventually decreases as temperature is quenched deeper into the Ld+Lo region.

5.3.4. Nanoscopic T_{misc} is higher than macroscopic T_{misc}

Not all systems require a transitional state from uniformity to microdomains, however a transitional state of nanodomains is highly likely.[30] Therefore, to further investigate the miscibility behavior we examined the T_{misc} of systems with a 40/40/20 mol% ratio of high-T_M /low-T_M /Chol. Each system was fitted with a uniform or phase-

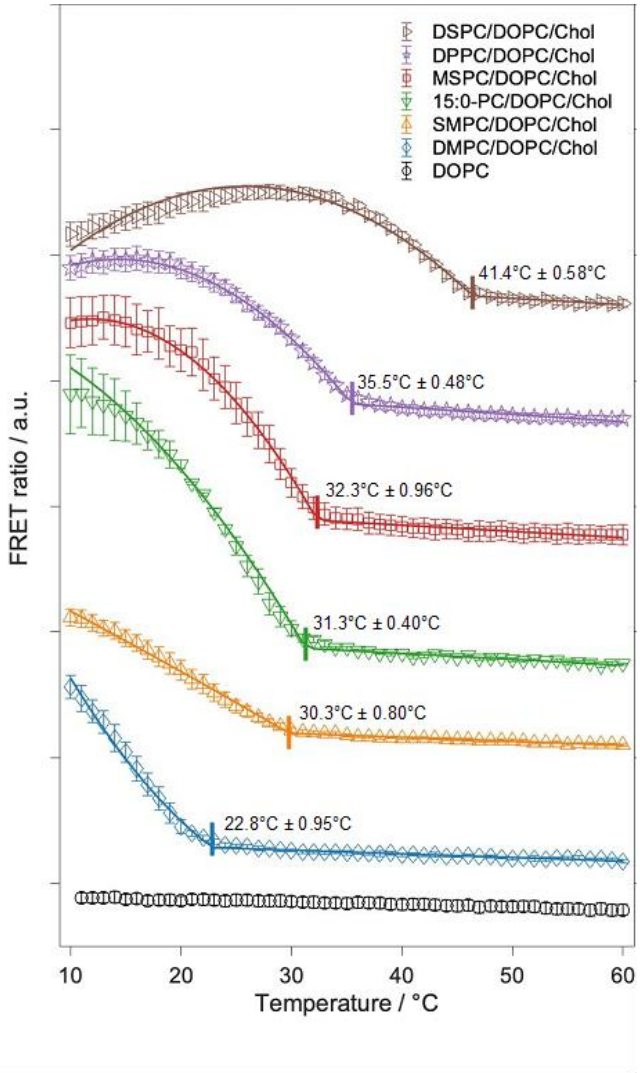


Figure 5.6) Average FRET ratio data for DOPC and ternary mixtures with model fits. (a) FRET ratio vs temperatures for DOPC (black circles) and high-T_M/DOPC/Chol 40/40/20 mol% for the high- T_M lipids: DMPC (blue diamonds), SMPC (orange triangles), 15:0-PC (green upside-down triangles), MSPC (red squares), DPPC (purple stars) and DSPC (brown right-pointing triangles). The solid lines represent the best fit to the uniform model for DOPC and the phase-separated model for ternary mixtures as described in Methods. Vertical lines indicate the best-fit value of T_{misc} determined from the model fits. Error bars are standard deviations determined from 10 sample replicates for DOPC, SMPC/DOPC/Chol, and DPPC/DOPC/Chol and 3 sample replicates for all other compositions.

separated model as described earlier. Within all systems except DOPC, the phase-separated model was a better fit, as shown in **(Appendix 5.5).** The T_{misc} of each of the ternary mixtures follows the same trend as when calculated using CFM (**Figure 5.7**).

Together, the CFM and FRET results reveal a clear distinction between micro- and nanodomain miscibility behavior. Since CFM cannot resolve nanodomains due to the diffraction limit of light, it captures transitions associated with larger microdomains, resulting in lower apparent T_{misc} values. In contrast, FRET is sensitive to nanoscopic organization and consistently reported higher T_{misc} values across all five ternary mixtures (**Figure 5.7**). The discrepancy between the two techniques was especially pronounced in the SMPC/DOPC/Chol system, where T_{misc} values differed by nearly 12 °C.

5.4. Summary and Conclusion

We investigated the influence of backbone position in OHL on the phase behavior of model lipid membranes. We studied the ternary mixtures of MSPC/DOPC/Chol, SMPC/DOPC/Chol, where high-T_M lipid is an OHL. We compared these findings with a ternary mixture of 15:0-PC/DOPC/Chol, in which high-T_M lipid is not an OHL but has a T_M between the two OHLs of interest. We found that 15:0-PC/DOPC/Chol and MSPC/DOPC/Chol exhibit type-II phase behavior characterized by a wide region of Lo+Ld phase coexistence (**Figures 5.3 and 5.4**). In contrast, when MSPC is replaced with SMPC in a ternary mixture, we observe a complete elimination of the macroscopic Lo+Ld coexistence at 22 °C (**Figures 5.2 and 5.3**). These findings indicate that both the number of carbons in the acyl chains and their specific placement at the *sn*-1 and *sn*-2 positions significantly influence the phase behavior of the ternary mixture at 22 °C. To further investigate the SMPC/DOPC/Chol, we used cryo-EM and FRET. Cryo-EM images reveal the nanoscopic lateral heterogeneity in this mixture **(Figure 5.4**). We observe notable variability in T_{misc} calculated for SMPC/DOPC/Chol supporting the findings from cryo-EM where SMPC promotes the formation of smaller domains. Collectively, FRET and cryo-EM suggest the presence of nanoscopic domains, although the precise domain structure and size remain challenging to resolve in SMPC/DOPC/Chol.

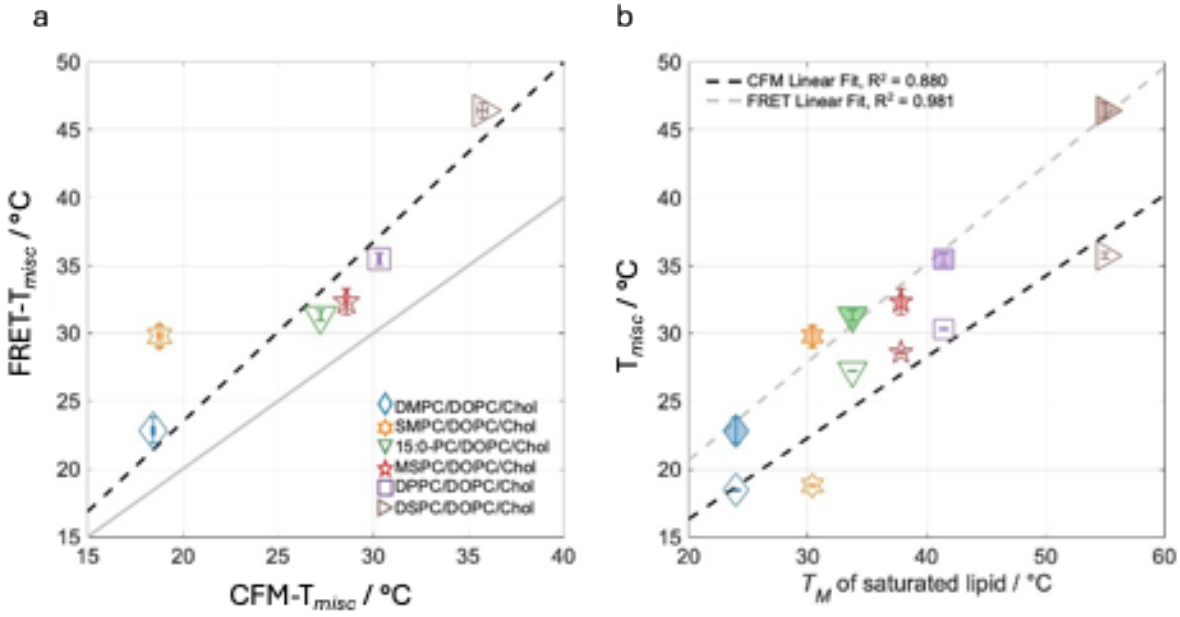


Figure 5.7) Comparing miscibility transition temperatures determined fluorescence microscopy and spectroscopy. Panel a shows T_{misc} values determined from FRET (vertical axis) and CFM (horizontal axis) for each mixture. The dashed line shows a linear fit (R^2 = 0.96) to the data points for mixtures with symmetric-chain high-T_M lipids (i.e., DMPC, 15:0-PC, DPPC, and DSPC) differing from the solid line that represents a 1:1 relationship between FRET and CFM T_{misc}. Panel b plots T_{misc} determined from FRET (filled symbols) and CFM (open symbols) for the ternary mixtures vs. the main chain transition temperature, T_M, of the high-T_M lipid.

CONCLUSIONS AND FUTURE DIRECTIONS

6.1 Conclusions

Lipid bilayers are ubiquitous in biology, and their properties are functionally important. Although originally considered to be relatively simple, non-functional structures, the complexity both in composition and in number asymmetry has become increasingly evident, along with the importance of understanding this semi-permeable barrier that is essential for a multitude of cellular processes. However, understanding specific lipid interactions remains challenging in complex mixtures, even though elucidation of these interactions can provide insight into basic biophysical principles and explanations for more complex species. This dissertation focused on one subclass of lipids, aiming to fill in some foundational knowledge on acyl chain asymmetry and its potential biological relevance.

In Chapter 2, we discussed three novel methods to quantify interdigitation between two leaflets. We provided frameworks for quantifying and visualizing interdigitation on an atomistic scale, leveraging one of the most desirable characteristics of AA-MD simulations. The first is the brute force method, which describes specific carbon-carbon interactions on a frame-step timescale, along with matrix population, allowing for the visualization of trends in carbon-carbon interactions. Using the same matrix structure, the second method utilizes the number density profile to quantify the probability of specific carbon-carbon interactions throughout a trajectory. In contrast, nISA enables the direct visualization of the bilayer midplane surface, as well as specific chain-wise interactions between leaflets.

We then implemented these techniques from Chapter 2 in AA-MD mixed chain lipid bilayers where the total sum of carbons was maintained at 32 carbons. In Chapter 3, we found that the acyl chain positioning is just as important as chain length in altering membrane properties. Furthermore, we concluded that in mixed chain lipid bilayers, those that sample an interdigitated state more often have a higher propensity to backbend, being a potential reason for mixed chain lipids forming softer bilayers.

We then introduced greater complexity by incorporating these mixed-chain lipids into ternary model membranes as the high-T_M lipid. In Chapter 4, we developed a new, user-friendly resource to determine the T_{misc} values in SP-FRET experiments of model

membrane. The models used included a uniform (3-parameter) model and two phase-separated models (4- and 5-parameter). The 3-parameter model captures the gradual increase in probe intensity with temperature. The 4-parameter model has previously been shown to effectively determine the T_{misc}, while the 5-parameter model accounts for both the parabolic intensity behavior and accurate determination of the T_{misc}. By comparing the χ^2_{red} for these models and applying the principle of parsimony, our methodology allows us to predict the phase behavior and determine the T_{misc} of the system using well-studied mixtures as proof of its application.

Chapter 5 implemented these models for fitting FRET data of ternary model membranes using mixed-chain lipids as the high-T_M lipid. CFM studies showed that replacing DPPC in DPPC/DOPC/Chol with MSPC maintained a large range of macroscopic phase separation, indicative of type-I behavior, while substitution of DPPC with SMPC, exhibits complete elimination of macroscopic phase separation. Because CFM is a diffraction-limited technique, we implemented cryo-EM, which revealed nanoscopic heterogeneity in SMPC/DOPC/Chol (40/40/20 mol %). This finding was validated using FRET data fit with our new methodologies from Chapter 4. We also found that, although T_{misc} reported from CFM and FRET share the same trend, the FRET value was consistently higher because of its sensitivity to nanoscopic heterogeneity.

Although we implemented a wide range of techniques and samples, model membranes and MD simulations simplify the complexity of the PM. Neither simulations nor model membranes provide a comprehensive framework of understanding of the complete PM membrane, as they lack bilayer asymmetries, and external structural components such as the cytoskeleton, as well as proteins. To accomplish this, future work should investigate the number and compositional differences in the leaflets of MD simulated bilayers to determine how this complexity affects the biophysical properties of mixed-chain lipids. Meanwhile, in experimental studies, this leaflet asymmetry should also be examined by determining phase behavior and leaflet phase coupling in asymmetric GUVs. Extending beyond model membranes, introducing peptides, such as gramicidin A (gA), that are known to affect membrane properites[256-258], to mixed-chain

lipids, would provide important biological frameworks for understanding the mechanical properties of these species when coupled together, especially considering the dynamic nature of SMPC. Including species like gA that alter membrane thickness would help better understand how well mixed chain lipids maintain bilayer properties with the presence of external modifications or molecules.

Overall, the work presented in this thesis underscores the importance of studying subclasses of lipids in simplified models to gain a comprehensive understanding of the biophysical mechanisms by which these lipids function. Furthermore, this research shows the value in integrating both computational and experimental approaches to allow for innovative science and method development outside project-specific goals.

LIST OF REFERENCES

(1) Gerrit van Meer, D. R. V. a. G. W. F. Membrane Bilayers: where they are and how we behave. *Nat Rev Mol Cell Bio* **2008**, *9*.

(2) Lorent, J. H.; Levental, K. R.; Ganesan, L.; Rivera-Longsworth, G.; Sezgin, E.; Doktorova, M.; Lyman, E.; Levental, I. Plasma membranes are asymmetric in lipid unsaturation, packing and protein shape. *Nat Chem Biol* **2020**, *16* (6), 644-652. DOI: 10.1038/s41589-020-0529-6.

(3) Alberts, B. J., A; Lewis, J.; et al. *Molecular Biology of the Cell*; Garland Science, 2002.

(4) Chiantia, S.; London, E. Acyl chain length and saturation modulate interleaflet coupling in asymmetric bilayers: effects on dynamics and structural order. *Biophys J* **2012**, *103* (11), 2311-2319. DOI: 10.1016/j.bpj.2012.10.033.

(5) Illya, G.; Lipowsky, R.; Shillcock, J. C. Effect of chain length and asymmetry on material properties of bilayer membranes. *J Chem Phys* **2005**, *122* (24), 244901. DOI: 10.1063/1.1917794 From NLM PubMed-not-MEDLINE.

(6) Kelley, E. G.; Frewein, M. P. K.; Czakkel, O.; Nagao, M. Nanoscale Bending Dynamics in Mixed-Chain Lipid Membranes. *Symmetry* **2023**, *15* (1). DOI: 10.3390/sym15010191.

(7) van Meer, G.; Voelker, D. R.; Feigenson, G. W. Membrane lipids: where they are and how they behave. *Nat Rev Mol Cell Bio* **2008**, *9* (2), 112-124. DOI: 10.1038/nrm2330.

(8) Mehta, D.; Crumley, E. K.; Lou, J.; Dzikovski, B.; Best, M. D.; Waxham, M. N.; Heberle, F. A. Halogenated Cholesterol Alters the Phase Behavior of Ternary Lipid Membranes. *The Journal of Physical Chemistry B* **2025**, *129* (2), 671-683. DOI: 10.1021/acs.jpcb.4c06318.

(9) Dufourc, E. J. Sterols and membrane dynamics. *J Chem Biol* **2008**, *1* (1-4), 63-77. DOI: 10.1007/s12154-008-0010-6 From NLM.

(10) Kawakami, L. M.; Yoon, B. K.; Jackman, J. A.; Knoll, W.; Weiss, P. S.; Cho, N.-J. Understanding How Sterols Regulate Membrane Remodeling in Supported Lipid Bilayers. *Langmuir* **2017**, *33* (51), 14756-14765. DOI: 10.1021/acs.langmuir.7b03236.

(11) Nyholm, T. K. M.; Jaikishan, S.; Engberg, O.; Hautala, V.; Slotte, J. P. The Affinity of Sterols for Different Phospholipid Classes and Its Impact on Lateral Segregation. *Biophys J* **2019**, *116* (2), 296-307. DOI: 10.1016/j.bpj.2018.11.3135 From NLM.
(12) Dai, J.; Alwarawrah, M.; Huang, J. Instability of cholesterol clusters in lipid bilayers and the cholesterol's Umbrella effect. *J Phys Chem B* **2010**, *114* (2), 840-848. DOI: 10.1021/jp909061h From NLM Medline.
(13) Leeb, F.; Maibaum, L. Spatially Resolving the Condensing Effect of Cholesterol in Lipid Bilayers. *Biophys J* **2018**, *115* (11), 2179-2188. DOI: 10.1016/j.bpj.2018.10.024 From NLM Medline.
(14) Leftin, A.; Molugu, T. R.; Job, C.; Beyer, K.; Brown, M. F. Area per lipid and cholesterol interactions in membranes from separated local-field (13)C NMR spectroscopy. *Biophys J* **2014**, *107* (10), 2274-2286. DOI: 10.1016/j.bpj.2014.07.044 From NLM Medline.
(15) Overton, E. Vierteljahrsschr. *Naturforsch. Ges. Zurich* **1899**, *44*, 88-135.
(16) Korn, E. D. Structure of Biological Membranes. *Science* **1966**, *153* (3743), 1491-1498. DOI: doi:10.1126/science.153.3743.1491.
(17) Kennedy, E. P.; Weiss, S. B. The Function of Cytidine Coenzymes in the Biosynthesis of Phospholipides. *Journal of Biological Chemistry* **1956**, *222* (1), 193-214. DOI: 10.1016/s0021-9258(19)50785-2.
(18) Gorter , E.; Grendel , F. ON BIMOLECULAR LAYERS OF LIPOIDS ON THE CHROMOCYTES OF THE BLOOD. *Journal of Experimental Medicine* **1925**, *41* (4), 439-443. DOI: 10.1084/jem.41.4.439 (accessed 5/28/2025).
(19) Singer, S. J.; Nicolson, G. L. The fluid mosaic model of the structure of cell membranes. *Science* **1972**, *175* (4023), 720-731. DOI: 10.1126/science.175.4023.720 From NLM Medline.
(20) Feigenson, G. W. Phase boundaries and biological membranes. *Annu Rev Biophys Biomol Struct* **2007**, *36*, 63-77. DOI: 10.1146/annurev.biophys.36.040306.132721.
(21) Hildebrand, J. H.; Scott, R. L. *Regular Solutions*; Prentice-Hall, 1962.

(22) Dill, K. B., S.;. *Molecular Driving Forces: Statistical Thermodynamics in Biology, Chemistry, Physics and Nanoscience*; Garland Science, 2010. DOI: https://doi.org/10.4324/9780203809075.
(23) Simons, K.; Ikonen, E. Functional rafts in cell membranes. *Nature* **1997**, *387* (6633), 569-572. DOI: Doi 10.1038/42408.
(24) Maxfield, F. R. Plasma membrane microdomains. *Current Opinion in Cell Biology* **2002**, *14* (4), 483-487. DOI: 10.1016/S0955-0674(02)00351-4.
(25) Veatch, S. L.; Keller, S. L. Seeing spots: complex phase behavior in simple membranes. *Biochim Biophys Acta* **2005**, *1746* (3), 172-185. DOI: 10.1016/j.bbamcr.2005.06.010 From NLM Medline.
(26) Lingwood, D.; Simons, K. Lipid rafts as a membrane-organizing principle. *Science* **2010**, *327* (5961), 46-50. DOI: 10.1126/science.1174621 From NLM Medline.
(27) Heberle, F. A.; Feigenson, G. W. Phase separation in lipid membranes. *Cold Spring Harb Perspect Biol* **2011**, *3* (4). DOI: 10.1101/cshperspect.a004630.
(28) Nickels, J. D.; Smith, J. C.; Cheng, X. Lateral organization, bilayer asymmetry, and inter-leaflet coupling of biological membranes. *Chem Phys Lipids* **2015**, *192*, 87-99. DOI: 10.1016/j.chemphyslip.2015.07.012.
(29) Heberle, F. A.; Wu, J.; Goh, S. L.; Petruzielo, R. S.; Feigenson, G. W. Comparison of three ternary lipid bilayer mixtures: FRET and ESR reveal nanodomains. *Biophys J* **2010**, *99* (10), 3309-3318. DOI: 10.1016/j.bpj.2010.09.064 From NLM Medline.
(30) Mittag, T.; Pappu, R. V. A conceptual framework for understanding phase separation and addressing open questions and challenges. *Mol Cell* **2022**, *82* (12), 2201-2214. DOI: 10.1016/j.molcel.2022.05.018 From NLM PubMed-not-MEDLINE.
(31) Veatch, S. L.; Polozov, I. V.; Gawrisch, K.; Keller, S. L. Liquid domains in vesicles investigated by NMR and fluorescence microscopy. *Biophys J* **2004**, *86* (5), 2910-2922. DOI: 10.1016/s0006-3495(04)74342-8 From NLM.
(32) Veatch, S. L.; Keller, S. L. Miscibility phase diagrams of giant vesicles containing sphingomyelin. *Physical review letters* **2005**, *94* (14), 148101.
(33) Veatch, S. L.; Keller, S. L. Organization in lipid membranes containing cholesterol. *Physical review letters* **2002**, *89* (26), 268101.

(34) Veatch, S. L.; Keller, S. L. Organization in lipid membranes containing cholesterol. *Phys Rev Lett* **2002**, *89* (26), 268101. DOI: 10.1103/PhysRevLett.89.268101 From NLM Medline.
(35) Veatch, S. L.; Keller, S. L. Separation of liquid phases in giant vesicles of ternary mixtures of phospholipids and cholesterol. *Biophysical journal* **2003**, *85* (5), 3074-3083.
(36) Heberle, F. A.; Feigenson, G. W. Phase separation in lipid membranes. *Cold Spring Harbor perspectives in biology* **2011**, *3* (4), a004630.
(37) Sharma, K. D.; Heberle, F. A.; Waxham, M. N. Visualizing lipid membrane structure with cryo-EM: past, present, and future. *Emerg Top Life Sci* **2023**, *7* (1), 55-65. DOI: 10.1042/etls20220090 From NLM.
(38) Hjort Ipsen, J.; Karlström, G.; Mourtisen, O. G.; Wennerström, H.; Zuckermann, M. J. Phase equilibria in the phosphatidylcholine-cholesterol system. *Biochimica et Biophysica Acta (BBA) - Biomembranes* **1987**, *905* (1), 162-172. DOI: https://doi.org/10.1016/0005-2736(87)90020-4.
(39) Khakbaz, P.; Klauda, J. B. Investigation of phase transitions of saturated phosphocholine lipid bilayers via molecular dynamics simulations. *Biochimica et Biophysica Acta (BBA) - Biomembranes* **2018**, *1860* (8), 1489-1501. DOI: https://doi.org/10.1016/j.bbamem.2018.04.014.
(40) Heberle, F. A.; Doktorova, M.; Scott, H. L.; Skinkle, A. D.; Waxham, M. N.; Levental, I. Direct label-free imaging of nanodomains in biomimetic and biological membranes by cryogenic electron microscopy. *Proc Natl Acad Sci U S A* **2020**, *117* (33), 19943-19952. DOI: 10.1073/pnas.2002200117.
(41) Filippov, A.; Orädd, G.; Lindblom, G. Lipid Lateral Diffusion in Ordered and Disordered Phases in Raft Mixtures. *Biophys J* **2004**, *86* (2), 891-896. DOI: 10.1016/S0006-3495(04)74164-8 (accessed 2025/06/08).
(42) Nagle, J. F.; Tristram-Nagle, S. Structure of lipid bilayers. *Biochimica et Biophysica Acta (BBA) - Reviews on Biomembranes* **2000**, *1469* (3), 159-195. DOI: https://doi.org/10.1016/S0304-4157(00)00016-2.
(43) Mihailescu, M.; Vaswani, Rishi G.; Jardón-Valadez, E.; Castro-Román, F.; Freites, J. A.; Worcester, David L.; Chamberlin, A. R.; Tobias, Douglas J.; White, Stephen H.

Acyl-Chain Methyl Distributions of Liquid-Ordered and -Disordered Membranes. *Biophys J* **2011**, *100* (6), 1455-1462. DOI: https://doi.org/10.1016/j.bpj.2011.01.035.
(44) Marques-da-Silva, D.; Lagoa, R. Rafting on the Evidence for Lipid Raft-like Domains as Hubs Triggering Environmental Toxicants' Cellular Effects. **2023**, *28* (18), 6598.
(45) Kaiser, H. J.; Lingwood, D.; Levental, I.; Sampaio, J. L.; Kalvodova, L.; Rajendran, L.; Simons, K. Order of lipid phases in model and plasma membranes. *Proc Natl Acad Sci U S A* **2009**, *106* (39), 16645-16650. DOI: 10.1073/pnas.0908987106 From NLM.
(46) Simons, K.; Toomre, D. Lipid rafts and signal transduction. *Nature reviews Molecular cell biology* **2000**, *1* (1), 31-39.
(47) Pralle, A.; Keller, P.; Florin, E.-L.; Simons, K.; Hörber, J. K. H. Sphingolipid–Cholesterol Rafts Diffuse as Small Entities in the Plasma Membrane of Mammalian Cells. *Journal of Cell Biology* **2000**, *148* (5), 997-1008. DOI: 10.1083/jcb.148.5.997 (accessed 6/15/2025).
(48) Meder, D.; Moreno, M. J.; Verkade, P.; Vaz, W. L.; Simons, K. Phase coexistence and connectivity in the apical membrane of polarized epithelial cells. *Proceedings of the National Academy of Sciences* **2006**, *103* (2), 329-334.
(49) Stone, M. B.; Shelby, S. A.; Núñez, M. F.; Wisser, K.; Veatch, S. L. Protein sorting by lipid phase-like domains supports emergent signaling function in B lymphocyte plasma membranes. *elife* **2017**, *6*, e19891.
(50) Levental, I.; Levental, K. R.; Heberle, F. A. Lipid Rafts: Controversies Resolved, Mysteries Remain. *Trends Cell Biol* **2020**, *30* (5), 341-353. DOI: 10.1016/j.tcb.2020.01.009.
(51) Carpenter, T. S.; Lopez, C. A.; Neale, C.; Montour, C.; Ingolfsson, H. I.; Di Natale, F.; Lightstone, F. C.; Gnanakaran, S. Capturing Phase Behavior of Ternary Lipid Mixtures with a Refined Martini Coarse-Grained Force Field. *J Chem Theory Comput* **2018**, *14* (11), 6050-6062. DOI: 10.1021/acs.jctc.8b00496 From NLM PubMed-not-MEDLINE.
(52) Veatch, S. L. K., Sarah L. . Separation of Liquid Phases in Giant Vesicles of Ternary Mixtures of Phospholipids and Cholesterol. *Biophyiscal Journal* **2003**, *85*.

(53) Heberle, F. A.; Petruzielo, R. S.; Pan, J.; Drazba, P.; Kucerka, N.; Standaert, R. F.; Feigenson, G. W.; Katsaras, J. Bilayer thickness mismatch controls domain size in model membranes. *J Am Chem Soc* **2013**, *135* (18), 6853-6859. DOI: 10.1021/ja3113615.
(54) Juhasz, J.; Sharom, F. J.; Davis, J. H. Quantitative characterization of coexisting phases in DOPC/DPPC/cholesterol mixtures: Comparing confocal fluorescence microscopy and deuterium nuclear magnetic resonance. *Biochimica et Biophysica Acta (BBA) - Biomembranes* **2009**, *1788* (12), 2541-2552. DOI: https://doi.org/10.1016/j.bbamem.2009.10.006.
(55) Feigenson, G. W. Phase diagrams and lipid domains in multicomponent lipid bilayer mixtures. *Biochim Biophys Acta* **2009**, *1788* (1), 47-52. DOI: 10.1016/j.bbamem.2008.08.014.
(56) Jacobson, K.; Liu, P.; Lagerholm, B. C. The Lateral Organization and Mobility of Plasma Membrane Components. *Cell* **2019**, *177* (4), 806-819. DOI: 10.1016/j.cell.2019.04.018 (accessed 2025/06/15).
(57) Doktorova, M.; Symons, J. L.; Levental, I. Structural and functional consequences of reversible lipid asymmetry in living membranes. *Nature chemical biology* **2020**, *16* (12), 1321-1330.
(58) Doktorova, M.; Symons, J. L.; Zhang, X.; Wang, H. Y.; Schlegel, J.; Lorent, J. H.; Heberle, F. A.; Sezgin, E.; Lyman, E.; Levental, K. R.; et al. Cell membranes sustain phospholipid imbalance via cholesterol asymmetry. *Cell* **2025**, *188* (10), 2586-2602 e2524. DOI: 10.1016/j.cell.2025.02.034 From NLM Medline.
(59) Contreras, F. X.; Sanchez-Magraner, L.; Alonso, A.; Goni, F. M. Transbilayer (flip-flop) lipid motion and lipid scrambling in membranes. *FEBS Lett* **2010**, *584* (9), 1779-1786. DOI: 10.1016/j.febslet.2009.12.049.
(60) Drin, G. Topological regulation of lipid balance in cells. *Annu Rev Biochem* **2014**, *83*, 51-77. DOI: 10.1146/annurev-biochem-060713-035307 From NLM.
(61) Fadeel, B.; Xue, D. The ins and outs of phospholipid asymmetry in the plasma membrane: roles in health and disease. *Crit Rev Biochem Mol Biol* **2009**, *44* (5), 264-277. DOI: 10.1080/10409230903193307.

(62) Zubia, M. V.; Yong, A. J. H.; Holtz, K. M.; Huang, E. J.; Jan, Y. N.; Jan, L. Y. TMEM16F exacerbates tau pathology and mediates phosphatidylserine exposure in phospho-tau-burdened neurons. *Proceedings of the National Academy of Sciences* **2024**, *121* (27), e2311831121. DOI: doi:10.1073/pnas.2311831121.
(63) Bratton, D. L.; Fadok, V. A.; Richter, D. A.; Kailey, J. M.; Guthrie, L. A.; Henson, P. M. Appearance of phosphatidylserine on apoptotic cells requires calcium-mediated nonspecific flip-flop and is enhanced by loss of the aminophospholipid translocase. *Journal of Biological Chemistry* **1997**, *272* (42), 26159-26165.
(64) Choubey, A.; Kalia, R. K.; Malmstadt, N.; Nakano, A.; Vashishta, P. Cholesterol translocation in a phospholipid membrane. *Biophys J* **2013**, *104* (11), 2429-2436. DOI: 10.1016/j.bpj.2013.04.036 From NLM.
(65) Lange, Y.; Ye, J.; Steck, T. L. How cholesterol homeostasis is regulated by plasma membrane cholesterol in excess of phospholipids. *Proc Natl Acad Sci U S A* **2004**, *101* (32), 11664-11667. DOI: 10.1073/pnas.0404766101 From NLM.
(66) de Duve, C. Tissue fraction-past and present. *J Cell Biol* **1971**, *50* (1), 20. From NLM.
(67) Ray, T. K.; Skipski, V. P.; Barclay, M.; Essner, E.; Archibald, F. M. Lipid composition of rat liver plasma membranes. *J Biol Chem* **1969**, *244* (20), 5528-5536. From NLM.
(68) Virtanen, J. A.; Cheng, K. H.; Somerharju, P. Phospholipid composition of the mammalian red cell membrane can be rationalized by a superlattice model. *Proc Natl Acad Sci U S A* **1998**, *95* (9), 4964-4969. DOI: 10.1073/pnas.95.9.4964 From NLM.
(69) Hossein, A.; Deserno, M. Spontaneous curvature, differential stress, and bending modulus of asymmetric lipid membranes. *Biophysical journal* **2020**, *118* (3), 624-642.
(70) Doktorova, M.; Symons, J. L.; Zhang, X.; Wang, H.-Y.; Schlegel, J.; Lorent, J. H.; Heberle, F. A.; Sezgin, E.; Lyman, E.; Levental, K. R.; et al. Cell membranes sustain phospholipid imbalance via cholesterol asymmetry. *Cell* **2025**, *188* (10), 2586-2602.e2524. DOI: 10.1016/j.cell.2025.02.034 (accessed 2025/05/28).

(71) Steck, T. L.; Lange, Y. Transverse distribution of plasma membrane bilayer cholesterol: Picking sides. *Traffic* **2018**, *19* (10), 750-760. DOI: https://doi.org/10.1111/tra.12586.
(72) Hua, L.; Akcesme, S.; Müller, K.; Heerklotz, H. A Roadmap of Responses to Asymmetry Stress in Lipid Membranes. *The Journal of Physical Chemistry B* **2025**, *129* (4), 1260-1273. DOI: 10.1021/acs.jpcb.4c05868.
(73) Flenner, E.; Das, J.; Rheinstädter, M. C.; Kosztin, I. Subdiffusion and lateral diffusion coefficient of lipid atoms and molecules in phospholipid bilayers. *Physical Review E* **2009**, *79* (1), 011907. DOI: 10.1103/PhysRevE.79.011907.
(74) Stetter, Frank W. S.; Cwiklik, L.; Jungwirth, P.; Hugel, T. Single Lipid Extraction: The Anchoring Strength of Cholesterol in Liquid-Ordered and Liquid-Disordered Phases. *Biophysical Journal* **2014**, *107* (5), 1167-1175. DOI: https://doi.org/10.1016/j.bpj.2014.07.018.
(75) Moradi, S.; Nowroozi, A.; Shahlaei, M. Shedding light on the structural properties of lipid bilayers using molecular dynamics simulation: a review study. *RSC Advances* **2019**, *9* (8), 4644-4658, 10.1039/C8RA08441F. DOI: 10.1039/C8RA08441F.
(76) Varma, M.; Deserno, M. The interplay of composition and mechanics in the thermodynamics of asymmetric ternary lipid membranes. *Faraday Discussions* **2025**, 10.1039/D4FD00196F. DOI: 10.1039/D4FD00196F.
(77) Guenza, M. G. Everything You Want to Know About Coarse-Graining and Never Dared to Ask: Macromolecules as a Key Example. *WIREs Computational Molecular Science* **2025**, *15* (2), e70022. DOI: https://doi.org/10.1002/wcms.70022.
(78) Bennett, W. F. D.; Bernardi, A.; Ozturk, T. N.; Ingólfsson, H. I.; Fox, S. J.; Sun, D.; Maupin, C. M. ezAlign: A Tool for Converting Coarse-Grained Molecular Dynamics Structures to Atomistic Resolution for Multiscale Modeling. *Molecules* **2024**, *29* (15), 3557.
(79) Aydin, F.; Georgouli, K.; Pottier, L.; Oppelstrup, T.; Carpenter, T. S.; Tempkin, J. O. B.; Bremer, P.-T.; Nissley, D. V.; Streitz, F. H.; Lightstone, F. C.; et al. Enhanced Exploration of Protein Conformational Space through Integration of Ultra-Coarse-

Grained Models to Multiscale Workflows. *The Journal of Physical Chemistry B* **2025**, *129* (20), 4895-4903. DOI: 10.1021/acs.jpcb.4c08622.
(80) Cooke, I. R.; Deserno, M. Solvent-free model for self-assembling fluid bilayer membranes: stabilization of the fluid phase based on broad attractive tail potentials. *J Chem Phys* **2005**, *123* (22), 224710. DOI: 10.1063/1.2135785 From NLM Medline.
(81) Jouhet, J. Importance of the hexagonal lipid phase in biological membrane organization. *Front Plant Sci* **2013**, *4*, 494. DOI: 10.3389/fpls.2013.00494 From NLM.
(82) Jo, S.; Kim, T.; Iyer, V. G.; Im, W. CHARMM-GUI: a web-based graphical user interface for CHARMM. *J Comput Chem* **2008**, *29* (11), 1859-1865. DOI: 10.1002/jcc.20945.
(83) Wassenaar, T. A.; Ingólfsson, H. I.; Böckmann, R. A.; Tieleman, D. P.; Marrink, S. J. Computational Lipidomics with insane: A Versatile Tool for Generating Custom Membranes for Molecular Simulations. *Journal of Chemical Theory and Computation* **2015**, *11* (5), 2144-2155. DOI: 10.1021/acs.jctc.5b00209.
(84) Marquardt, D.; Heberle, F. A.; Miti, T.; Eicher, B.; London, E.; Katsaras, J.; Pabst, G. 1H NMR Shows Slow Phospholipid Flip-Flop in Gel and Fluid Bilayers. *Langmuir* **2017**, *33* (15), 3731-3741. DOI: 10.1021/acs.langmuir.6b04485.
(85) Dolan, E. A.; Venable, R. M.; Pastor, R. W.; Brooks, B. R. Simulations of membranes and other interfacial systems using P2(1) and Pc periodic boundary conditions. *Biophys J* **2002**, *82* (5), 2317-2325. DOI: 10.1016/s0006-3495(02)75577-x From NLM.
(86) Brooks, B. R.; Brooks, C. L., 3rd; Mackerell, A. D., Jr.; Nilsson, L.; Petrella, R. J.; Roux, B.; Won, Y.; Archontis, G.; Bartels, C.; Boresch, S.; et al. CHARMM: the biomolecular simulation program. *J Comput Chem* **2009**, *30* (10), 1545-1614. DOI: 10.1002/jcc.21287 From NLM Medline.
(87) Frewein, M. P. K.; Doktorova, M.; Heberle, F. A.; Scott, H. L.; Semeraro, E. F.; Porcar, L.; Pabst, G. Structure and Interdigitation of Chain-Asymmetric Phosphatidylcholines and Milk Sphingomyelin in the Fluid Phase. *Symmetry* **2021**, *13* (8), 1441. DOI: 10.3390/sym13081441.

(88) Chaisson, E. H.; Heberle, F. A.; Doktorova, M. Quantifying Acyl Chain Interdigitation in Simulated Bilayers Via Direct Transbilayer Interactions. *bioRxiv* **2025**. DOI: 10.1101/2024.12.20.629658 From NLM PubMed-not-MEDLINE.
(89) Marsh, D. Lipid Bilayer Lateral Pressure Profile. In *Encyclopedia of Biophysics*, Roberts, G. C. K. Ed.; Springer Berlin Heidelberg, 2013; pp 1253-1256.
(90) Foley, S.; Deserno, M. Stabilizing Leaflet Asymmetry in a Highly Coarse-Grained Lipid Membrane Model. *Biophys J* **2021**, *120* (3), 146a. DOI: 10.1016/j.bpj.2020.11.1076 (accessed 2025/05/28).
(91) Chaisson, E. H.; Heberle, F. A.; Doktorova, M. Building Asymmetric Lipid Bilayers for Molecular Dynamics Simulations: What Methods Exist and How to Choose One? *Membranes (Basel)* **2023**, *13* (7). DOI: 10.3390/membranes13070629 From NLM PubMed-not-MEDLINE.
(92) Marsh, D. Protein modulation of lipids, and vice-versa, in membranes. *Biochim Biophys Acta* **2008**, *1778* (7-8), 1545-1575. DOI: 10.1016/j.bbamem.2008.01.015.
(93) Cantor, R. S. The influence of membrane lateral pressures on simple geometric models of protein conformational equilibria. *Chem Phys Lipids* **1999**, *101* (1), 45-56. DOI: 10.1016/s0009-3084(99)00054-7 From NLM.
(94) Gullingsrud, J.; Schulten, K. Lipid bilayer pressure profiles and mechanosensitive channel gating. *Biophys J* **2004**, *86* (6), 3496-3509. DOI: 10.1529/biophysj.103.034322 From NLM.
(95) Phillips, J. C.; Braun, R.; Wang, W.; Gumbart, J.; Tajkhorshid, E.; Villa, E.; Chipot, C.; Skeel, R. D.; Kale, L.; Schulten, K. Scalable molecular dynamics with NAMD. *J Comput Chem* **2005**, *26* (16), 1781-1802. DOI: 10.1002/jcc.20289.
(96) Lindahl, E.; Edholm, O. Mesoscopic Undulations and Thickness Fluctuations in Lipid Bilayers from Molecular Dynamics Simulations. *Biophys J* **2000**, *79* (1), 426-433. DOI: 10.1016/s0006-3495(00)76304-1.
(97) Sonne, J.; Hansen, F. Y.; Peters, G. H. Methodological problems in pressure profile calculations for lipid bilayers. *J Chem Phys* **2005**, *122* (12), 124903. DOI: 10.1063/1.1862624 From NLM Medline.

(98) Park, S.; Beaven, A. H.; Klauda, J. B.; Im, W. How Tolerant are Membrane Simulations with Mismatch in Area per Lipid between Leaflets? *Journal of Chemical Theory and Computation* **2015**, *11* (7), 3466-3477. DOI: 10.1021/acs.jctc.5b00232.
(99) Esteban-Martín, S.; Risselada, H. J.; Salgado, J.; Marrink, S. J. Stability of asymmetric lipid bilayers assessed by molecular dynamics simulations. *Journal of the American Chemical Society* **2009**, *131* (42), 15194-15202.
(100) Blumer, M.; Harris, S.; Li, M.; Martinez, L.; Untereiner, M.; Saeta, P. N.; Carpenter, T. S.; Ingólfsson, H. I.; Bennett, W. D. Simulations of asymmetric membranes illustrate cooperative leaflet coupling and lipid adaptability. *Frontiers in Cell and Developmental Biology* **2020**, *8*, 575.
(101) Doktorova, M.; Weinstein, H. Accurate In Silico Modeling of Asymmetric Bilayers Based on Biophysical Principles. *Biophysical Journal* **2018**, *115* (9), 1638-1643. DOI: 10.1016/j.bpj.2018.09.008.
(102) Pirhadi, E.; Vanegas, J. M.; Farin, M.; Schertzer, J. W.; Yong, X. Effect of Local Stress on Accurate Modeling of Bacterial Outer Membranes Using All-Atom Molecular Dynamics. *J Chem Theory Comput* **2023**, *19* (1), 363-372. DOI: 10.1021/acs.jctc.2c01026 From NLM.
(103) Jiang, W.; Lin, Y.-C.; Luo, Y. L. Mechanical properties of anionic asymmetric bilayers from atomistic simulations. *The Journal of Chemical Physics* **2021**, *154* (22).
(104) Renooij, W.; Van Golde, L. M. G.; Zwaal, R. F. A.; Roelofsen, B.; Van Deenen, L. L. M. Preferential incorporation of fatty acids at the inside of human erythrocyte membranes. *Biochimica et Biophysica Acta (BBA) - Biomembranes* **1974**, *363* (2), 287-292. DOI: https://doi.org/10.1016/0005-2736(74)90069-8.
(105) Van der Schaft, P. H.; Roelofsen, B.; Op den Kamp, J. A. F.; Van Deenen, L. L. M. Phospholipid asymmetry during erythropoiesis. A study on Friend erythroleukemic cells and mouse reticulocytes. *Biochimica et Biophysica Acta (BBA) - Biomembranes* **1987**, *900* (1), 103-115. DOI: https://doi.org/10.1016/0005-2736(87)90282-3.
(106) Doktorova, M.; Daum, S.; Reagle, T. R.; Cannon, H. I.; Ebenhan, J.; Neudorf, S.; Han, B.; Sharma, S.; Kasson, P.; Levental, K. R.; et al. Caveolin assemblies displace one

bilayer leaflet to organize and bend membranes. *Proceedings of the National Academy of Sciences* **2025**, *122* (20), e2417024122. DOI: doi:10.1073/pnas.2417024122.
(107) Wang, X.; Deserno, M. Determining the pivotal plane of fluid lipid membranes in simulations. *J Chem Phys* **2015**, *143* (16), 164109. DOI: 10.1063/1.4933074 From NLM.
(108) Doktorova, M.; Harries, D.; Khelashvili, G. Determination of bending rigidity and tilt modulus of lipid membranes from real-space fluctuation analysis of molecular dynamics simulations. *Physical Chemistry Chemical Physics* **2017**, *19* (25), 16806-16818. DOI: 10.1039/c7cp01921a.
(109) Bochicchio, D.; Monticelli, L. Chapter Five - The Membrane Bending Modulus in Experiments and Simulations: A Puzzling Picture. In *Advances in Biomembranes and Lipid Self-Assembly*, Iglič, A., Kulkarni, C. V., Rappolt, M. Eds.; Vol. 23; Academic Press, 2016; pp 117-143.
(110) Khelashvili, G.; Kollmitzer, B.; Heftberger, P.; Pabst, G.; Harries, D. Calculating the Bending Modulus for Multicomponent Lipid Membranes in Different Thermodynamic Phases. *Journal of Chemical Theory and Computation* **2013**, *9* (9), 3866-3871. DOI: 10.1021/ct400492e.
(111) Johner, N.; Harries, D.; Khelashvili, G. Curvature and lipid packing modulate the elastic properties of lipid assemblies: comparing HII and lamellar phases. *The journal of physical chemistry letters* **2014**, *5* (23), 4201-4206.
(112) Johner, N.; Harries, D.; Khelashvili, G. Implementation of a methodology for determining elastic properties of lipid assemblies from molecular dynamics simulations. *BMC bioinformatics* **2016**, *17*, 1-11.
(113) Pöhnl, M.; Trollmann, M. F. W.; Böckmann, R. A. Nonuniversal impact of cholesterol on membranes mobility, curvature sensing and elasticity. *Nat Commun* **2023**, *14* (1), 8038. DOI: 10.1038/s41467-023-43892-x From NLM.
(114) Sapp, K. C.; Beaven, A. H.; Sodt, A. J. Spatial extent of a single lipid's influence on bilayer mechanics. *Physical Review E* **2021**, *103* (4), 042413. DOI: 10.1103/PhysRevE.103.042413.

(115) Hossein, A. S., Alexander J. . MembraneAnalysis.jl: A Julia package for analyzing molecular dynamics simulations of lipid membranes. *Journal of Open Source Software* **2023**, *8* (87), 5380. DOI: https://doi.org/10.21105/joss.05380.
(116) Konyakhina, T. Ternary And Quaternary Lipid Phase Diagrams To Investigate Membrane Raft Behavior. **2015**.
(117) Chan, Y. H.; Boxer, S. G. Model membrane systems and their applications. *Curr Opin Chem Biol* **2007**, *11* (6), 581-587. DOI: 10.1016/j.cbpa.2007.09.020 From NLM.
(118) Baumgart, T.; Hess, S. T.; Webb, W. W. Imaging coexisting fluid domains in biomembrane models coupling curvature and line tension. *Nature* **2003**, *425* (6960), 821-824. DOI: 10.1038/nature02013.
(119) Cheng, H.-T.; London, E. Preparation and Properties of Asymmetric Large Unilamellar Vesicles: Interleaflet Coupling in Asymmetric Vesicles Is Dependent on Temperature but Not Curvature. *Biophys J* **2011**, *100* (11), 2671-2678. DOI: 10.1016/j.bpj.2011.04.048 (accessed 2025/06/10).
(120) Hoffmann, I.; Hoffmann, C.; Farago, B.; Prévost, S.; Gradzielski, M. Dynamics of small unilamellar vesicles. *The Journal of Chemical Physics* **2018**, *148* (10). DOI: 10.1063/1.5009424 (accessed 6/10/2025).
(121) Bhatia, T.; Husen, P.; Brewer, J.; Bagatolli, L. A.; Hansen, P. L.; Ipsen, J. H.; Mouritsen, O. G. Preparing giant unilamellar vesicles (GUVs) of complex lipid mixtures on demand: Mixing small unilamellar vesicles of compositionally heterogeneous mixtures. *Biochimica et Biophysica Acta (BBA) - Biomembranes* **2015**, *1848* (12), 3175-3180. DOI: https://doi.org/10.1016/j.bbamem.2015.09.020.
(122) Kennison-Cook, K. B.; Heberle, F. A. Disruption of liquid/liquid phase separation in asymmetric GUVs prepared by hemifusion. *bioRxiv* **2024**, 2024.2006.2021.600037. DOI: 10.1101/2024.06.21.600037.
(123) Mui, B. L.; Cullis, P. R.; Evans, E. A.; Madden, T. D. Osmotic properties of large unilamellar vesicles prepared by extrusion. *Biophys J* **1993**, *64* (2), 443-453. DOI: 10.1016/S0006-3495(93)81385-7 (accessed 2025/06/10).

(124) MacDonald, R. C.; MacDonald, R. I.; Menco, B. P. M.; Takeshita, K.; Subbarao, N. K.; Hu, L.-r. J. B. e. B. A.-B. Small-volume extrusion apparatus for preparation of large, unilamellar vesicles. **1991**, *1061* (2), 297-303.
(125) Arriaga, L. R.; López-Montero, I.; Monroy, F.; Orts-Gil, G.; Farago, B.; Hellweg, T. Stiffening effect of cholesterol on disordered lipid phases: a combined neutron spin echo + dynamic light scattering analysis of the bending elasticity of large unilamellar vesicles. *Biophys J* **2009**, *96* (9), 3629-3637. DOI: 10.1016/j.bpj.2009.01.045 From NLM.
(126) Doktorova, M.; Heberle, F. A.; Eicher, B.; Standaert, R. F.; Katsaras, J.; London, E.; Pabst, G.; Marquardt, D. Preparation of asymmetric phospholipid vesicles for use as cell membrane
models. *Nature Protocols* **2018**, *13* (9), 2086-2101. DOI: 10.1038/s41596-018-0033-6.
(127) Buboltz, J. T.; Feigenson, G. W. A novel strategy for the preparation of liposomes: rapid solvent exchange. *Biochimica et Biophysica Acta (BBA) - Biomembranes* **1999**, *1417* (2), 232-245. DOI: https://doi.org/10.1016/S0005-2736(99)00006-1.
(128) Enoki, T. A.; Heberle, F. A.; Feigenson, G. W. FRET Detects the Size of Nanodomains for Coexisting Liquid-Disordered and Liquid-Ordered Phases. *Biophys J* **2018**, *114* (8), 1921-1935. DOI: 10.1016/j.bpj.2018.03.014 From NLM Medline.
(129) Mardešić, I.; Boban, Z.; Subczynski, W. K.; Raguz, M. Membrane Models and Experiments Suitable for Studies of the Cholesterol Bilayer Domains. *Membranes (Basel)* **2023**, *13* (3). DOI: 10.3390/membranes13030320 From NLM.
(130) Chaves, M. A.; Ferreira, L. S.; Baldino, L.; Pinho, S. C.; Reverchon, E. J. N. Current applications of liposomes for the delivery of vitamins: A systematic review. **2023**, *13* (9), 1557.
(131) Méléard, P.; Bagatolli, L. A.; Pott, T. Chapter 9 - Giant Unilamellar Vesicle Electroformation: From Lipid Mixtures to Native Membranes Under Physiological Conditions. In *Methods in Enzymology*, Vol. 465; Academic Press, 2009; pp 161-176.
(132) Boban, Z.; Mardešić, I.; Jozić, S. P.; Šumanovac, J.; Subczynski, W. K.; Raguz, M. Electroformation of Giant Unilamellar Vesicles from Damp Lipid Films Formed by Vesicle Fusion. *Membranes* **2023**, *13* (3), 352.

(133) Angelova, M. I.; Dimitrov, D. S. Liposome electroformation. *Faraday discussions of the Chemical Society* **1986**, *81*, 303-311.
(134) Pott, T.; Bouvrais, H.; Méléard, P. Giant unilamellar vesicle formation under physiologically relevant conditions. *Chemistry and Physics of Lipids* **2008**, *154* (2), 115-119. DOI: https://doi.org/10.1016/j.chemphyslip.2008.03.008.
(135) Enoki, T. A.; Feigenson, G. W. Asymmetric Bilayers by Hemifusion: Method and Leaflet Behaviors. *Biophys J* **2019**, *117* (6), 1037-1050. DOI: 10.1016/j.bpj.2019.07.054.
(136) García-Sáez, A. J.; Chiantia, S.; Schwille, P. Effect of Line Tension on the Lateral Organization of Lipid Membranes*. *Journal of Biological Chemistry* **2007**, *282* (46), 33537-33544. DOI: https://doi.org/10.1074/jbc.M706162200.
(137) Usery, R. D.; Enoki, T. A.; Wickramasinghe, S. P.; Weiner, M. D.; Tsai, W. C.; Kim, M. B.; Wang, S.; Torng, T. L.; Ackerman, D. G.; Heberle, F. A.; et al. Line Tension Controls Liquid-Disordered + Liquid-Ordered Domain Size Transition in Lipid Bilayers. *Biophys J* **2017**, *112* (7), 1431-1443. DOI: 10.1016/j.bpj.2017.02.033 From NLM.
(138) Sarkar, P.; Chattopadhyay, A. Membrane Dipole Potential: An Emerging Approach to Explore Membrane Organization and Function. *The Journal of Physical Chemistry B* **2022**, *126* (24), 4415-4430. DOI: 10.1021/acs.jpcb.2c02476.
(139) Devaux, P. F. Static and dynamic lipid asymmetry in cell membranes. *Biochemistry* **1991**, *30* (5), 1163-1173.
(140) He, H. T.; Marguet, D. Detecting nanodomains in living cell membrane by fluorescence correlation spectroscopy. *Annu Rev Phys Chem* **2011**, *62*, 417-436. DOI: 10.1146/annurev-physchem-032210-103402 From NLM.
(141) Buboltz, J. T. Steady-state probe-partitioning fluorescence resonance energy transfer: a simple and robust tool for the study of membrane phase behavior. *Phys Rev E Stat Nonlin Soft Matter Phys* **2007**, *76* (2 Pt 1), 021903. DOI: 10.1103/PhysRevE.76.021903 From NLM Medline.
(142) Loura, L. M.; Prieto, M. FRET in Membrane Biophysics: An Overview. *Front Physiol* **2011**, *2*, 82. DOI: 10.3389/fphys.2011.00082 From NLM PubMed-not-MEDLINE.

(143) Marquardt, D.; Heberle, F. A.; Nickels, J. D.; Pabst, G.; Katsaras, J. On scattered waves and lipid domains: detecting membrane rafts with X-rays and neutrons. *Soft Matter* **2015**, *11* (47), 9055-9072, 10.1039/C5SM01807B. DOI: 10.1039/C5SM01807B.
(144) Knoll, W.; Schmidt, G.; Ibel, K.; Sackmann, E. Small-angle neutron scattering study of lateral phase separation in dimyristoylphosphatidylcholine-cholesterol mixed membranes. *Biochemistry* **1985**, *24* (19), 5240-5246. DOI: 10.1021/bi00340a043 From NLM.
(145) Yuan, Z.; Hansen, S. B. Cholesterol Regulation of Membrane Proteins Revealed by Two-Color Super-Resolution Imaging. *Membranes* **2023**, *13* (2), 250.
(146) Stöckl, M.; Nikolaus, J.; Herrmann, A. Visualization of Lipid Domain-Specific Protein Sorting in Giant Unilamellar Vesicles. In *Liposomes: Methods and Protocols, Volume 2: Biological Membrane Models*, Weissig, V. Ed.; Humana Press, 2010; pp 115-126.
(147) Kaur, A.; Kaur, P.; Ahuja, S. Forster resonance energy transfer (FRET) and applications thereof. *Anal Methods* **2020**, *12* (46), 5532-5550. DOI: 10.1039/d0ay01961e From NLM PubMed-not-MEDLINE.
(148) Mehta, D.; Crumley, E. K.; Lou, J.; Dzikovski, B.; Best, M. D.; Waxham, M. N.; Heberle, F. A. Halogenated cholesterol alters the phase behavior of ternary lipid membranes. *The Journal of Physical Chemistry B* **2025**.
(149) Lepault, J.; Pattus, F.; Martin, N. Cryo-electron microscopy of artificial biological membranes. *Biochimica et Biophysica Acta (BBA) - Biomembranes* **1985**, *820* (2), 315-318. DOI: https://doi.org/10.1016/0005-2736(85)90126-9.
(150) Bhella, D. Cryo-electron microscopy: an introduction to the technique, and considerations when working to establish a national facility. *Biophys Rev* **2019**, *11* (4), 515-519. DOI: 10.1007/s12551-019-00571-w PubMed.
(151) Huang, C.-h.; Mason, J. T. Structure and properties of mixed-chain phospholipid assemblies. *Biochimica et Biophysica Acta (BBA)-Reviews on Biomembranes* **1986**, *864* (3-4), 423-470.
(152) Makarova, M.; Peter, M.; Balogh, G.; Glatz, A.; MacRae, J. I.; Lopez Mora, N.; Booth, P.; Makeyev, E.; Vigh, L.; Oliferenko, S. Delineating the Rules for Structural

Adaptation of Membrane-Associated Proteins to Evolutionary Changes in Membrane Lipidome. *Curr Biol* **2020**, *30* (3), 367-380 e368. DOI: 10.1016/j.cub.2019.11.043 From NLM Medline.
(153) Reinhard, J.; Mattes, C.; Vath, K.; Radanovic, T.; Surma, M. A.; Klose, C.; Ernst, R. A Quantitative Analysis of Cellular Lipid Compositions During Acute Proteotoxic ER Stress Reveals Specificity in the Production of Asymmetric Lipids. *Front Cell Dev Biol* **2020**, *8*, 756. DOI: 10.3389/fcell.2020.00756 From NLM PubMed-not-MEDLINE.
(154) Capponi, S.; Freites, J. A.; Tobias, D. J.; White, S. H. Interleaflet mixing and coupling in liquid-disordered phospholipid bilayers. *Biochim. Biophys. Acta* **2016**, *1858* (2), 354-362. DOI: 10.1016/j.bbamem.2015.11.024.
(155) Rog, T.; Orlowski, A.; Llorente, A.; Skotland, T.; Sylvanne, T.; Kauhanen, D.; Ekroos, K.; Sandvig, K.; Vattulainen, I. Interdigitation of long-chain sphingomyelin induces coupling of membrane leaflets in a cholesterol dependent manner. *Biochim. Biophys. Acta* **2016**, *1858* (2), 281-288. DOI: 10.1016/j.bbamem.2015.12.003.
(156) Mavromoustakos, T.; Chatzigeorgiou, P.; Koukoulitsa, C.; Durdagi, S. Partial interdigitation of lipid bilayers. *International Journal of Quantum Chemistry* **2011**, *111* (6), 1172-1183, https://doi.org/10.1002/qua.22610. DOI: https://doi.org/10.1002/qua.22610 (accessed 2023/03/08).
(157) Boggs, J. M.; Rangaraj, G.; Watts, A. Behavior of spin labels in a variety of interdigitated lipid bilayers. *Biochimica et Biophysica Acta (BBA) - Biomembranes* **1989**, *981* (2), 243-253. DOI: https://doi.org/10.1016/0005-2736(89)90034-5.
(158) Slater, J. L.; Huang, C. H. Interdigitated bilayer membranes. *Prog Lipid Res* **1988**, *27* (4), 325-359. DOI: 10.1016/0163-7827(88)90010-0.
(159) Pinto, S. N.; Silva, L. C.; de Almeida, R. F.; Prieto, M. Membrane domain formation, interdigitation, and morphological alterations induced by the very long chain asymmetric C24:1 ceramide. *Biophys J* **2008**, *95* (6), 2867-2879. DOI: 10.1529/biophysj.108.129858 From NLM Medline.
(160) Jiménez-Rojo, N.; García-Arribas, A. B.; Sot, J.; Alonso, A.; Goñi, F. M. Lipid bilayers containing sphingomyelins and ceramides of varying N-acyl lengths: A glimpse

into sphingolipid complexity. *Biochimica et Biophysica Acta (BBA) - Biomembranes* **2014**, *1838* (1, Part B), 456-464. DOI: https://doi.org/10.1016/j.bbamem.2013.10.010.
(161) Bondar, O. P.; Pivovarenko, V. G.; Rowe, E. S. Flavonols - new fluorescent membrane probes for studying the interdigitation of lipid bilayers. *Biochimica et Biophysica Acta (BBA) - Biomembranes* **1998**, *1369* (1), 119-130. DOI: https://doi.org/10.1016/S0005-2736(97)00218-6.
(162) Schram, V.; Thompson, T. E. Interdigitation does not affect translational diffusion of lipids in liquid crystalline bilayers. *Biophys J* **1995**, *69* (6), 2517-2520. DOI: 10.1016/s0006-3495(95)80122-0.
(163) Murata, M.; Umegawa, Y.; Fukunaga, S.; Yasuda, T. A Fluorescent Probe for C24 Fatty Acids to Report the Deep Interior of Lipid Bilayers. *Synlett* **2023**. DOI: 10.1055/a-2210-1162.
(164) Rog, T.; Orlowski, A.; Llorente, A.; Skotland, T.; Sylvanne, T.; Kauhanen, D.; Ekroos, K.; Sandvig, K.; Vattulainen, I. Interdigitation of long-chain sphingomyelin induces coupling of membrane leaflets in a cholesterol dependent manner. *Biochim Biophys Acta* **2016**, *1858* (2), 281-288. DOI: 10.1016/j.bbamem.2015.12.003 From NLM Medline.
(165) Seo, S.; Murata, M.; Shinoda, W. Pivotal Role of Interdigitation in Interleaflet Interactions: Implications from Molecular Dynamics Simulations. *J Phys Chem Lett* **2020**, *11* (13), 5171-5176. DOI: 10.1021/acs.jpclett.0c01317 From NLM PubMed-not-MEDLINE.
(166) Niemela, P. S.; Hyvonen, M. T.; Vattulainen, I. Influence of chain length and unsaturation on sphingomyelin bilayers. *Biophys J* **2006**, *90* (3), 851-863. DOI: 10.1529/biophysj.105.067371 From NLM Medline.
(167) Bacle, A.; Gautier, R.; Jackson, C. L.; Fuchs, P. F. J.; Vanni, S. Interdigitation between Triglycerides and Lipids Modulates Surface Properties of Lipid Droplets. *Biophys J* **2017**, *112* (7), 1417-1430. DOI: 10.1016/j.bpj.2017.02.032 From NLM Medline.

(168) Devanand, T.; Krishnaswamy, S.; Vemparala, S. Interdigitation of Lipids Induced by Membrane-Active Proteins. *J Membr Biol* **2019**, *252* (4-5), 331-342. DOI: 10.1007/s00232-019-00072-7 From NLM Medline.
(169) Phillips, J. C.; Hardy, D. J.; Maia, J. D. C.; Stone, J. E.; Ribeiro, J. V.; Bernardi, R. C.; Buch, R.; Fiorin, G.; Henin, J.; Jiang, W.; et al. Scalable molecular dynamics on CPU and GPU architectures with NAMD. *J Chem Phys* **2020**, *153* (4), 044130. DOI: 10.1063/5.0014475 From NLM PubMed-not-MEDLINE.
(170) Klauda, J. B.; Venable, R. M.; Freites, J. A.; O'Connor, J. W.; Tobias, D. J.; Mondragon-Ramirez, C.; Vorobyov, I.; MacKerell, A. D., Jr.; Pastor, R. W. Update of the CHARMM all-atom additive force field for lipids: validation on six lipid types. *J Phys Chem B* **2010**, *114* (23), 7830-7843. DOI: 10.1021/jp101759q From NLM Medline.
(171) Chodera, J. D. A Simple Method for Automated Equilibration Detection in Molecular Simulations. *J Chem Theory Comput* **2016**, *12* (4), 1799-1805. DOI: 10.1021/acs.jctc.5b00784 From NLM Medline.
(172) Feller, S. E.; Pastor, R. W. Constant surface tension simulations of lipid bilayers: the sensitivity of surface areas and compressibilities. *The Journal of chemical physics* **1999**, *111* (3), 1281-1287.
(173) Humphrey, W.; Dalke, A.; Schulten, K. VMD: visual molecular dynamics. *J Mol Graph* **1996**, *14* (1), 33-38, 27-38. DOI: 10.1016/0263-7855(96)00018-5.
(174) Cheng, S. Y., Duong, H.V., Compton, C., Vaughn, M.W., Nguyen, H., Cheng, K.H. Characterization of 3D Voronoi Tessellation Nearest Neighbor Lipid Shells Provides Atomistic Lipid Disruption Profile of Protein Containing Lipid Membranes. *Biophysical Chemistry* **2015**, *198*, 22-35. DOI: doi:10.1016/j.bpc.2015.01.005.
(175) Greenfield, M. L.; Martin, L. M.; Joodaki, F. Computing Individual Area per Head Group Reveals Lipid Bilayer Dynamics. *The Journal of Physical Chemistry B* **2022**, *126* (50), 10697-10711. DOI: 10.1021/acs.jpcb.2c04633.
(176) Rycroft, C. H. VORO++: a three-dimensional voronoi cell library in C++. *Chaos* **2009**, *19* (4), 041111. DOI: 10.1063/1.3215722.
(177) Guixà-González, R.; Rodriguez-Espigares, I.; Ramírez-Anguita, J. M.; Carrió-Gaspar, P.; Martinez-Seara, H.; Giorgino, T.; Selent, J. MEMBPLUGIN: studying

membrane complexity in VMD. *Bioinformatics* **2014**, *30* (10), 1478-1480. DOI: 10.1093/bioinformatics/btu037 (accessed 12/10/2021).
(178) Doktorova, M.; Khelashvili, G.; Ashkar, R.; Brown, M. F. Molecular simulations and NMR reveal how lipid fluctuations affect membrane mechanics. *Biophys. J.* **2023**, *122* (6), 984-1002. DOI: 10.1016/j.bpj.2022.12.007 From NLM Medline.
(179) Doktorova, M.; LeVine, M. V.; Khelashvili, G.; Weinstein, H. A New Computational Method for Membrane Compressibility: Bilayer Mechanical Thickness Revisited. *Biophys. J.* **2019**, *116* (3), 487-502. DOI: 10.1016/j.bpj.2018.12.016.
(180) Koenig, B. W.; Gawrisch, K. Specific volumes of unsaturated phosphatidylcholines in the liquid crystalline lamellar phase. *Biochim. Biophys. Acta* **2005**, *1715* (1), 65-70. DOI: 10.1016/j.bbamem.2005.07.006 From NLM Medline.
(181) Marsh, D. Molecular volumes of phospholipids and glycolipids in membranes. *Chem. Phys. Lipids* **2010**, *163* (7), 667-677. DOI: 10.1016/j.chemphyslip.2010.06.005 From NLM Medline.
(182) Harayama, T.; Riezman, H. Understanding the diversity of membrane lipid composition. *Nat Rev Mol Cell Biol* **2018**, *19* (5), 281-296. DOI: 10.1038/nrm.2017.138 From NLM Medline.
(183) Kucerka, N.; Nieh, M. P.; Katsaras, J. Fluid phase lipid areas and bilayer thicknesses of commonly used phosphatidylcholines as a function of temperature. *Biochim Biophys Acta* **2011**, *1808* (11), 2761-2771. DOI: 10.1016/j.bbamem.2011.07.022 From NLM Medline.
(184) Kucerka, N.; Heberle, F. A.; Pan, J.; Katsaras, J. Structural Significance of Lipid Diversity as Studied by Small Angle Neutron and X-ray Scattering. *Membranes (Basel)* **2015**, *5* (3), 454-472. DOI: 10.3390/membranes5030454 From NLM PubMed-not-MEDLINE.
(185) Rawicz, W.; Olbrich, K. C.; McIntosh, T.; Needham, D.; Evans, E. Effect of chain length and unsaturation on elasticity of lipid bilayers. *Biophys J* **2000**, *79* (1), 328-339.
(186) Nagao, M.; Kelley, E. G.; Ashkar, R.; Bradbury, R.; Butler, P. D. Probing Elastic and Viscous Properties of Phospholipid Bilayers Using Neutron Spin Echo Spectroscopy.

The Journal of Physical Chemistry Letters **2017**, *8* (19), 4679-4684. DOI: 10.1021/acs.jpclett.7b01830.
(187) Goni, F. M.; Alonso, A. Biophysics of sphingolipids I. Membrane properties of sphingosine, ceramides and other simple sphingolipids. *Biochim Biophys Acta* **2006**, *1758* (12), 1902-1921. DOI: 10.1016/j.bbamem.2006.09.011 From NLM Medline.
(188) Frewein, M. P. K.; Piller, P.; Semeraro, E. F.; Batchu, K. C.; Heberle, F. A.; Scott, H. L.; Gerelli, Y.; Porcar, L.; Pabst, G. Interdigitation-Induced Order and Disorder in Asymmetric Membranes. *J Membr Biol* **2022**, *255* (4-5), 407-421. DOI: 10.1007/s00232-022-00234-0 From NLM Medline.
(189) Smith, P.; Owen, D. M.; Lorenz, C. D.; Makarova, M. Asymmetric glycerophospholipids impart distinctive biophysical properties to lipid bilayers. *Biophys J* **2021**, *120* (9), 1746-1754. DOI: 10.1016/j.bpj.2021.02.046 From NLM.
(190) Ozturk, T. N.; Ferron, T. J.; He, W.; Schwarz, B.; Weiss, T. M.; Fischer, N. O.; Rasley, A.; Carpenter, T. S.; Bosio, C. M.; Ingólfsson, H. I. Highly tail-asymmetric lipids interdigitate and cause bidirectional ordering. *Journal of Lipid Research* **2025**, *66* (5), 100797. DOI: https://doi.org/10.1016/j.jlr.2025.100797.
(191) Marsh, D. Structural and thermodynamic determinants of chain-melting transition temperatures for phospholipid and glycolipids membranes. *Biochim Biophys Acta* **2010**, *1798* (1), 40-51. DOI: 10.1016/j.bbamem.2009.10.010 From NLM Medline.
(192) Yee, S. M.; Gillams, R. J.; McLain, S. E.; Lorenz, C. D. Effects of lipid heterogeneity on model human brain lipid membranes. *Soft Matter* **2021**, *17* (1), 126-135. DOI: 10.1039/d0sm01766c From NLM Medline.
(193) Kelley, E. G.; Butler, P. D.; Ashkar, R.; Bradbury, R.; Nagao, M. Scaling relationships for the elastic moduli and viscosity of mixed lipid membranes. *Proceedings of the National Academy of Sciences* **2020**, *117* (38), 23365-23373. DOI: doi:10.1073/pnas.2008789117.
(194) Seifert, U. Configurations of fluid membranes and vesicles. *Advances in Physics* **1997**, *46* (1), 13-137. DOI: 10.1080/00018739700101488.
(195) Seifert, U.; Langer, S. A. J. E. L. Viscous modes of fluid bilayer membranes. **1993**, *23* (1), 71.

(196) Ali, S.; Smaby, J. M.; Momsen, M. M.; Brockman, H. L.; Brown, R. E. J. B. j. Acyl chain-length asymmetry alters the interfacial elastic interactions of phosphatidylcholines. **1998**, *74* (1), 338-348.
(197) Dan, N. J. B. e. B. A.-B. Lipid tail chain asymmetry and the strength of membrane-induced interactions between membrane proteins. **2007**, *1768* (10), 2393-2399.
(198) Scott, H. L.; Burns-Casamayor, V.; Dixson, A. C.; Standaert, R. F.; Stanley, C. B.; Stingaciu, L.-R.; Carrillo, J.-M. Y.; Sumpter, B. G.; Katsaras, J.; Qiang, W.; et al. Neutron spin echo shows pHLIP is capable of retarding membrane thickness fluctuations. *Biochimica et Biophysica Acta (BBA) - Biomembranes* **2024**, *1866* (7), 184349. DOI: https://doi.org/10.1016/j.bbamem.2024.184349.
(199) Bhandarkar, M., Brunner, R., Chipot, C., Dalke, A., Dixit, S., Grayson, P., Gullingsrud, J., Gursoy, A., Hardy, D., Hénin, J., Humphrey, W., Hurwitz, D., Krawetz, N., Kumar, S., Nelson, M., Phillips, J., Shinozaki, A., Zheng, G., Zhu, F. *NAMD User's Guide*. 2006. https://www.ks.uiuc.edu/Research/namd/cvs/ug.pdf (accessed).
(200) Foley, S. L.; Deserno, M. Quantifying uncertainty in trans-membrane stresses and moments in simulation. *Methods Enzymol* **2024**, *701*, 83-122. DOI: 10.1016/bs.mie.2024.04.008 From NLM Medline.
(201) Stillwell, W. *AN INTRODUCTION TO BIOLOGICAL MEMBRANES COMPOSITION, STRUCTURE AND FUNCTION*; Elsevier, 2016.
(202) Szleifer, I.; Kramer, D.; Ben-Shaul, A.; Gelbart, W. M.; Safran, S. A. Molecular theory of curvature elasticity in surfactant films. *The Journal of Chemical Physics* **1990**, *92* (11), 6800-6817. DOI: 10.1063/1.458267 (accessed 6/6/2025).
(203) MathWorks, I. *MATLAB : the language of technical computing : computation, visualization, programming*; Natwick : Math Works Inc., 1996., 2021.
(204) Piggot, T. J.; Allison, J. R.; Sessions, R. B.; Essex, J. W. On the Calculation of Acyl Chain Order Parameters from Lipid Simulations. *Journal of Chemical Theory and Computation* **2017**, *13* (11), 5683-5696. DOI: 10.1021/acs.jctc.7b00643.
(205) Doktorova, M.; Levine, M. V.; Khelashvili, G.; Weinstein, H. A New Computational Method for Membrane Compressibility: Bilayer Mechanical Thickness Revisited. *Biophys J* **2019**, *116* (3), 487-502. DOI: 10.1016/j.bpj.2018.12.016.

(206) Karal, M. A. S.; Billah, M. M.; Ahmed, M.; Ahamed, M. K. A review on the measurement of the bending rigidity of lipid membranes. *Soft Matter* **2023**, *19* (43), 8285-8304. DOI: 10.1039/d3sm00882g From NLM Medline.
(207) Helfrich, W. Elastic Properties of Lipid Bilayers: Theory and Possible Experiments. *Zeitschrift für Naturforschung C* **1973**, *28* (11-12), 693-703. DOI: doi:10.1515/znc-1973-11-1209 (accessed 2025-06-07).
(208) Dahman, Y. Chapter 3 - Smart Nanomaterials**By Yaser Dahman, Adil Kamil, and Daniel Baena. In *Nanotechnology and Functional Materials for Engineers*, Dahman, Y. Ed.; Elsevier, 2017; pp 47-66.
(209) Evans, E. A. Bending resistance and chemically induced moments in membrane bilayers. *Biophys J* **1974**, *14* (12), 923-931. DOI: 10.1016/S0006-3495(74)85959-X.
(210) Zhao, B.; Brittain, W. J. Polymer brushes: surface-immobilized macromolecules. *Progress in Polymer Science* **2000**, *25* (5), 677-710.
(211) Shchelokovskyy, P.; Tristram-Nagle, S.; Dimova, R. Effect of the HIV-1 fusion peptide on the mechanical properties and leaflet coupling of lipid bilayers. *New Journal of Physics* **2011**, *13* (2), 025004. DOI: 10.1088/1367-2630/13/2/025004.
(212) Huster, D.; Arnold, K.; Gawrisch, K. Investigation of lipid organization in biological membranes by two-dimensional nuclear Overhauser enhancement spectroscopy. *The Journal of Physical Chemistry B* **1999**, *103* (1), 243-251.
(213) Lewis, B. A.; Engelman, D. M. Lipid bilayer thickness varies linearly with acyl chain length in fluid phosphatidylcholine vesicles. *J Mol Biol* **1983**, *166* (2), 211-217. DOI: 10.1016/s0022-2836(83)80007-2 From NLM.
(214) Kranenburg, M.; Vlaar, M.; Smit, B. Simulating Induced Interdigitation in Membranes. *Biophys J* **2004**, *87* (3), 1596-1605. DOI: https://doi.org/10.1529/biophysj.104.045005.
(215) Muddana, H. S.; Gullapalli, R. R.; Manias, E.; Butler, P. J. Atomistic simulation of lipid and DiI dynamics in membrane bilayers under tension. *Physical Chemistry Chemical Physics* **2011**, *13* (4), 1368-1378, 10.1039/C0CP00430H. DOI: 10.1039/C0CP00430H.

(216) Evans, E.; Rawicz, W. J. P. r. l. Entropy-driven tension and bending elasticity in condensed-fluid membranes. **1990**, *64* (17), 2094.
(217) Waheed, Q.; Edholm, O. Undulation Contributions to the Area Compressibility in Lipid Bilayer Simulations. *Biophys J* **2009**, *97* (10), 2754-2760. DOI: https://doi.org/10.1016/j.bpj.2009.08.048.
(218) Elani, Y.; Purushothaman, S.; Booth, P. J.; Seddon, J. M.; Brooks, N. J.; Law, R. V.; Ces, O. Measurements of the effect of membrane asymmetry on the mechanical properties of lipid bilayers. *Chem Commun (Camb)* **2015**, *51* (32), 6976-6979. DOI: 10.1039/c5cc00712g.
(219) Shkulipa, S.; den Otter, W. K.; Briels, W. J. J. P. r. l. Thermal Undulations of Lipid Bilayers Relax by Intermonolayer Friction<? format?> at Submicrometer Length Scales. **2006**, *96* (17), 178302.
(220) Sharma, K. D. Investigating Liquid-Liquid Phase Separation in Lipid Bilayers: A Multi-Modal Approach Utilizing Spectroscopy, Microscopy, and Cryo-EM University of Tennessee Knoxville, 2024. https://trace.tennessee.edu/utk_graddiss/10502.
(221) Kingsley, P. B.; Feigenson, G. W. The synthesis of a perdeuterated phospholipid: 1,2-dimyristoyl-sn-glycero-3-phosphocholine-d72. *Chemistry and Physics of Lipids* **1979**, *24* (2), 135-147. DOI: https://doi.org/10.1016/0009-3084(79)90083-5.
(222) **!!! INVALID CITATION !!! 9**.
(223) Konyakhina, T. M.; Wu, J.; Mastroianni, J. D.; Heberle, F. A.; Feigenson, G. W. Phase diagram of a 4-component lipid mixture: DSPC/DOPC/POPC/chol. *Biochimica et Biophysica Acta (BBA) - Biomembranes* **2013**, *1828* (9), 2204-2214. DOI: https://doi.org/10.1016/j.bbamem.2013.05.020.
(224) Kinnun, J. J.; Bolmatov, D.; Lavrentovich, M. O.; Katsaras, J. Lateral heterogeneity and domain formation in cellular membranes. *Chemistry and physics of lipids* **2020**, *232*, 104976.
(225) Sezgin, E.; Levental, I.; Mayor, S.; Eggeling, C. The mystery of membrane organization: composition, regulation and roles of lipid rafts. *Nature reviews Molecular cell biology* **2017**, *18* (6), 361-374.

(226) Levental, I.; Levental, K. R.; Heberle, F. A. Lipid rafts: controversies resolved, mysteries remain. *Trends in cell biology* **2020**, *30* (5), 341-353.
(227) Simons, K.; Sampaio, J. L. Membrane organization and lipid rafts. (1943-0264 (Electronic)). From 2011 Oct 1.
(228) Simons, K.; Vaz, W. L. C. Model systems, lipid rafts, and cell membranes. **2004**.
(229) Kai, S.; Elina, I. Functional rafts in cell membranes. *Nature* **1997**, *387* (6633), 569-572.
(230) Alonso, M. A.; Millán, J. The role of lipid rafts in signalling and membrane trafficking in T lymphocytes. *Journal of cell science* **2001**, *114* (22), 3957-3965.
(231) Levental, I.; Veatch, S. L. The continuing mystery of lipid rafts. *Journal of molecular biology* **2016**, *428* (24), 4749-4764.
(232) Waheed, A. A.; Freed, E. O. The Role of Lipids in Retrovirus Replication. In *Viruses*, 2010; Vol. 2, pp 1146-1180.
(233) Heberle, F. A.; Petruzielo, R. S.; Pan, J.; Drazba, P.; Kučerka, N.; Standaert, R. F.; Feigenson, G. W.; Katsaras, J. Bilayer thickness mismatch controls domain size in model membranes. *Journal of the American Chemical Society* **2013**, *135* (18), 6853-6859.
(234) Kollmitzer, B.; Heftberger, P.; Podgornik, R.; Nagle, J. F.; Pabst, G. Bending rigidities and interdomain forces in membranes with coexisting lipid domains. *Biophysical journal* **2015**, *108* (12), 2833-2842.
(235) Kulkarni, R.; Wiemer, E. A. C.; Chang, W. Role of lipid rafts in pathogen-host interaction-a mini review. *Frontiers in Immunology* **2021**, *12*.
(236) Shaw, A. S. Lipid rafts: now you see them, now you don't. *Nature immunology* **2006**, *7* (11), 1139-1142.
(237) Feigenson, G. W. Phase diagrams and lipid domains in multicomponent lipid bilayer mixtures. *Biochimica et Biophysica Acta (BBA)-Biomembranes* **2009**, *1788* (1), 47-52.
(238) Harayama, T.; Riezman, H. Understanding the diversity of membrane lipid composition. *Nature reviews Molecular cell biology* **2018**, *19* (5), 281-296.

(239) Veatch, S. L.; Keller, S. L. Seeing spots: complex phase behavior in simple membranes. *Biochimica et Biophysica Acta (BBA)-Molecular Cell Research* **2005**, *1746* (3), 172-185.
(240) Pan, J.; Heberle, F. A.; Petruzielo, R. S.; Katsaras, J. Using small-angle neutron scattering to detect nanoscopic lipid domains. *Chemistry and physics of lipids* **2013**, *170*, 19-32.
(241) Heberle, F. A.; Wu, J.; Goh, S. L.; Petruzielo, R. S.; Feigenson, G. W. Comparison of three ternary lipid bilayer mixtures: FRET and ESR reveal nanodomains. *Biophysical journal* **2010**, *99* (10), 3309-3318.
(242) Enoki, T. A.; Heberle, F. A.; Feigenson, G. W. FRET detects the size of nanodomains for coexisting liquid-disordered and liquid-ordered phases. *Biophysical Journal* **2018**, *114* (8), 1921-1935.
(243) Heberle, F. A.; Doktorova, M.; Scott, H. L.; Skinkle, A. D.; Waxham, M. N.; Levental, I. Direct label-free imaging of nanodomains in biomimetic and biological membranes by cryogenic electron microscopy. *Proceedings of the National Academy of Sciences* **2020**, *117* (33), 19943-19952.
(244) Lorent, J. H.; Levental, K. R.; Ganesan, L.; Rivera-Longsworth, G.; Sezgin, E.; Doktorova, M.; Lyman, E.; Levental, I. Plasma membranes are asymmetric in lipid unsaturation, packing and protein shape. *Nature chemical biology* **2020**, *16* (6), 644-652.
(245) Goñi, F. M.; Alonso, A. Biophysics of sphingolipids I. Membrane properties of sphingosine, ceramides and other simple sphingolipids. *Biochimica et Biophysica Acta (BBA)-Biomembranes* **2006**, *1758* (12), 1902-1921.
(246) Jimenez-Rojo, N.; Garcia-Arribas, A. B.; Sot, J.; Alonso, A.; Goni, F. M. Lipid bilayers containing sphingomyelins and ceramides of varying N-acyl lengths: a glimpse into sphingolipid complexity. *Biophysical Journal* **2014**, *106* (2), 289a.
(247) Makarova, M.; Peter, M.; Balogh, G.; Glatz, A.; MacRae, J. I.; Mora, N. L.; Booth, P.; Makeyev, E.; Vigh, L.; Oliferenko, S. Delineating the rules for structural adaptation of membrane-associated proteins to evolutionary changes in membrane lipidome. *Current Biology* **2020**, *30* (3), 367-380.

(248) Kelley, E. G.; Butler, P. D.; Nagao, M. Collective dynamics in model biological membranes measured by neutron spin echo spectroscopy. *Characterization of Biological Membranes* **2019**, 131-176.
(249) Kingsley, P. B.; Feigenson, G. W. The synthesis of a perdeuterated phospholipid: 1, 2-dimyristoyl-sn-glycero-3-phosphocholine-d72. *Chemistry and physics of lipids* **1979**, *24* (2), 135-147.
(250) Heberle, F. A.; Waxham, M. N. Phase separation in model lipid membranes investigated with cryogenic electron microscopy. *Methods in Enzymology* **2024**, *700*, 189-216.
(251) Heberle, F. A.; Welsch, D.; Scott, H. L.; Waxham, M. N. Optimization of cryo-electron microscopy for quantitative analysis of lipid bilayers. *Biophysical Reports* **2023**, *3* (1), 100090.
(252) Rohou, A.; Grigorieff, N. CTFFIND4: Fast and accurate defocus estimation from electron micrographs. *Journal of structural biology* **2015**, *192* (2), 216-221.
(253) Kiewisz, R.; Fabig, G.; Müller-Reichert, T.; Bepler, T. Automated segmentation of 3D cytoskeletal filaments from electron micrographs with TARDIS. Oxford University Press US: 2023.
(254) Sharma, K. D.; Doktorova, M.; Waxham, M. N.; Heberle, F. A. Cryo-EM images of phase-separated lipid bilayer vesicles analyzed with a machine-learning approach. *Biophysical Journal* **2024**.
(255) Heftberger, P.; Kollmitzer, B.; Rieder, A. A.; Amenitsch, H.; Pabst, G. In situ determination of structure and fluctuations of coexisting fluid membrane domains. *Biophysical journal* **2015**, *108* (4), 854-862.
(256) Kim, T.; Lee, K. I.; Morris, P.; Pastor, R. W.; Andersen, O. S.; Im, W. Influence of hydrophobic mismatch on structures and dynamics of gramicidin a and lipid bilayers. *Biophys J* **2012**, *102* (7), 1551-1560. DOI: 10.1016/j.bpj.2012.03.014 From NLM.
(257) Kelley, E. G.; Butler, P. D.; Nagao, M. Collective dynamics in lipid membranes containing transmembrane peptides. *Soft Matter* **2021**, *17* (23), 5671-5681. DOI: 10.1039/d1sm00314c From NLM.

(258) Doktorova, M.; Heberle, F. A.; Marquardt, D.; Rusinova, R.; Sanford, R. L.; Peyear, T. A.; Katsaras, J.; Feigenson, G. W.; Weinstein, H.; Andersen, O. S. Gramicidin Increases Lipid Flip-Flop in Symmetric and Asymmetric Lipid Vesicles. *Biophys J* **2019**, *116* (5), 860-873. DOI: 10.1016/j.bpj.2019.01.016 From NLM.
(259) *Mathematica*; Wolfram Research Inc.: 2024. https://www.wolfram.com/mathematica.

APPENDICES

Appendix 1)Supplemental Information for Chapter 1

Appendix 1.1) Tcl script for modifying chain symmetric lipids into mixed chain lipids.

Below is an annotated sample script of how to modify lipid structure using CHARMM formatting from saturated chain symmetric lipids into MCL. In this case, a DSPC bilayer was generated and is being modified into a SMPC bilayer.

Select the atoms that are going to be kept.

```
1. set sel [atomselect top "not (resname DSPC and name C218 C216 H18S H18R
   C217 H17R H18T H17S H16S H16R H15R H15S)"]
```

Write only the selected atoms to a pdb and psf.

```
2. $sel writepsf noC16down.psf
3. $sel writepdb noC16down.pdb
```

Unload the file.

```
4. mol delete all
```

Load the new psf and pdb that were created in lines 2 and 3

```
5. mol load psf noC16down.psf pdb noC16down.pdb
```

Select the parent lipid that will be modified, in this example it is DSPC.

```
6. set sel [atomselect top "resname DSPC"]
```

Change the resname from DSPC to the final lipid resname (SMPC).

```
7. $sel set resname SMPC
```

Select the n carbon and change it type to be a terminal methyl carbon

```
8. set sel [atomselect top "name C214"]
9. $sel set type CTL3
```

Change the charge to be a terminal methyl carbon

```
10. $sel set charge -0.27
```

Select the n+1 carbon.

```
11. set sel [atomselect top "name C215"]
```

Change the carbon name and type to be a terminal methyl hydrogen and

```
12. $sel set name H14T
13. $sel set type HAL3
```

Change the charge to be a terminal methyl hydrogen from an methylene carbon.

```
14. $sel set charge 0.09
```

Change the previous n carbon methylene hydrogens to methyl hydrogens.

```
15. set sel [atomselect top "name H14S H14R"]
16. $sel set type HAL3
```

Updated the charge to be terminal methyl hydrogens.

```
17. $sel set charge 0.09
```

Select all molecules and write it to a pdb and psf.

```
18. set sel [atomselect top "all"]
19. $sel writepsf NewPSF.psf
20. $sel writepdb NewPDB.pdb
```

Unload all molecules and reload the new psf, pdb, and validate the changes.

```
21. mol delete all
22. mol load psf NewPSF.psf pdb NewPDB.pdb
```

Appendix 2) Supplemental Information for Chapter 2

These figures and tables from Chapter 2 were originally published as listed below in the Supplemetal Information from the following paper and is reproduced with under the terms CC-BY 4.0 .

Emily H. Chaisson, Frederick A. Heberle, Milka Doktorova. "Quantifying Acyl Chain Interdigitaiton in simulated bilayers via direct transbilayer interactions" *JCIM* 2025; *65* (8), 3879-3885

This chapter describes algorithms designed by E.H.C., F.A. H., and M.D. Data analysis was performed by E.H.C and F.A.H. Preparation of the manuscript was prepared by myself, F.A. H., and M.D.

Appendix 2.1) Interdigitation and structural parameters of simulated bilayers.

Table A2.1) Interdigitation and structural parameters of simulated bilayers. Listed are the results from memIT, nISA, ccMat and doMat (both the total matrix sums and individual quadrant sums), the average area per lipid and average phosphate-to-phosphate distance (PP-dist). Errors are calculated from block averaging as described in Appendix 2.4. This table is reused from [88] by the terms of CC-BY-4.0.

	$DPPC_T$	DPPC	MSPC
memIT / dimensionless	0.270 ± 0.0019	0.282 ± 0.0013	0.324 ± 0.0014
nISA / dimensionless	3.94 ± 0.011	4.03 ± 0.010	4.26 ± 0.010
ccMat / contacts per	257 ± 1.5	270 ± 1.1	342 ± 1.5
ccMat quadrant 1	64.1 ± 0.4	67.2 ± 0.4	73.4 ± 0.6
ccMat quadrant 2	80.6 ± 0.7	83.8 ± 0.4	19.7 ± 0.6
ccMat quadrant 3	63 ± 1	67.1 ± 0.3	75.3 ± 0.7
ccMat quadrant 4	48.7 ± 0.6	52.3 ± 0.4	171.7 ± 0.7
doMat / $Å^{-2}$	0.69 ± 0.024	0.75 ± 0.009	0.88 ± 0.011
doMat quadrant 1	0.165 ± 0.007	0.185 ± 0.002	0.196 ± 0.003
doMat quadrant 2	0.230 ± 0.007	0.248 ± 0.003	0.085 ± 0.002
doMat quadrant 3	0.172 ± 0.006	0.185 ± 0.002	0.196 ± 0.003
doMat quadrant 4	0.124 ± 0.005	0.135 ± 0.002	0.404 ± 0.004
APL / $Å^2$	60.1 ± 0.11	61.42 ± 0.071	62.04 ± 0.073
PP-dist / Å	40.14 ± 0.058	39.50 ± 0.036	39.20 ± 0.039

Appendix 2.2) Correlation times of interdigitation dynamics. Fluctuations in nISA and ccMat were fit with a double exponential decay

TableA2.2) Correlation times of interdigitation dynamics. Fluctuations in nISA and ccMat were fit with a double exponential decay (Figure A2.3). Shown are the respective correlation times and errors calculated from the fits (using Mathematica's NonlinearLeastSquares[259] function).

bilayer	nISA / ns		ccMat / ns	
	τ_{fast}	τ_{slow}	τ_{fast}	τ_{slow}
MSPC	0.481 ± 0.008	5.93 ± 0.11	0.082 ± 0.003	4.8 ± 0.1
DPPC	0.141 ± 0.007	2.90 ± 0.03	0.036 ± 0.003	3.08 ± 0.065
$DPPC_T$	0.121 ± 0.007	2.55 ± 0.04	0.039 ± 0.003	3.2 ± 0.1

Appendix 2.3) Autocorrelation functions for nISA and ccMat.

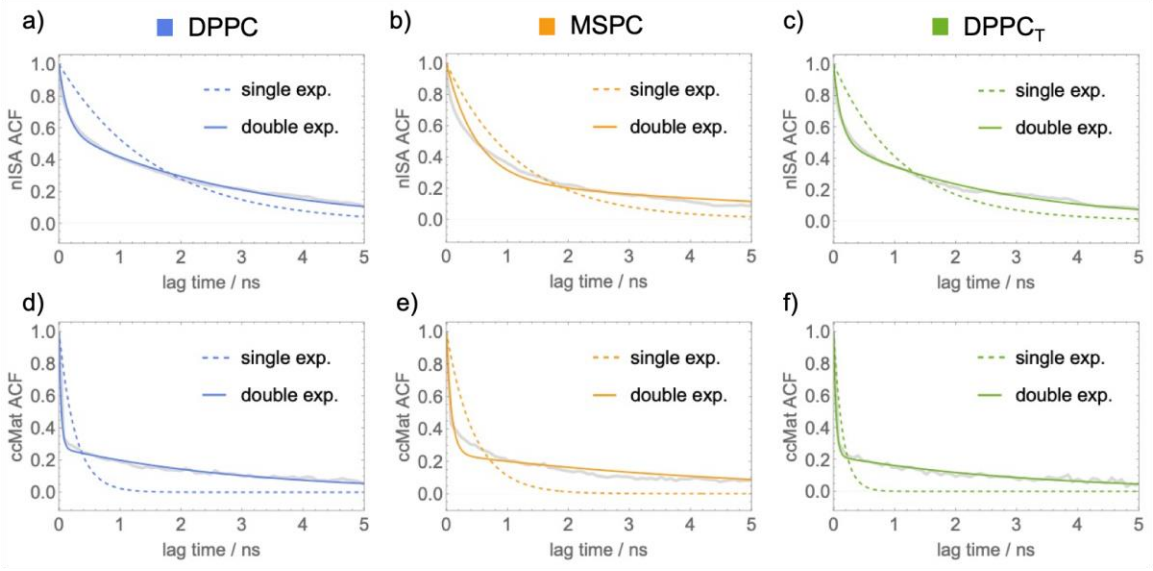


Figure A2.1) Autocorrelation functions of nISA (top) and ccMat (bottom) for each simulated bilayer (gray). Shown on each plot are the corresponding best fits with a single exponential (dashed color line) vs double exponential (solid color line) decay. The resulting correlation times from the double exponential fits are listed in Appendix 2.2.

Appendix 2.4) Additional methods and error analysis

1) *Interdigitation Tool (memIT).* The MEMBPLUGIN[177] package for VMD has a *Lipid Interdigitation* tool that provides three measures of interdigitation: I_p, w_p, and I_C. [177] I_p and w_p are the fraction and width (respectively) of the mass density overlap calculated for a user-specified selection of atoms from the two bilayer leaflets. I_C is the fraction of inter-leaflet atomic contacts calculated from all lipid atoms with a cutoff distance of 4 Å. For comparison with the new methods, we used I_p and performed the analysis on all atoms in the leaflets, including hydrogens.
2) *Error analysis*. For all measured quantities, reported uncertainties are standard errors of the mean calculated by block averaging to properly account for time correlations; an excellent description of this procedure can be found in a recent methods paper from Foley and Deserno[200]. Briefly, consecutive measurements in the time series were iteratively blocked into groups of two and averaged, with the standard error calculated at each blocking iteration. A plot of the standard error vs. blocking iteration shows an initial increase and eventual plateau once the block size is large enough for successive values to be uncorrelated; the uncertainties we report are the standard error at the plateau region. Since the doMat analysis already requires frame averaging, uncertainty was estimated as the standard error of doMat values calculated separately for consecutive blocks of ~1000 frames (a total of 5-10 blocks depending on the trajectory length). For comparing differences in the means of two distributions, p-values were calculated from the Student's *t* distribution with an effective number of degrees of freedom implied by the block averaging procedure.

Appendix 2.5) Interdigitation in simulated bilayers quantified with different methods.

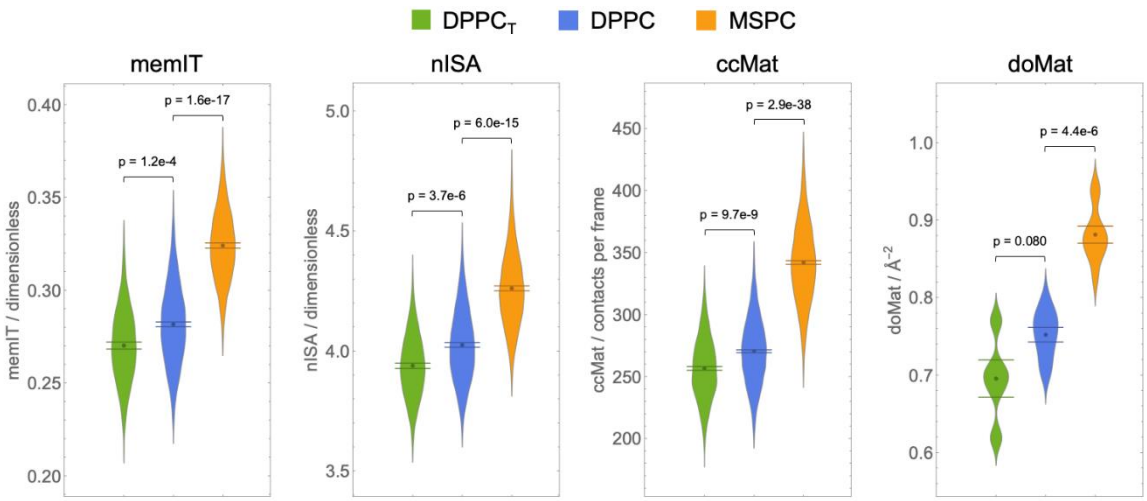


Figure A2.2) Interdigitation in simulated bilayers quantified with different methods. Shown for each method are: the spread in the values from individual frames (for memIT, nISA and ccMat) or consecutive blocks of ~1000 frames (for doMat); their mean and effective standard error of the mean calculated from block averaging as detailed in Supplemental Methods; and the *p*-values for comparisons of the results for DPPC$_T$ and MSPC against those for the DPPC bilayer.

.

Appendix 2.6) Maps of shared Voronoi faces between atoms in opposing leaflets .

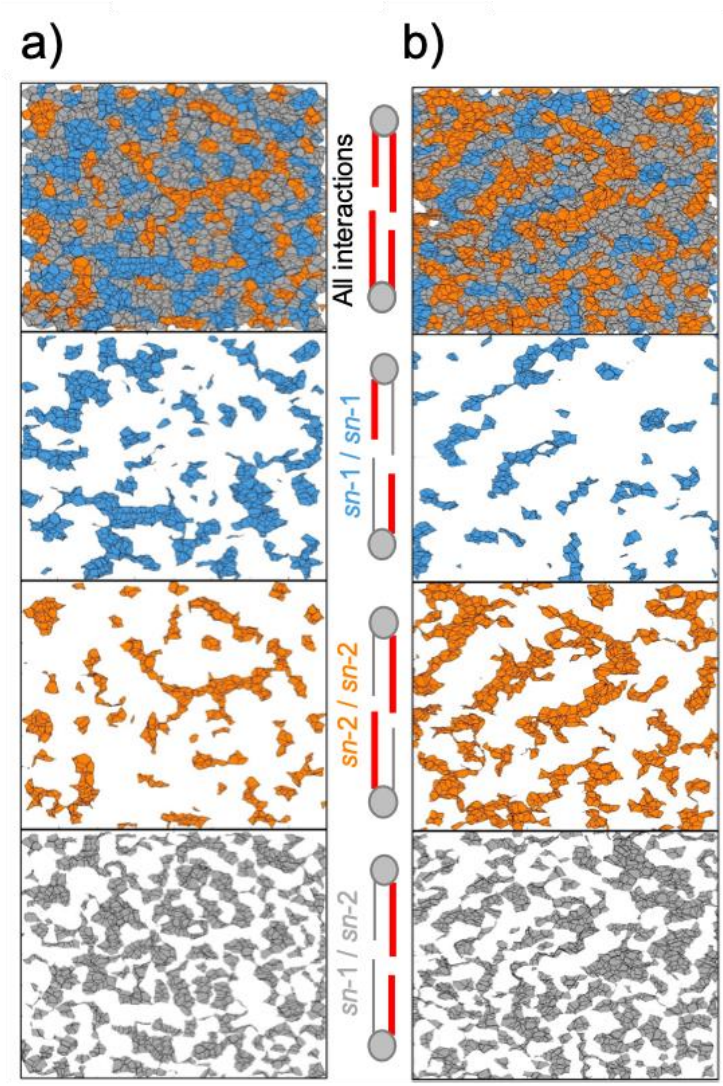


Figure A2.3) Maps of shared Voronoi faces between atoms in opposing leaflets in DPPC (a) and MSPC (b) from the same trajectory frames as in Figure 2.2. Different maps correspond to (from top to bottom): all atom pairs, *sn*-1/*sn*-1 pairs, *sn*-2/*sn*-2 pairs, and *sn*-1/*sn*-2 pairs. Each map is 80 × 80 Å.

Appendix 2.7) Correlation between bilayer thickness (phosphate-to-phosphate distance, PP-dist) and area per lipid (APL)

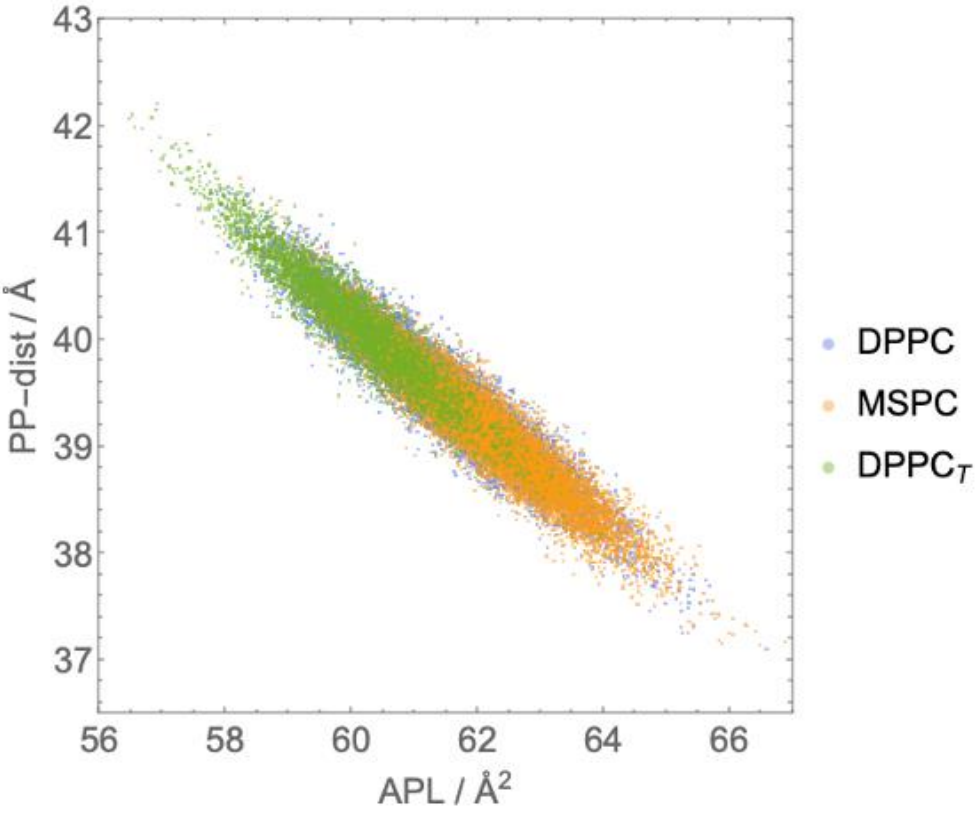


Figure A2.4) Correlation between bilayer thickness (phosphate-to-phosphate distance, PP-dist) and area per lipid (APL) in the three simulated bilayers. Each data point represents a single frame from the corresponding trajectory

Appendix 2.8) Interdigitation in the DPPC$_T$ bilayer quantified with (ccMat) and doMat.

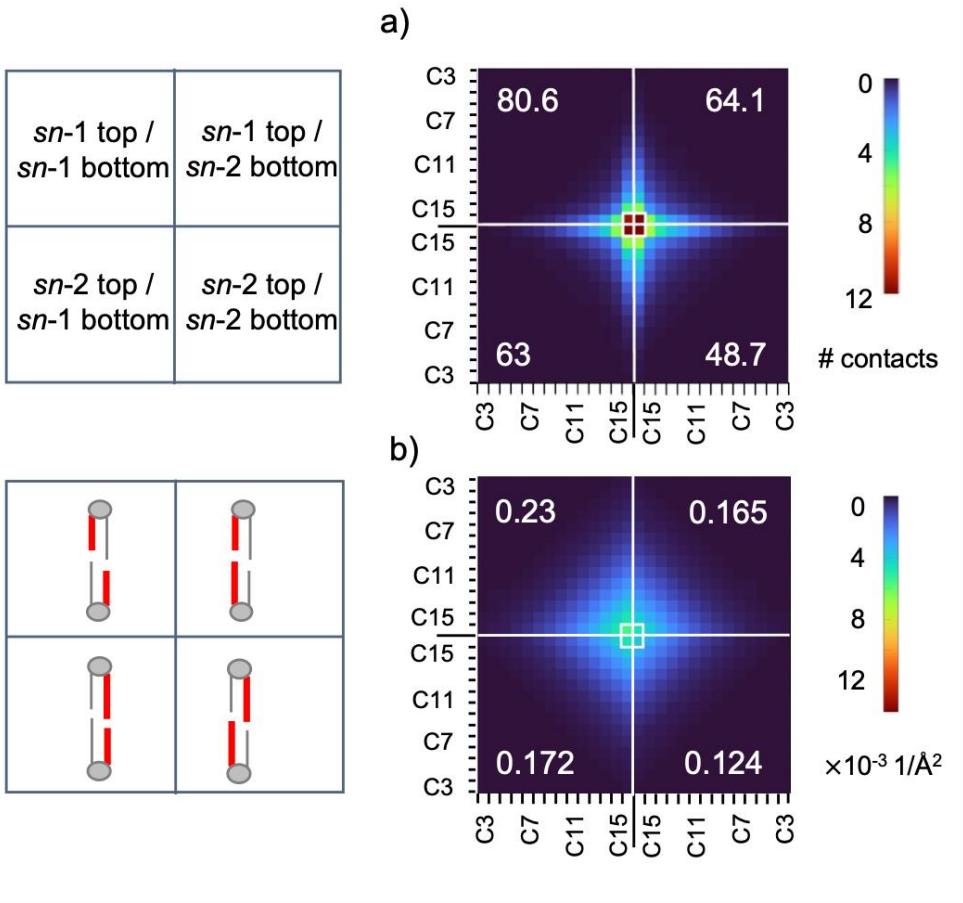


Figure A2.5) Interdigitation in the DPPC$_T$ bilayer quantified with ccMat (A) and doMat (B). Shown are the average results from each method as matrices following the format of Figure 2.3 in the main text. Errors for the quadrant sums are listed in Appendix 2.1.

Appendix 3) Supplemental Figures for Chapter 3

Appendix 3.1) Backbending cutoff distances for acyl chain lengths.

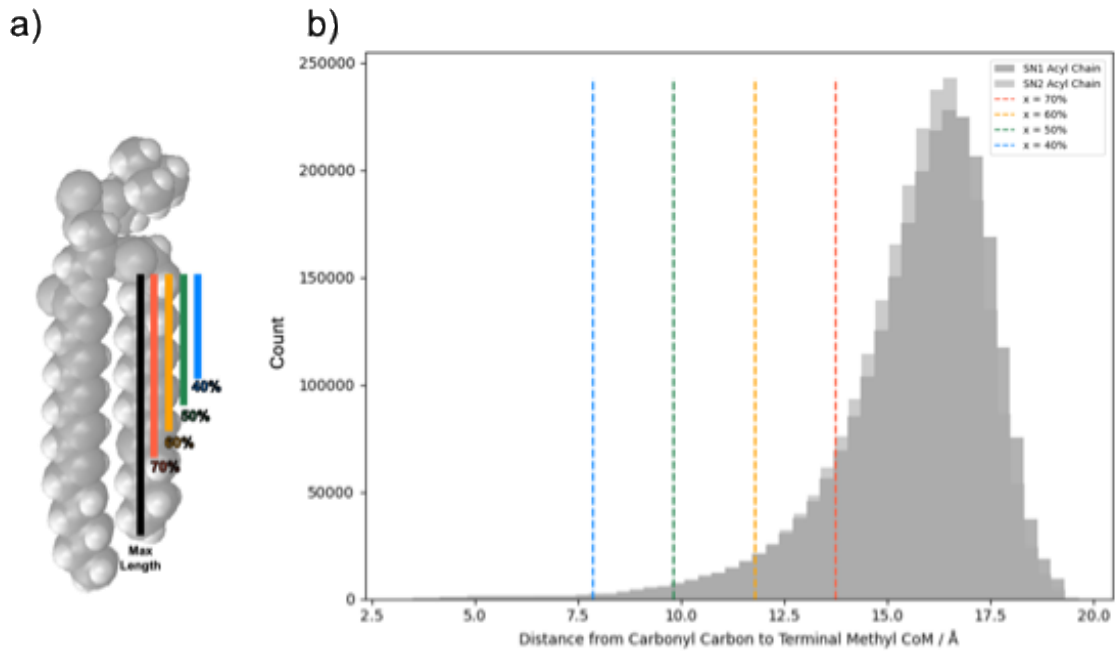


Figure A3.6) Backbending cutoff distances for chain length distances. (a) DPPC is shown with the maximum chain length highlighted in black. The thresholds in this study are defined by a percentage of this maximum distance from the carbonyl carbon and the center of mass of the terminal methyl group. (b) Histogram of *sn*-1 and *sn*-2 chain length distances. The superimposed vertical lines represent the respective thresholds of the study

Appendix 3.2) Acyl chain order parameters for mixed chain lipids.

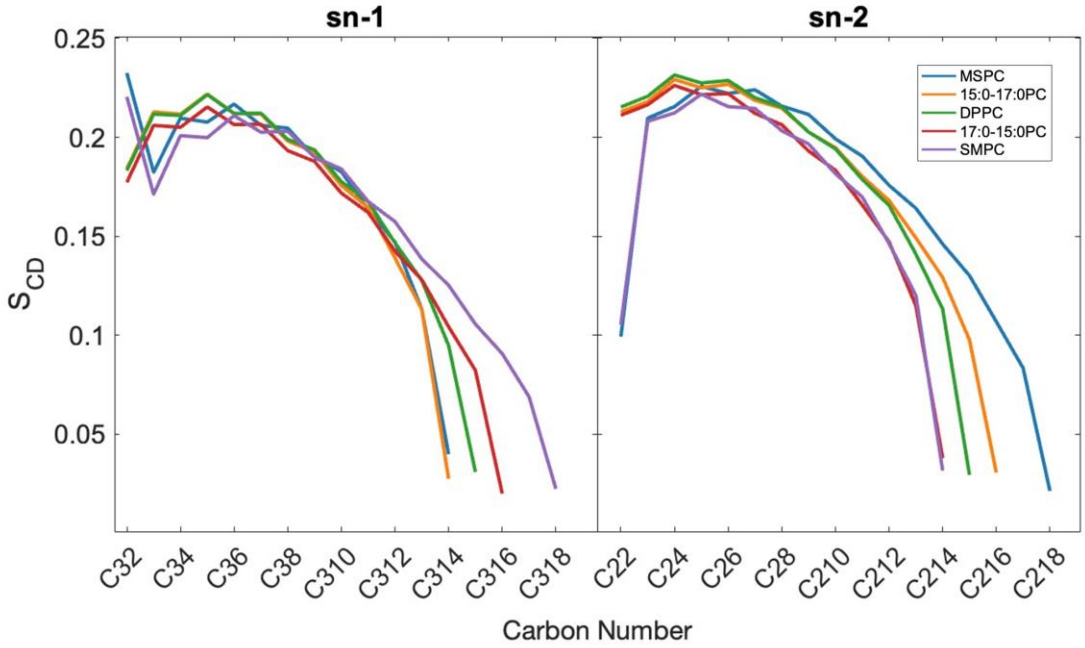


Figure A3.7) Acyl chain order parameters for mixed chain lipids. The deuterium order parameters were calculated for each lipid. The average order parameter for each carbon is shown with the *sn*-1 and *sn*-2 plotted separately. The legend applies for both panels. Overall, the *sn*-2 chains are more disordered.

Appendix 3.3) Bending rigidity and APC from this study and Doktorova et al..[108]

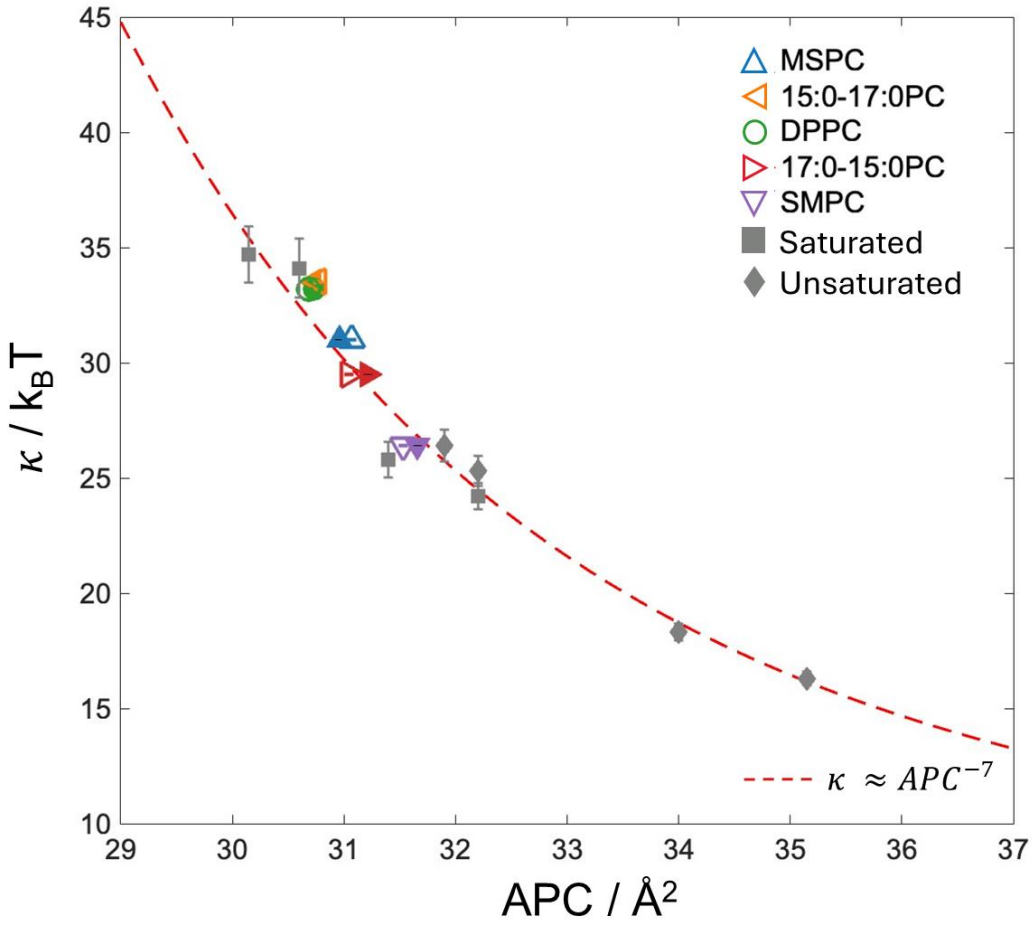


Figure A3.8) Bending rigidity and APC from this study and Doktorova et al..[108] The relationship of APC and κ is well known. These mixed chain lipids follow the trend. Shown in gray are lipids from a previous method application in ref[108] both saturated and unsaturated systems. SMPC behaves similarly to some unsaturated species, while the rest of the mixed chain lipids behavior mimics other saturated lipid systems.

Appendix 3.4) Interdigitation values for mixed-chain lipids

Table A3.3) Interdigitation values for mixed-chain lipids

Lipid	doMat / $Å^{-2}$	nISA / dimensionless	memIT / dimensionless	ccMat / contacts per frame
MSPC	0.88 ± 0.026	4.26 ± 0.010	0.324 ± 0.0019	340± 1.5
15:0-17:0 PC	0.79 ± 0.020	4.04 ± 0.012	0.27 ± 0.0018	270±1.2
DPPC	0.75 ± 0.035	4.02 ± 0.011	0.26 ± 0.022	270± 1.1
17:0-15:0 PC	0.94 ± 0.028	4.31 ± 0.009	0.29 ± 0.012	300±1.5
SMPC	1.18 ± 0.016	4.76 ± 0.011	0.330 ± 0.012	340 ± 1.3

Appendix 3.5) Second-order polynomial fits for interdigitation and backbending as a function of acyl chain length mismatch

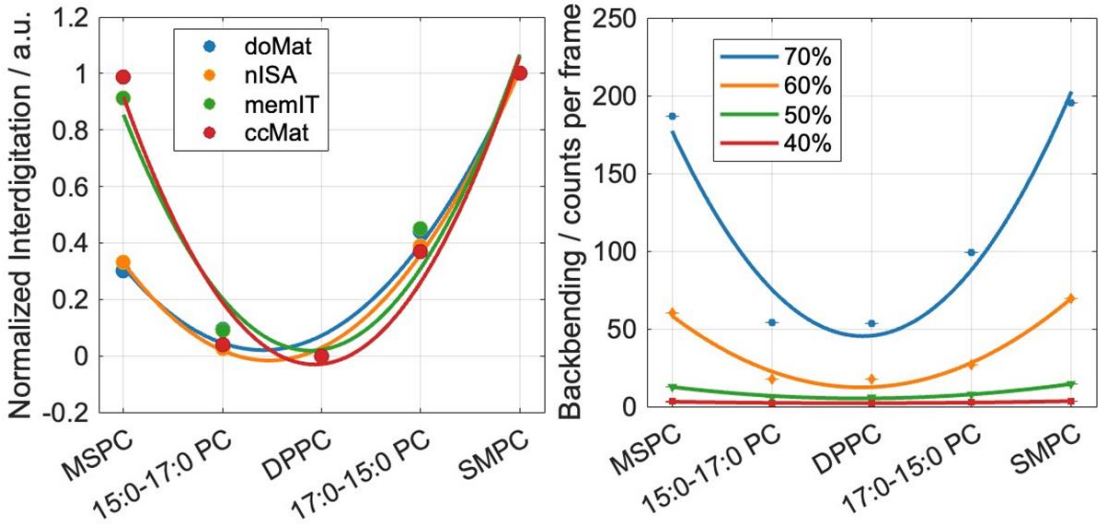


Figure A3.9) Second-order polynomial fits for interdigitation and backbending as a function of acyl chain length mismatch. (Left): Interdigitation shows a quadratic correlation with the difference in carbon numbers between the two acyl tails in mixed-chain lipids. Each interdigitation method was fit with a second-order polynomial; corresponding R^2 values are provided in Appendix Figure 3.5. (Right): Counts per frame of backbending acyl chains also exhibit a second-degree polynomial relationship with the difference in carbon number between the *sn*-1 and *sn*-2 chains. Each maximum chain length threshold was independently fit, with R^2 values reported in Appendix 3.6

Appendix 3.6) R^2 of second degree polynomial fits for interdigitation values·

Table A3.4) R^2 of second degree polynomial fits for interdigitation values·

Interdigitation Analysis Method	R^2 of second order polynomial fit
doMat	0.984
nISA	0.997
memIT	0.951
ccMat	0.955

Appendix 3.7) R^2 values for normalized backbending versus normalized interdigitation

Table A3.5) R^2 values for normalized backbending versus normalized interdigitation

	Backbending Chain Length Threshold			
Interdigitation Method	70%	60%	50%	40%
doMat	0.594	0.66	0.985	0.997
nISA	0.627	0.701	0.943	0.963
memIT	0.644	0.716	0.950	0.965
ccMat	0.735	0.798	0.946	0.943

Appendix 3.8) R^2 of second degree polynomial fits for backbending counts.

Table A3.6) R^2 of second degree polynomial fits for backbending counts.

Max Chain Length Threshold	R^2 of second order polynomial fit
70%	0.959
60%	0.978
50%	0.983
40%	0.993

Appendix 4)

Appendix 4.1) Probe excitation and emission spectra and collection channels. Spectra of Naph and DiD probes.

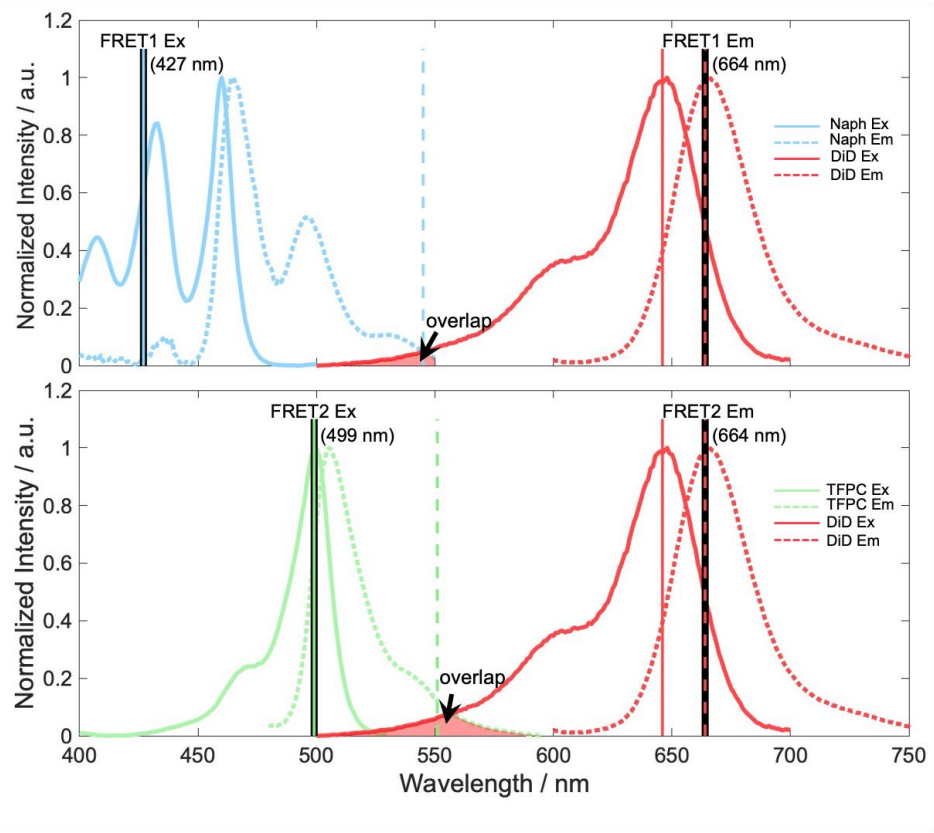


Figure A4.1) Probe excitation and emission spectra and collection channels. Spectra of Naph and DiD probes. Dashed vertical lines indicate the emission wavelength collection channels for Naph (545 nm) and DiD (664 nm), while solid vertical lines mark the excitation wavelengths (Naph: 427 nm; DiD: 646 nm). (bottom) Spectra of TFPC and DiD probes. Dashed vertical lines represent the emission collection channels for TFPC (551 nm) and DiD (664 nm), and solid vertical lines indicate the excitation wavelengths (TFPC: 499 nm; DiD: 646 nm). In both panels, the red shaded regions highlight the spectral overlap between the donor emission and acceptor excitation—an essential condition for FRET. However, excessive overlap can lead to spectral cross-talk. The collection channels for FRET excitation and emission are shown with solid black lines.

Appendix 4.2) FRET1 and FRET2 data for single-component DOPC.

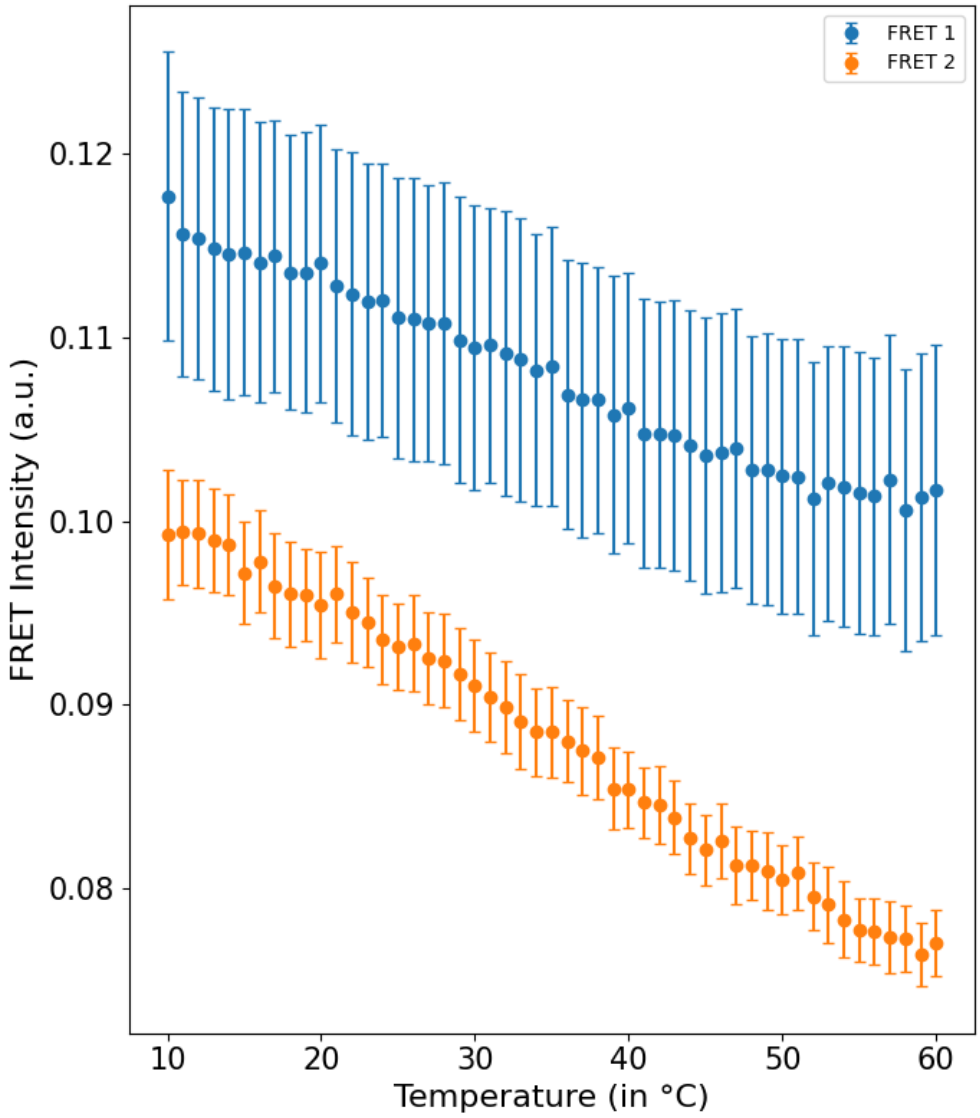


Figure A4.2) FRET1 and FRET2 data for single-component DOPC. The plot shows weighted FRET intensity values for 10 sample replicates for 100% DOPC system. The error bars on the plots are found by the standard error of the mean. The gradual increase in intensity is because of quantum yield and not the phase behavior.

Appendix 4.3) χ^2_{red} for all sample replicates for 100% DOPC, DPPC/POPC/Chol (40/40/20mol%), and DPPC/DOPC/Chol (40/40/20mol%).

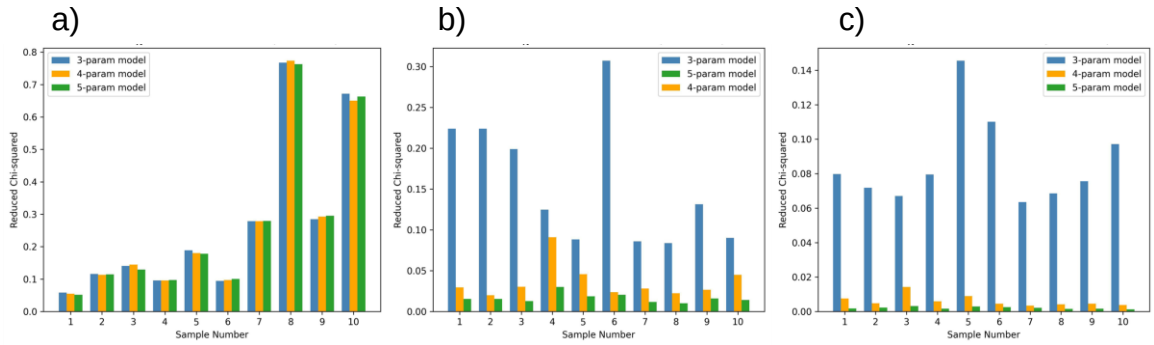


Figure A4.3) χ^2_{red} for all sample replicates for 100% DOPC, DPPC/POPC/Chol (40/40/20mol%), and DPPC/DOPC/Chol (40/40/20mol%). (a) shows that for uniform samples show no significant different in the between models. In the phase-separated systems, (b) (DPPC/POPC/Chol) and (c) (DPPC/DOPC/Chol) there is a distinct difference in the χ^2_{red}. The differences in (b) are smaller than in (c) suggesting the nanoscopic mixture has increase fitting noise compared to macroscopic heterogeneity.

Appendix 4.4) Ratios of χ^2_{red} for all sample replicates for 100% DOPC, DPPC/POPC/Chol (40/40/20mol%), and DPPC/DOPC/Chol (40/40/20mol%).

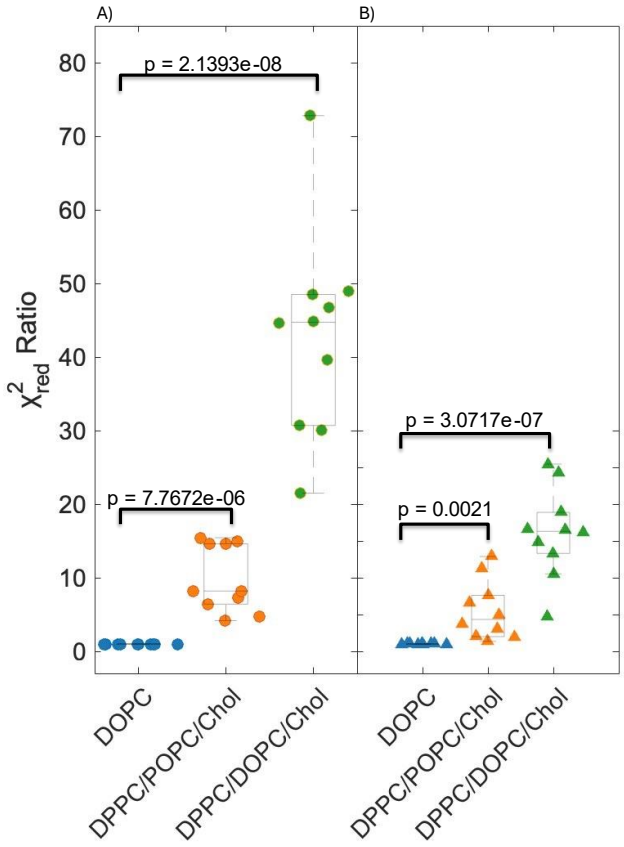


Figure A4.4) Ratios of χ^2_{red} for all sample replicates for 100% DOPC, DPPC/POPC/Chol (40/40/20mol%), and DPPC/DOPC/Chol (40/40/20mol%). Both ratios show that for uniform samples the ratio of is ~1. In the phase-separated systems, (DPPC/POPC/Chol) and (DPPC/DOPC/Chol) there is a distinct increase in the ratios when compared to uniform DOPC. In the phase-separated systems (DPPC/POPC/Chol) and (DPPC/DOPC/Chol), there is a distinct increase in the χ^2 ratios compared to the DOPC control. The p-values and χ^2_{red} ratios indicate that both ternary mixtures exhibit phase separation. Furthermore, the 5-parameter model (A) provides a statistically improved fit over the 4-parameter model (B), supporting its utility in capturing nanoscopic heterogeneity.

Appendix 4.5) $F_{Ratio}(T)$ for the 1:1 line of DPPC/DOPC/Chol with increasing cholesterol concentration.

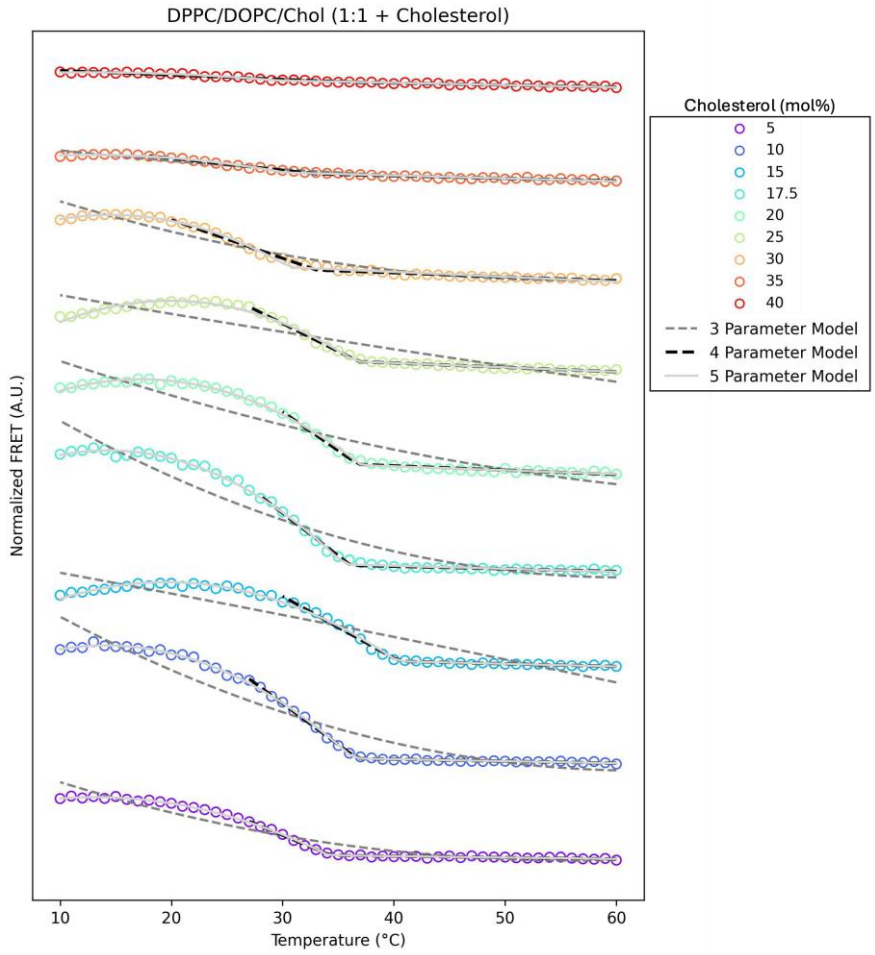


Figure A4.5) $F_{Ratio}(T)$ for the 1:1 line of DPPC/DOPC/Chol with increasing cholesterol concentration. Each line is an independent FRET experiment with a distinct amount of cholesterol. All experiments were fit with the 3(dark gray dashed),4 (black dashed), and 5 (light gray solid) parameter models.

Appendix 4.6) T_{misc} determined by FRET Curves

Table A4.1) T_{misc} determined by FRET Curves

	FRET 1 T_{misc} (°C)		FRET 2 T_{misc} (°C)		FRET Ratio T_{misc} (°C)	
Parameter Model	4	5	4	5	4	5
DPPC/POPC/Chol (40/40/20mol%)	38 ± 4	36 ± 7	35 ± 2	34 ± 2	35 ± 1	34 ± 2
DPPC/DOPC/Chol (40/40/20mol%)	37.7 ± 0.69	37.5 ± 0.95	39 ± 2	36.1 ± 0.95	35.5 ± 0.48	36.0 ± 0.68

Appendix 5)

Appendix 5.1) GUV T_{misc} experiment for SMPC/DOPC/Chol. Images of GUVs for a three-component system SMPC/DOPC/Chol (40/40/20mol%) starting from 17℃ to 23℃.

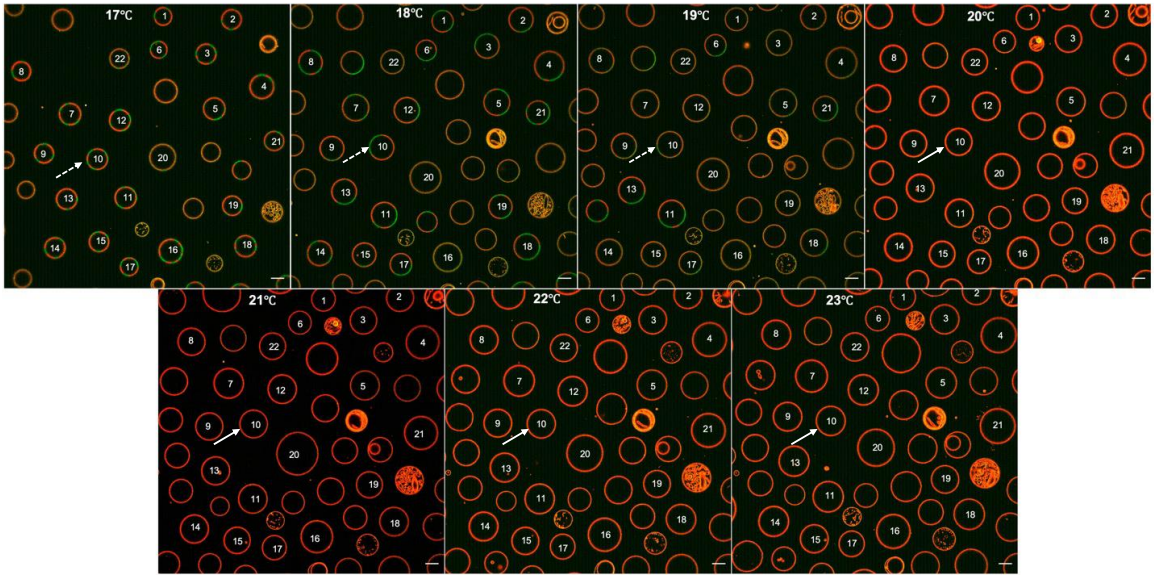


Figure A5.1) Figure A5.1) GUV T_{misc} experiment for SMPC/DOPC/Chol. Images of GUVs for a three-component system SMPC/DOPC/Chol (40/40/20mol%) starting from 17°C to 23°C. GUVs were labelled with fluorescent dyes LRPE (red) and 18:0 NBD (green). GUVs were prepared by electro-formation method and imaged on VA Heat substrate. Arrows indicate a representative vesicle, with dashed arrows marking its phase-separated state and a solid arrow indicating the transition to a uniform state. Each image presented is the fluorescence collected from both green and red channel using Image J. The data is then fitted in a sigmoidal fit shown in [Eq 1] to precisely calculate T_{misc}. Scale bars are 10μm

Appendix 5.2) Full field-of-view cryo-EM images of ternary liposomes. The first row is an overlay with thicknesses determined from the I(w) profiles.

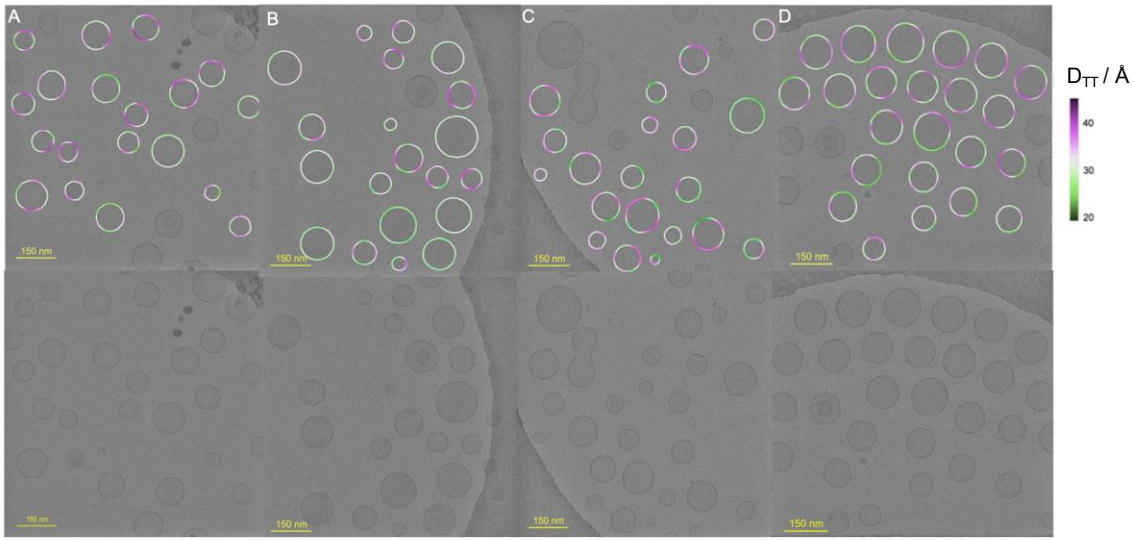


Figure A5.2) Full field-of-view cryo-EM images of ternary liposomes. The first row is an overlay with thicknesses determined from the I(w) profiles. The bottom row is the full field of view with no overlay. Column (A) is DPPC/DOPC/Chol (40/40/20), (B) MSPC/DOPC/Chol (40/40/20), (C) is 15:0-PC/DOPC/Chol (40/40/20), (D) is SMPC/DOPC/Chol.

Appendix 5.3) Representative FRET data for 40/40/20 mol% DOPC/DPPC/Cholesterol.

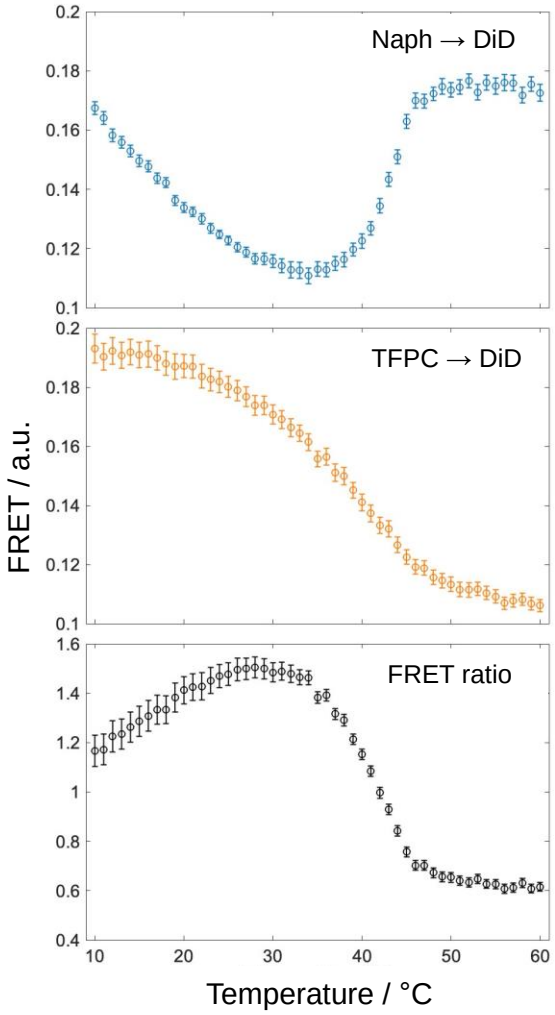


Figure A5.3) Representative FRET data for 40/40/20 mol% DOPC/DPPC/Cholesterol. The top panel shows FRET intensity for Pair 1 (Nap to DiD), which decreases with decreasing temperature due to the probes preferring different phases. The middle panel displays FRET intensity for Pair 2 (TF-PC to DiD), which increases with decreasing temperature as both probes partition into the same phase. The bottom panel presents the FRET ratio (Pair 1/Pair 2), which enables accurate determination of T_{misc}

Appendix 5.4) Model fits and χ^2_{red} ratios for FRET samples. Panel a shows FRET ratio data for DOPC and ternary mixtures with uniform and phase-separated model fits.

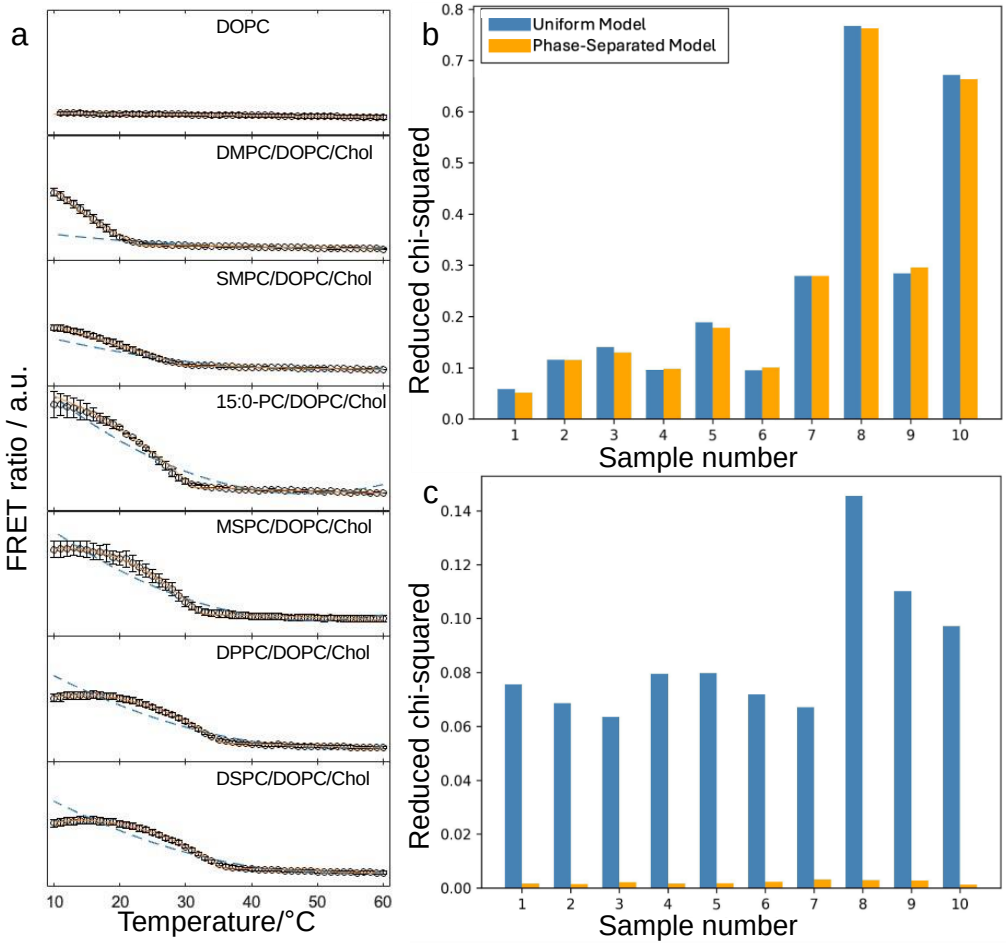


Figure A5.4) Model fits and χ^2_{red} ratios for FRET samples. Panel a shows FRET ratio data for DOPC and ternary mixtures with uniform and phase-separated model fits. Average FRET ratio for DOPC, and 40/40/20 mol% ternary mixtures fit with uniform model fits (dashed lines) and phase-separated model fits (solid lines). Each plot is a minimum of 3 replicates. In each of the ternary mixtures, the best fits came from the phase-separated models. The best fitting models are shown in (a). (b) and (c) shows the reduced chi-squared (χ^2_{red}) for 10 sample replicates of uniform (DOPC) and phase-separated (40/40/20 mol % DPPC/DOPC/Chol) model fits respectively. The DOPC replicates have no significant difference in the value between the phase-separated and uniform model. However, in (c) the phase-separated model fits significantly better than the uniform model for all 10 replicates.

Appendix 5.4) Sigmoidal model fitting

A5.4.1. Sigmoidal model for determining the miscibility transition temperature of GUVs

In addition to characterizing macroscopic phase behavior at 22 °C), we utilized precise temperature control by balancing the cooling collar with the temperature sensing VA Heat to report the miscibility transition temperature from GUVs. For mixtures that exhibited phase separation at 22°C, such as DPPC/DOPC/Chol, MSPC/DOPC/Chol, DSPC/DOPC/Chol, and 15:0-PC/DOPC/Chol, we initiated the temperature ramping at 22°C and increased the temperature in 1 °C increments with 30 seconds equilibration time until the vesicles appeared uniform. We suspected that T_{misc} was below 22°C for samples that appeared uniform in our initial studies; therefore, we began measurements at 17 °C, increasing the temperature similarly in 1 °C increments with 30 seconds equilibration time until all vesicles were uniform. Temperatures below 17 °C were avoided to prevent condensation on the objective lens, which introduces imaging artifacts.

For each composition, we selected a field of view containing a minimum of 9 clearly phase-separated vesicles. These same vesicles were monitored across the temperature range, with images collected at each temperature point. During image processing in ImageJ, vesicles were individually numbered, allowing us to track the fraction of phase-separated vesicles at each temperature. An example for one of our systems is shown in Figure S6. The resulting data were fit using a sigmoidal function based on the general form of the error function,

$$f(T; T_{misc}, \sigma) = \frac{1}{2}\left\{Erf\left(\frac{T + T_{misc}}{\sqrt{2}\sigma}\right) - Erf\left(\frac{T - T_{misc}}{\sqrt{2}\sigma}\right)\right\}, \qquad (S1)$$

where Erf is the general error function, T is the temperature, and T_{misc} and σ are parameters describing the center and width of the transition, respectively. σ and T_{misc}

was treated as a free parameter to obtain best fit to the data. Error bars for T_{misc} were calculated as the pooled standard error of the mean obtained from three sample replicates.

VITA

Emily H. Chaisson was born in North Carolina, and raised in Stokesdale with her sister and parents. She split her childhood between the classroom and the softball field.

She played softball at the University of Mount Olive and graduated Cum Laude with degrees in math and chemistry – though the chemistry part was mostly to stay on the team all four years. Her undergraduate adviser, Dr. Jason Pajski, introduced her to computational biophysics. During her REU at the University of Alabama at Birmingham, she saw how some research combines computational techniques with experimental work, and she knew that was the skillset she wanted to develop.

Emily started at the University of Tennessee in fall of 2020 and joined the Heberle lab in the spring of 2021 where she used simulations to study lipid bilayers. Wanting to join in with her lab mates – and stop putting them to sleep with code - she began experiments in the spring of 2023.

Emily plans to continue doing science that involves coding, lots of talking, cool ideas, and is ideally near a beach.